Dipl.-Ing. Stefan Topolovec

In-situ studies of the correlations between electrochemical processes and magnetic properties

DOCTORAL THESIS

For obtaining the academic degree of

Doktor der technischen Wissenschaften

Doctoral Programme of Technical Sciences
Technical Physics

Graz University of Technology

Supervisor:

Univ.-Prof. Dipl.-Phys. Dr.rer.nat. Roland Würschum

Institute of Materials Physics

Graz, October 2015

Abstract

The combination of magnetism and electrochemistry has attracted considerable attention in the last years for various application-relevant issues. One aspect of this combination pertains to the electrodeposition of magnetic thin films. On the other hand, a promising research field has recently opened up with in-situ studying the influence of electrochemical charging processes on the magnetic properties of high-surface area porous nanomaterials and thin films, with the aim to achieve voltage control of the magnetic properties. Furthermore, the electronic and chemical processes which occur in an electrode during charging/discharging can be characterized by using magnetism variations as diagnostic tool.

For each of theses topics, the control of magnetic properties by electrochemical processes demands appropriate in-situ measurement techniques. By designing a three-electrode electrochemical cell for operation in a commercial state-of-the-art SQUID magnetometer, which allows the simultaneous measurement of magnetization and cyclic voltammograms, we have developed a new approach for studying the correlations between electrochemical processes and magnetic properties. This is demonstrated in the present thesis for the three topics mentioned above.

In the case of electrodeposition, the emergence and decreasing of magnetism during the growth and dissolution of thin Co films on a Au(111) substrate is studied by the novel electrochemical cell, facilitating in-situ electrodeposition in a SQUID magnetometer. This measurement approach enables not only a determination of the absolute magnetic moment m_{film}, which arises exclusively from the electrodeposited Co film, but also an adjustment and determination of the film thickness. Hence, the thickness-dependence of m_{film} could be studied. For ultrathin films an enhancement of the magnetic moment per Co atom could be observed, which increases steadily with lowering the film thickness, and reaches up to 40 % for a film thickness of one atomic layer.

Regarding the case of electrochemical tuning of magnetic properties, the ability of the novel

electrochemical cell design to monitor the magnetic moment m during cyclic voltammetry measurements was utilized to distinguish which electrochemical process at the electrode-electrolyte interface causes the m-variation. The reversible variation of the magnetic moment of porous nanophase Pt during electrooxidation of up to 1 % was attributed to the high electric field which is generated by electrochemical double layer charging. For γ-Fe_2O_3 nanoparticles the variation of the magnetic moment of up to 4.9 % strongly depend on the potential regime of charging and is related to a pseudocapacitive redox reaction.

In the last case, the novel cell design enabled the first in-operando measurements of the magnetic susceptibility of commercially used Li-ion battery cathode material. This was demonstrated by monitoring the magnetic susceptibility χ_{LCO} of Li_xCoO_2 cathodes during consecutive cycles of charging and discharging. The distinct variation of χ_{LCO} with Li content x gave insights into the chemical and electronic processes occurring in the cathode during charging and discharging. In particular, the measurementes revealed that an occurring nonmetal-metal transition is of Anderson type and that in addition to cobalt also oxygen undergoes partial oxidation during charging.

Kurzfassung

Die Kombination von Magnetismus und Elektrochemie erhielt in den letzten Jahren hohe Aufmerksamkeit aufgrund mehrerer anwendungsrelevanter Themen. Ein Aspekt dieser Kombination betrifft die elektrochemische Abscheidung von magnetischen dünnen Filmen. Zum anderen eröffnete sich kürzlich durch in-situ Untersuchungen des Einflusses von elektrochemischen Beladeprozessen auf die magnetischen Eigenschaften von porösen Nanomaterialien und dünnen Filmen mit großer Oberfläche ein vielversprechendes Forschungsfeld mit dem Ziel, die magnetischen Eigenschaften über die angelegte Spannung zu steuern. Außerdem können die elektronischen und chemischen Prozesse, welche in einer Elektrode während einer Be- und Entladung stattfinden, durch die auftretenden Magnetismusänderungen charakterisiert werden.

Für jede der genannten Fragestellungen ist es erforderlich, dass der Einfluss der elektrochemischen Prozesse auf die magnetischen Eigenschaften durch eine geeignete in-situ Messmethode untersucht werden kann. Durch die Entwicklung einer neuen elektrochemischen Zelle in 3-Elektrodengeometrie, welche die Messung von Zyklovoltammogrammen in einem SQUID Magnetometer und somit die gleichzeitige elektrochemische und magnetische Charakterisierung erlaubt, wurden solche in-situ Messungen in einer neuen Qualität ermöglicht. Die Möglichkeiten dieser neuen Messmethode werden in dieser Arbeit anhand der obigen drei Themen verdeutlicht.

Zum einen wird die neue elektrochemische Zelle zur in-situ Abscheidung von dünnen Co Filmen auf einem Au(111) Substrat im SQUID Magnetometer verwendet. Die gleichzeitige Messung des magnetischen Momentes erlaubt es, die Entwicklung des Magnetismus während des Schichtwachstums mitzuverfolgen. Darüber hinaus ermöglicht diese neue Messmethode nicht nur die Bestimmung des absoluten magnetischen Momentes m_{film}, welches alleinig vom abgeschiedenen Co Film stammt, sondern auch die Einstellung und Bestimmung der Filmdicke. Auf diese Weise konnte die Dickenabhängigkeit von m_{film} untersucht

werden. Für ultradünne Filme wurde eine Erhöhung des magnetischen Momentes pro Co Atom beobachtet, welche mit abnehmender Filmdicke kontinuierlich zunimmt, und für eine Filmdicke von einer Atomlage Werte von bis zu 40 % erreicht.

In-situ Zyklovoltammetriemessungen wurden darüberhinaus zur Untersuchung der elektrochemischen Durchstimmbarkeit der magnetischen Eigenschaften von porösen Nanomaterialien eingesetzt. Anhand dieser Messungen lässt sich herausfinden, durch welche elektrochemischen Prozesse an der Elektroden-Elektrolyt Grenzfläche die jeweiligen Änderungen des magnetischen Momentes hervorgerufen werden. Die reversible Änderung des magnetischen Momentes von bis zu 1 %, die an porösen, nanophasigen Pt während der Elektrooxidation beobachtet wurde, konnte dem hohen elektrischen Feld, welches durch das Beladen der elektrochemischen Doppelschicht entsteht, zugeschreiben werden. Für γ-Fe_2O_3 Nanopartikel hängt die Änderung des magnetischen Momentes von bis zu 4.9 % stark vom Potentialbereich der Beladung ab und kann einer pseudokapazitiven Redoxreaktion zugeschrieben werden.

Schließlich wurde das neue Zellendesign für die ersten magnetischen in-operando Messungen von kommerziell verwendeten Batteriekathodenmaterialien herangezogen. Auf diese Weise war es möglich die magnetische Suszeptibilität χ_{LCO} von Li_xCoO_2 Kathoden während drei aufeinanderfolgenden Lade- und Entladezyklen kontinuierlich zu messen. Anhand der markanten Änderung von χ_{LCO} mit der Lithiumkonzentration x konnten Rückschlüsse auf die chemischen und elektronischen Prozesse gezogen werden, die in der Kathode während des Ladens und Entladens ablaufen. Dabei stellte sich heraus, dass ein auftretender Nichtmetall-Metall Übergang vom Anderson-Typ ist und, dass während des Ladens zusätzlich zu Co auch Sauerstoff teilweise oxidiert wird.

Contents

CHAPTER 1

Introduction

"At first sight, magnetism and electrochemistry seem an odd couple." This sentence is quoted from an article by Coey [1], where he explains this putative incompatibility by the fact that the energies involved in chemical reactions and the magnetic energies (e.g. the Zeeman splitting energy) differ by orders of magnitude. Nonetheless, the combination of magnetism and electrochemistry has attracted considerable attention in the last years, since there is a connection between these two disciplines in at least three different fields:

(i) Magnetoelectrochemistry deals with electrochemistry in the presence of an imposed magnetic field and studies the influence of the field on the mass transport kinetics, the electrode kinetics and the morphology of electrodeposits [1, 2].

(ii) Electrodeposition of ferromagnetic metals and alloys is a further interdisciplinary field where electrochemistry meets magnetism [1]. Electrodeposition has developed as a preparation technique not only for magnetic thin films of metals [3–5], soft and hard magnetic alloys, like e.g. permalloy [6,7] and FePt [8,9], but also of magnetic multilayer structures [10–12] and magnetic nanowires, which can be obtained by template assisted electrodeposition [13, 14].

(iii) Electrochemically charging-induced variations of magnetism represents the third research area covering both magnetism and electrochemistry. On the one hand, the aim of this field is to achieve voltage control of magnetic properties of high-surface area nanomaterials (see e.g. [15–18]) and magnetic thin films (see e.g. [19–23]). On the other hand, the electrochemically induced alterations of magnetic properties can be used as a diagnostic tool, to characterize electronic and chemical processes occurring

in the investigated material during electrochemical charging/discharging.

For the last two cases the correlations between the occurring electrochemical processes and the magnetic properties are of pivotal relevance. Therefore, techniques that allow to measure the magnetic properties during electrochemical experiments are necessary. In particular, a technique enabling a continuous monitoring of the magnetic properties during electrochemical characterization measurements, i.e., cyclic voltammetry measurements, would represent an ideal candidate for studying these correlations.

In this thesis, such a technique was developed by designing a three-electrode electrochemical cell, which allows for in-situ cyclic voltammetry measurements in a commercial SQUID magnetometer. The new cell design is based on the cell established by T. Traußnig in his PhD thesis [18,24], with the major improvements of a reduced magnetic background signal and of a third electrode, enabling the in-situ cyclic voltammetry measurements. By this means, a precise correlation between the detected variations of the magnetic moment and the electrochemical processes occurring at the investigated sample becomes possible. The advantages of this novel cell design are illustrated by applying it to the two later cases mentioned above – electrodeposition and electrochemically charging-induced variations of magnetism.

In the case of electrodeposition the combination of SQUID magnetometry and in-situ electrodeposition of cobalt is used for studying the evolution of magnetism in ultrathin Co films. So far, in-situ magnetic characterization during electrodeposition has been developed and applied for magneto-optical Kerr effect (MOKE) [4, 5, 22, 25–33], alternating gradient field magnetometry (AGFM) [5, 29, 34–38] and ferromagnetic resonance (FMR) [39] measurements. Whereas these techniques yield information about spin orientation, coercivity or ratio between the remanent and saturation magnetization, neither of these techniques allows to determine absolute magnetic moments. The novel in-situ electrochemical cell presented in this thesis enables such measurements of the absolute magnetic moment with a SQUID magnetometer. This is demonstrated by means of thin Co films which are electrodeposited on a Au/Si substrate by cyclic voltammetry. With the new in-situ technique, a precise cancellation of the parasitic background signal of the cell and substrate becomes possible. This gives direct experimental access to the magnetic moment which arises exclusively from the electrodeposited Co film. By adjusting the Co film thickness via the electrodeposition parameters, the magnetic moment can be determined in absolute terms as a function of the film thickness. This in situ-electrodeposition of thin Co films is covered in Chapter 4 of this

thesis.

As mentioned above, there are two different aims in the field of electrochemically charging-induced variations of magnetism. Both of them are addressed in this thesis: Chapter 5 deals with the electrochemical tuning of magnetic properties of porous nanophase systems. As proposed by Gleiter et al. [40], the high electric fields which can be achieved in the electrochemical double layer at an electrode-electrolyte interface can be used to reversibly tune the magnetic properties of nanomaterials exhibiting a high-surface-to volume ratio. This was, for example, demonstrated for porous nanophase Pd-Ni [15], Pd [17] and Pd-Co [16], as well as for thin films of FePt [19], FePd [19] and Pd-Co [41]. More recently it was shown that besides tuning via an electric field, the magnetic properties of such systems can also be varied by chemical reactions induced by electrochemical charging (see e.g. [18, 20, 21]). To distinguish between these two effects, a precise electrochemical characterization is necessary. Ideally, this characterization occurs simultaneously with the magnetic measurements by an in-situ technique. In this thesis, this is achieved by means of the novel electrochemical cell design, that allows for in-situ cyclic voltammetry measurements in a SQUID. This new cell is applied to study the tunability of the magnetic moment m of γ-Fe_2O_3 nanoparticles, for which reversible variations of m of up to several percent were reported by our group in a previous work [18]. In this thesis, the ability of the novel cell to monitor m continuously during cyclic voltammetry measurements is used to derive more detailed information on the correlations between the electrochemical processes and the magnetic behavior. In addition, the alterations of the magnetic moment of porous nanophase Pt upon electrochemical oxidation are investigated and compared with variations of the electrical resistance. This direct comparison of these two different electronic properties in combination with the in-situ cyclic voltammetry measurements allows to distinguish between the influence of the various electrochemical processes (electrochemical double layer charging and chemical modification) and, therefore, provides a deeper understanding of the underlying charging-related processes.

The aim to use the alterations of the magnetic properties induced by electrochemical charging as diagnostic tool is pursued in Chapter 6 for in-situ studying battery charging. Since the magnetic properties of the technologically important Li-ion battery electrode materials are sensitive to phase composition, structural disorder, defects and the oxidation state of the transition metal ion (see [42] for a review), this material class is an ideal candidate for such kind of studies. Unti now, however, all magnetic measurements on commercially

used battery electrodes were performed ex-situ. By means of the novel cell design with reduced background signal, the first in-operando studies become possible, facilitating reliable electrochemical charging/discharging of the battery and enabling the detection of the paramagnetic signal of commercially used cathode materials. This is demonstrated by in-operando SQUID magnetometry measurements on Li_xCoO_2 cathodes during Li extraction and re-intercalation, providing new insights into the electronic and chemical processes in the cathode material during charging and discharging.

Before dealing with these three issues in the Chapters 4-6, the fundamentals of the electrochemical processes occurring at an electrode-electrolyte interface are briefly summarized in chapter 2. In Chapter 3, the basics of the experimental methods and set-ups applied in the present work are described. In Chapters 4-6, the results of the three different topics are presented and discussed. At the beginning of each of the three chapters, an overview of the state-of-the art of research in the particular field is given. Finally, a conclusion is drawn in Chapter 7.

List of publications arising from this thesis

During the completion of this thesis, some aspects of this study have been published in the following articles:

Paper I (Ref. [43])

SQUID magnetometry combined with in-situ cyclic voltammetry: A case study of tunable magnetism of γ-Fe_2O_3 nanoparticles

S. Topolovec, P. Jerabek, D. V. Szabó, H. Krenn, R. Würschum

J. Magn. Magn. Mater. **329** (2013) 43.

Author Contributions: S. Topolovec designed the electrochemical cell, performed all experimental work and data analysis, drafted and wrote the manuscript and edited the final version together with the co-authors. The SQUID measurements were supported by P. Jerabek and H. Krenn. D. V. Szabó synthesized the γ-Fe_2O_3 nanoparticles. R. Würschum supervised the project and the writing of the manuscript.

Parts of this publication are included in Chapter 5 of this thesis.

Paper II (Ref. [44])

In-situ monitoring magnetism and resistance of nanophase platinum upon electrochemical oxidation

E.-M. Steyskal*, S. Topolovec*, S. Landgraf, H. Krenn, R. Würschum

Beilstein J. Nanotech. **4** (2013) 394.

*Both authors contributed equally to this work.

Author Contributions: S. Topolovec designed the electrochemical cell for the SQUID measurements and performed all experimental work and data analysis concerning the magnetic studies. E.-M. Steyskal performed all experimental work and data analysis concerning the studies of the electrical resistance. The manuscript was drafted and written by E.-M. Steyskal in collaboration with S. Topolovec and the final editing was performed together with the co-authors. The SQUID measurements were supported by H. Krenn. S. Landgraf contributed to the interpretation of the electrochemical data. R. Würschum supervised the project and the writing of the manuscript.

Parts of this publication are included in Chapter 5 of this thesis.

Paper III (Ref. [45])

Electrochemical cell for in-situ electrodeposition of magnetic thin films in a superconducting quantum interference device magnetometer

S. Topolovec, H. Krenn, R. Würschum

Rev. Sci. Instrum. **86** (2015) 063903.

Author Contributions: S. Topolovec designed the electrochemical cell, performed all experimental work and data analysis, drafted and wrote the manuscript and edited the final version together with the co-authors. The SQUID measurements were supported by H. Krenn. R. Würschum supervised the project and the writing of the manuscript.

Parts of this publication are included in Chapters 3 and 4 of this thesis.

Paper IV (Ref. [46])

Enhanced magnetic moment of ultrathin Co films measured by in-situ electrodeposition in a SQUID

S. Topolovec, H. Krenn, R. Würschum

J. Magn. Magn. Mater. **397** (2016) 96.

Author Contributions: S. Topolovec designed the electrochemical cell, performed all experimental work and data analysis, drafted and wrote the manuscript and edited the final version together with the co-authors. The SQUID measurements were supported by H. Krenn. R. Würschum supervised the project and the writing of the manuscript.

Parts of this publication are included in Chapter 4 of this thesis.

Paper V (Ref. [47])

In-operando SQUID magnetometry on Li_xCoO_2 during charging/discharging

S. Topolovec, H. Kren, G. Klinser, S. Koller, H. Krenn, R. Würschum

Manuscript submitted for publication

Author Contributions: S. Topolovec designed the electrochemical cell, performed the measurements and data analysis of the in-operando studies, drafted and wrote the manuscript including the discussion and edited the final version together with the co-authors. H. Kren and S. Koller supported the design and assembly of the electrochemical cell. The ex-situ SQUID measurements and their data analysis and interpretation were performed by G. Klinser in the framework of his master thesis, which was co-supervised by the author of this thesis. The SQUID measurements were supported by H. Krenn. R. Würschum supervised the project and the writing of the manuscript.

Parts of this publication are included in Chapter 6 of this thesis.

CHAPTER 2

Electrochemical processes at the electrode-electrolyte interface

Since this thesis aims to study the correlations between magnetic properties and electrochemical processes, a short overview of the most fundamental electrochemical processes occurring at the electrode-electrolyte interface is given in this chapter. Section 2.1 deals with the electrochemical double layer, which forms at the phase boundary between the electrode and the electrolyte and which can be used for interfacial charging. The specific adsorption of electrolyte species on the electrode, including the deposition of metal ions, is addressed in Section 2.2.

2.1 Electrochemical double layer used for interfacial charging

Upon immersing a metal electrode in a liquid electrolyte, the different chemical potentials in the two phases give rise to a certain amount of electron transfer reactions, which occur until the chemical potential is equal in both phases. In case that the electrolyte contains ions (Me^{z+}) of the same metal, the following reaction occurs at the surface of the metal electrode:

$$Me^{z+} + ze^- \rightleftharpoons Me. \tag{2.1}$$

For an inert electrode, which does not participate in the reaction, likewise a redox reaction

$$S_{ox} + ne^- \rightleftharpoons S_{red} \tag{2.2}$$

takes place at the electrode surface. Herein, S_{ox} and S_{red} denote the oxidized and reduced species in the solution, respectively, and n is the number of transferred electrons. In this

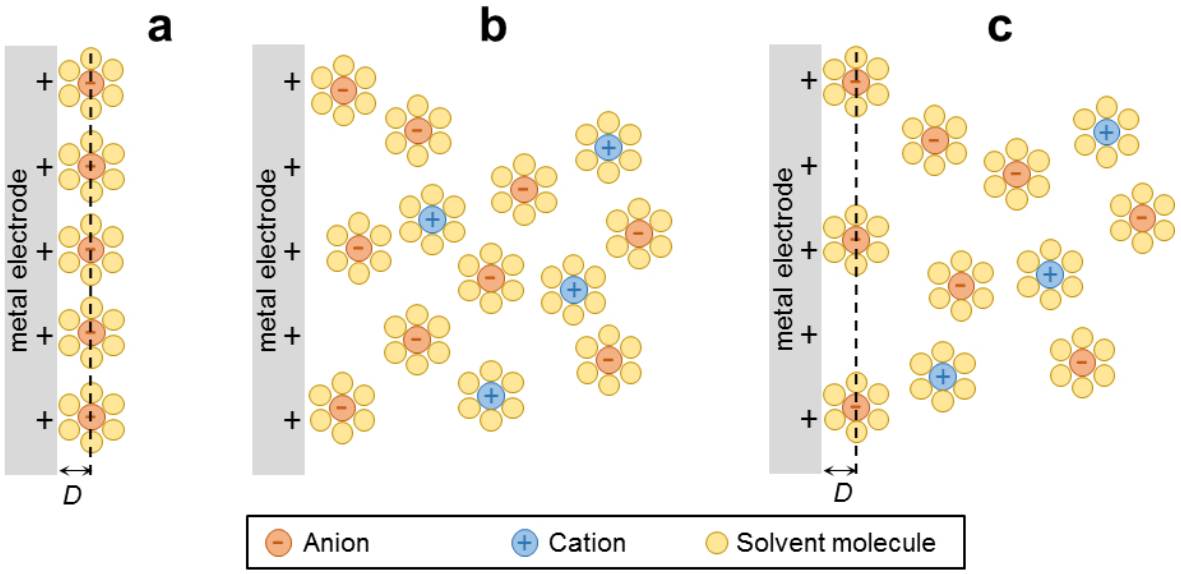

Figure 2.1: Sketch illustrating the different models of the electrochemical double layer at the electrode-electrolyte interface. (a) Helmholtz model, (b) Diffuse double layer model according to Gouy and Chapman, (c) Stern model combining the two other models. D denotes the distance between the Helmholtz plane and the electrode surface.

case, the electrode serves solely as electron donor or acceptor.

Depending on the direction of these reactions, electrons are accumulated or depleted at the surface of the metal electrode. This excess charge is compensated by attracting counterions in the solution to the electrode surface. Thus, a region of two layers with opposite net charge, the so-called electrochemical double layer, is formed at the phase boundary between the electrode and the electrolyte. In the metal electrode, the strong electron screening due to the high density of free electrons confines the surface charge to a relative narrow region. The penetration depth into the metal can be estimated applying the Thomas-Fermi theory and is typically about 1 Ångstrom [40, 48, 49].

Various models of the electrochemical double layer exist for the solution. The three most fundamental ones will be discussed briefly. The most simple and oldest model, the so-called Helmholtz model (see Fig. 2.1a), is based on the notion that the counterions are located in a plane parallel to the metal surface. This plane is separated from the metal surface by a dielectric layer of solvent molecules. In analogy to a conventional parallel plate capacitor, a capacitance per unit area

$$C_H = \frac{\epsilon_0 \epsilon_r}{D} \tag{2.3}$$

can be calculated according to this model. Herein, ϵ_0 denotes the vacuum permittivity, ϵ_r the electrolyte dielectric constant and D the distance between the two layers. This distance

is determined by the size of the solvation shell of the ions and is approximately given by the half diameter of the solvated ions, which is in the order of 0.2 nm [50]. Hence, the dielectric thickness in the electrochemical double layer is significantly smaller than that in a conventional capacitor and, therefore, the electrochemical double layer exhibits a very high capacitance. In particular, with the dielectric constant of water of ϵ_r=78, a capacitance C_H of 345 μF/cm^2 is obtained according to eq. (2.3). This value is, however, considerably higher than the experimentally observed ones, which usually lie between 5-50 μF/cm^2 [50], indicating the limits of this simple Helmholtz model.

An alternative model, the so-called diffuse double layer model (see Fig. 2.1b) proposed by Gouy and Chapman, takes into account the thermal motion of the ions in the solution of the electrochemical double layer. In this model, the distribution of the counterions and the potential are described by the Poisson-Boltzmann equation. The counterions are not fixed anymore in a plane, but are spread out into the solution forming a diffuse layer. This layer consists of ions of both signs, with the counterion concentration increasing towards the surface. However, also this model fails to describe most of the experimental data [51, 52].

Agreement between theory and experiment was achieved by the model of Stern [51, 52], which combines the two approaches by Helmholtz and by Gouy-Chapman (Stern model, see Fig. 2.1c). In this model, a part of the counterions forms a plane close to the electrode as suggested by Helmholtz, denoted the compact Helmholtz layer. Outside of this layer, a diffuse layer as suggested by Gouy and Chapmann, is present. Hence, the charge that compensates the charge in the metal electrode is located partly in the Helmholtz layer and partly in the diffuse layer. According to this model, the overall capacitance C_{DL} of the electrochemical double layer is given by the series capacitance of the Helmholtz layer (C_H, see eq. (2.3)) and of the diffuse layer (C_{diff}):

$$\frac{1}{C_{DL}} = \frac{1}{C_H} + \frac{1}{C_{diff}}. \tag{2.4}$$

For this thesis, the exact description of the electrochemical double layer is of less relevance than the mere fact that its capacitance is quite high and, therefore, also the electric field that can be generated at the metal-electrolyte interface by double layer charging. This electric field can be varied in a defined manner by an external voltage, which controls the charging of the double layer. Assuming a double layer capacitance C_{DL} of 30 μF/cm^2 and an applied potential U of 1 V, which is reasonable for an aqueous electrolyte, electric fields of up to 5×10^8 V/m can be generated. As shown in Chapter 5, this high electric fields can be used to reversibly tune the magnetic properties of high surface area nanomaterials.

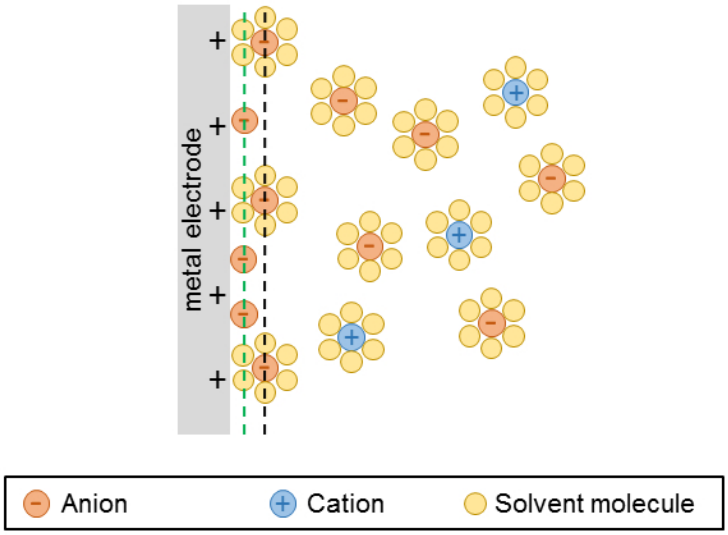

Figure 2.2: Stern model of the electrochemical double layer, in the case of specific adsorbed ions at the metal electrode. The black and green dashed line indicate the outer and inner Helmholtz plane, respectively.

2.2 Adsorption of ions and metal electrodeposition

As shown in Chapter 5, not only the electrostatic effects in the electrochemical double layer, but also the adsorption of ionic species from the electrolyte on the electrode plays another important role for the charging-induced property tuning. Furthermore, adsorption is a fundamental process taking place during metal electrodeposition, which is dealt with in Chapter 4.

In most cases, adsorption is caused by the chemical interaction between the electrode and the adsorbate (chemisorption), whereas weaker interactions such as van der Waals forces (physisorption) cause adsorption just in rare cases [53]. Adsorption of a distinct ion species at the electrode requires that the interaction between this species and the electrode is stronger than the interactions of this ion species within the solvent. "Specific adsorption" denotes the case where the adsorbing ions loose their solvation shell (at least partly), giving rise to a direct, strong bonding at the electrode surface (mostly by forming a chemical bond). Since anions have a weaker bound solvation shell than cations due to their larger ionic radius, they are more likely to be specifically adsorbed. In the case of specific adsorption, the above mentioned Stern model of the electrochemical double layer has to be further modified. As indicated in Fig. 2.2, the Helmholtz plane is separated in an outer plane, which passes through the center of the solvated ions, and in an inner plane, passing through the center of the specifically adsorbed ions.

The specific adsorption of a metal ion on the electrode is a fundamental step, which also takes place during metal electrodeposition. In general, electrodeposition refers to the formation of a metallic film onto a substrate through the electrochemical reduction of metal ions from the electrolyte [48, 54]. The metal ion takes up one or more electrons from the electrode (substrate) and is deposited as metal atom on its surface. Thin film growth by electrodeposition consists of the following steps: (i) Diffusive transport of the metal ions in the solution to the surface, (ii) specific adsorption of the metal ions on the substrate surface, including the stripping of the solvation shell and the charge transfer reaction, (iii) diffusion on the metal surface with subsequent nuclei formation or atom attachment at step surfaces, resulting in the formation of a metallic layer.

CHAPTER 3

Experimental techniques and procedures

In this chapter, the basics of the experimental methods and set-ups, which were applied in the present work, are described[a]. Section 3.1 deals with the electrochemical characterization and Section 3.2 outlines the underlying measurement principle of the used SQUID magnetometer. In Section 3.3, the resulting constraints and demands for the design of the electrochemical cell for the in-situ measurements in the SQUID are elucidated. The detailed experimental parameters and procedures used for each measurement can be found in the respective sections of Chapters 4-6.

3.1 Electrochemical characterization

The majority of the electrochemical measurements were performed with an Autolab PGSTAT 128N potentiostat/galvanostat controlled by Nova software (Metrohm Autolab, Utrecht, Netherlands). For in-situ charging of the γ-Fe_2O_3/Pt nanocomposite pellet in the SQUID magnetometer (see Sec. 5.3.2), a PGZ 100 potentiostat/galvanostat controlled by VoltaMaster software (Radiometer Analytical, Villeurbanne Cedex, France) was used.

All electrochemical experiments were conducted in a three-electrode set-up, which is necessary to obtain reliable results, especially for cyclic voltammetry (see Sec. 3.1.1) measurements [48, 50, 55–57]. In such a set-up, the investigated sample (Pt pellet, γ-Fe_2O_3/Pt nanocomposite pellet, Li_xCoO_2 cathode) or the substrate used for electrodeposition serves as working electrode (WE). The potential of the WE is measured with respect to the refer-

[a] As mentioned in the introduction of this thesis (Chapter 1), parts of the content of this chapter are based on a published article (Paper III, Ref. [45]).

ence electrode (RE). To ensure a constant potential of the RE and to minimize the ohmic voltage drop, the current flowing through the RE is limited by picking up the RE-signal with a high-impedance input of the potentiostat. Current flow through the WE is enabled by means of the counter electrode (CE).

3.1.1 Cyclic voltammetry

Cyclic voltammetry is an electrochemical measurement method, which allows to determine the potentials and mechanisms of redox reactions occurring at the WE. During such a measurement, the potential U between the WE and the RE is swept linearly between an upper (U_{up}) and lower potential limit (U_{low}). When one of these two limits is reached, the potential scan direction is reversed, leading to the triangle shaped potential function shown in Fig. 3.1a. The variation of the potential occurs with a defined scan rate $v = \frac{dU}{dt}$, ranging typically from a few mV/s to a few V/s [50,58]. In the case of nanoporous electrodes, as used for the measurements in Chapter 5, even lower scan rates are necessary because of the limited transport kinetics in the porous structure. To obtain the so-called cyclic voltammogram (CV), the current i flowing between the WE and CE is plotted as a function of the potential U. The current i consists of two superimposed components. The nearly constant charging current of the electrochemical double layer (see Sec. 2.1) and faradaic currents, which result from charge transfer reactions or specific adsorption/desorption processes at the WE and give rise to the formation of current peaks in the CV.

As an example, the CV of a porous nanophase Pt pellet measured in 1 M KOH is shown in Fig. 3.1b. The pellet is made from commercial Pt nanoparticles (for details on the sample preparation see Sec. 5.2). For Pt, the ongoing processes are well documented in literature (see e.g. [59–61]). Starting the potential scan from $-300\,\mathrm{mV}$[b] in anodic direction, a shoulder and plateau of oxygen species adsorption arises between $-250\,\mathrm{mV}$ and $+480\,\mathrm{mV}$. The increase of the current starting at about $+450\,\mathrm{mV}$ indicates the onset of O_2 gas evolution at the WE. After reaching the upper potential limit U_{up} of $+480\,\mathrm{mV}$, the scan direction is reversed. In the cathodic scan, the current is small at first, indicating that the oxygen remains on the Pt surface. At about $-50\,\mathrm{mV}$, the oxygen desorption peak starts to rise and reaches its extremum at about $-350\,\mathrm{mV}$. Lowering the potential further towards the lower potential limit U_{low} of $-1050\,\mathrm{mV}$, three cathodic peaks arise between $-600\,\mathrm{mV}$ and $-1050\,\mathrm{mV}$, which are due to the adsorption of hydrogen on the Pt surface. After reversing

[b] The potentials here are referred with respect to a Ag/AgCl (3 M KCl) reference electrode.

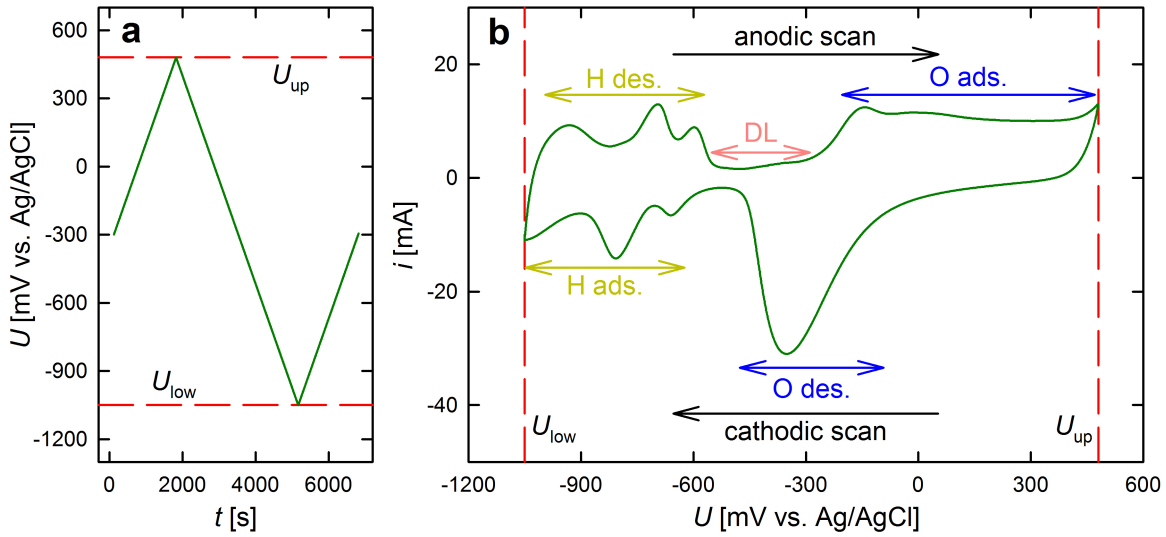

Figure 3.1: Illustration of a cyclic voltammetry measurement. (a) Linear variation of the applied potential U between the upper (U_{up}) and lower (U_{low}) potential limit as a function of time t. (b) Measured current i plotted as a function of the applied potential U. Shown is a cyclic voltammogram (CV) of a porous nanophase Pt pellet in 1 M KOH recorded with a scan rate of v=0.5 mV/s. The arrows indicate the anodic and cathodic scan direction, as well as the potential regions of oxygen adsorption/desorption, hydrogen adsorption/desorption and of the electrochemical double layer (DL), respectively.

the scan direction and going again to more positive potentials, hydrogen desorption occurs, indicated by the three cathodic peaks in the potential region between −1000 mV and −560 mV. In the following potential region between −530 mV and −300 mV, the current is constant and relatively small, revealing that only charging of the electrochemical double layer takes place. It should be noted that the charging of the electrochemical double layer does not only occur in this potential regime, but also over the whole potential scan outside of this regime, where the charging current of the double layer is superimposed by faradaic currents.

3.2 SQUID magnetometry: Measurement principle

Since the goal of this work is to detected relative small variations of the magnetic moment induced by electrochemical processes, a highly sensitive magnetic measurement technique is required. SQUID (**S**uper Conducting **Qu**antum **I**nterference **D**evice) magnetometry is the perfect choice, because changes of the magnetic moment in the order of 10^{-8} emu[c] can be resolved [62].

The SQUID measurements were performed in collaboration with Prof. Heinz Krenn at the

[c] $1\,\text{emu} = 10^{-3}\,\text{Am}^2$

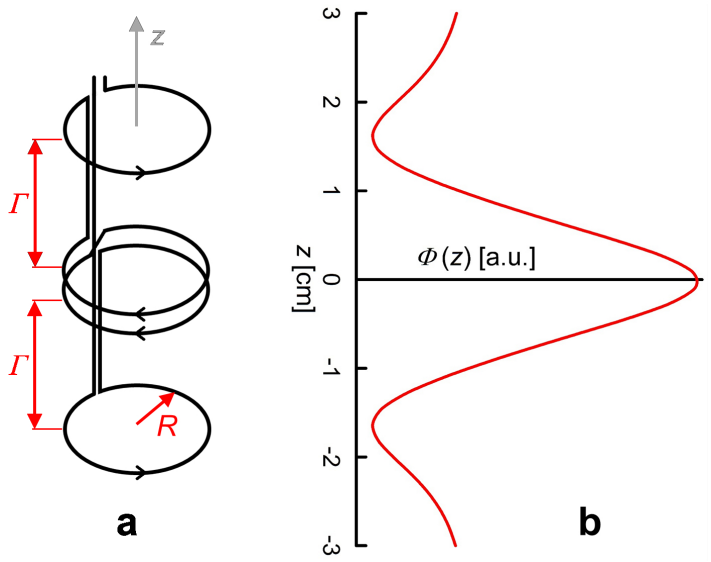

Figure 3.2: (a) Sketch of the SQUID pick-up coils, forming a second order gradiometer. (b) Magnetic flux $\Phi(z)$ induced by a magnetic point-dipole pulled through the coils as a function of the position z. The flux (red curve) is described by eq. (3.1). Pick-up coil radius: R=0.97 cm, distance between the coils: Γ=1.519 cm [63]. The mutual current directions in the coils are indicated by the arrows.

Institute of Physics, University of Graz, using a MPMS®-XL-7 magnetometer (Quantum Design Inc., San Diego, CA, USA). This particular device can detect changes of the magnetic moment of 10^{-8} emu at magnetic fields smaller than 2500 Oe[d] and of 6×10^{-8} emu at magnetic fields up to 70 kOe [62]. In this chapter, the measurement principle of a SQUID magnetometer is described based on this MPMS® SQUID magnetometer system of Quantum Design Inc., which is the most widely used commercial SQUID system [62]. Also the design of the electrochemical cells presented in this work focuses on this system. Nevertheless, the present approach can be adapted for any other SQUID system as well, since the configuration and the measurement principle of other SQUID magnetometers are similar.

In order to measure the magnetic moment m with the MPMS®, the sample is pulled through a set of superconducting pick-up coils forming a second order gradiometer. The sample is moved over a predefined scan length in discrete steps along the z-axis of the gradiometer (see Fig. 3.2a). For the measurements presented in this work, scan lengths of either 4 or 6 cm were used, recording either 32 or 64 data points per scan. Translation of the sample induces a magnetic flux change $\Phi(z)$ in the pick-up coils, which is proportional to the magnetic dipole moment m of the sample. Assuming the sample to be an ideal magnetic point dipole, the magnetic flux change $\Phi(z)$ shown in Fig. 3.2b is obtained. The associated change of the flux-screening super-current through the pick-up coils is inductively coupled to

[d] 1 Oe = $\frac{1000}{4\pi}\ \frac{\mathrm{A}}{\mathrm{m}}$

a radio-frequency SQUID sensor, which transforms the magnetic flux change $\Phi(z)$ into the SQUID output voltage $U(z)$. The magnetic moment m is obtained from this raw data by applying a least square regression fit, using the theoretical response function of a magnetic point dipole [63]

$$U(z) = P_1 + P_2 \cdot z + P_3 \cdot \Big\{ 2 \cdot \Big[R^2 + (z + P_4)^2\Big]^{-3/2} - \Big[R^2 + (\Gamma + z + P_4)^2\Big]^{-3/2} - \Big[R^2 + (-\Gamma + z + P_4)^2\Big]^{-3/2} \Big\}. \quad (3.1)$$

Herein, R=0.97 cm denotes the radius of the pick-up coils and Γ=1.519 cm the distance between the coils [63] as shown in Fig. 3.2a. A constant and a z-linear background signal are represented by the parameter P_1 and the term $P_2 \cdot z$, respectively. The parameter P_4 allows for small displacements of the sample along the z-axis with respect to the center of the gradiometer. The magnetic moment m is proportional to the amplitude P_3 and can be derived from the formula

$$m = P_3 \times \frac{f_{lr}}{f_{cal} \times f_{sens} \times f_{corr}}. \quad (3.2)$$

Herein, f_{lr} denotes the device-dependent longitudinal regression factor, f_{cal} the SQUID calibration factor[e]. f_{sens} is a sensitivity factor, which depends on the measurement range used[f], and f_{corr}=0.9125 a correction factor given by the manufacturer of the SQUID magnetometer [63]. The approximation of a point like sample can be used without any further correction as long as the sample is small in comparison to the coil radius of the gradiometer and the coil separation. For a sample size smaller than 3x3 mm^2, the relative error is below 1% [62].

3.3 Constraints and demands for electrochemical cell design for in-situ measurements in a SQUID

One of the most challenging tasks of this thesis was to develop an electrochemical cell design suitable for reliable in-situ measurements in the SQUID magnetometer and thus allowing simultaneous electrochemical and magnetic measurements. The cell design established by T. Traußnig in his PhD thesis [18, 24] served as a base. The improvements made by the author of this thesis concern especially the reduction of the magnetic background signal of the cell and the implementation of a third, separate reference electrode. With the reduced

[e] For the used SQUID system these factors are f_{lr}=1.825 and f_{cal}=7342.468.

[f] For the measurement range used for the Co electrodeposition experiments presented in Chapter 4, the sensitivity factor f_{sens} is 5.

magnetic background signal of the new cell design, measurements of the magnetic moment of paramagnetic samples (e.g. Pt, Li_xCoO_2) and ultrathin films become possible. The new third electrode enables in-situ cyclic voltammetry measurements, and consequently a more precise and reliable correlation between the detected variations of the magnetic moment and the electrochemical processes occurring at the investigated electrode.

In this section, the constraints and demands which have to be taken into account for the design of the electrochemical cell are described. Since the actual cell design varies somewhat for the three different topics studied in this thesis – electrodeposition of Co films (Chapter 4), electrochemical tuning of magnetism (Chapter 5) and in-situ studies of the magnetic moment of Li_xCoO_2 cathodes (Chapter 6) – the exact set-up of the electrochemical cells used is presented in the respective Sections 4.2.1, 5.2.2 and 6.3.1.

The construction of the MPMS® and the used measurement principle described in Section 3.2, impose the following constraints and demands for the cell design:

(i) The diameter of the cell is limited by the sample space inside the MPMS® which has an inner diameter of 9 mm.

(ii) For using liquid electrolytes, the cell has to be vacuum-tight, since it is exposed to vacuum during the transfer into the magnetometer and to a He-atmosphere of a few mbar during the measurements [64].

(iii) The cell design should allow an easy attachment of the cell to the SQUID sample transfer rod.

(iv) As a major demand, the cell should affect the magnetic signal measured by the SQUID as less as possible. One way to minimize the influence of the cell is to use only diamagnetic materials for the cell assembly. However, this alone is not sufficient to reduce the background signal of the cell to allow reliable measurements on paramagnetic electrodes or magnetic thin films[g]. Considering the measurement principle of the SQUID, there is a further, more efficient way to reduce the magnetic background signal by suitable cell design. As can be seen from Section 3.2, each part of the cell leading to a change of the magnetic flux upon translation in the pick-up coils affects the induced output voltage and, therefore, the magnetic moment m calculated by eq. (3.2). There are two ways to prevent such flux changes induced by the cell and to ensure that the

[g] Since the γ-Fe_2O_3 nanoparticles investigated in Chapter 5 exhibit a high magnetic moment, the usage of diamagnetic material for the cell assembly was sufficient to reduce the background signal of the cell and to enable measurements of the variation of the magnetic moment of the γ-Fe_2O_3 particles.

measured signal arises exclusively from the investigated sample (working electrode) or the electrodeposited film rather than from the cell periphery: On the one hand, parts of the cell that are located far enough outside the pick-up coils, on the other hand, long homogenous parts that extend well beyond all three pick-up coils during the sample movement, do not lead to a flux change in the coils. Thus, these parts do not contribute to the measured magnetic moment.

Beside these constraints for the magnetic moment detection, electrochemistry puts further demands on the cell:

(v) As already mentioned in Section 3.1, a cell including three electrodes is necessary for reliable electrochemical, and especially for cyclic voltammetry, measurements.

(vi) All materials used for the cell assembly must be resistant against the electrolyte and the solvent.

(vii) To avoid contaminants in the electrodeposited film and at the investigated working electrode, a material, that is insoluble at the applied potentials has to be used as counter electrode.

(viii) To prevent that the kinetics at the counter electrode limit the occurring electrochemical processes, a high surface material has to be used as counter electrode for the measurements on the nanoporous electrodes presented in Chapter 5.

CHAPTER 4

In-situ electrodeposition of thin Co films

4.1 Introduction

Over the last few decades, the magnetic properties of magnetic thin films have been subject of intense research[h]. The continuous interest in this topic is not only due to its technological relevance (e.g. applications in information technology), but also stems from the fact that the magnetic properties of magnetic thin films can bring important contributions to a fundamental understanding of the physics of magnetism [65, 66].

The high amount of interfaces and surfaces in magnetic thin films leads to different magnetic properties compared to the bulk. This is on the one hand due to the lower coordination number of the magnetic atoms at the interface/surface. On the other hand, the reduced symmetry at the interface/surface leads to modified electronic interactions, resulting in varied magnetic properties. Indications for such variations are, for instance, altered magnetic anisotropies, magnetic exchange constants or absolute magnetic moments per atom of thin films compared to the bulk (see [65] for a review).

Measuring these deviations from the bulk magnetic properties is experimentally quite challenging. Especially in the case of the magnetic moment, methods having a monolayer sensitivity and providing absolute values are required. In principle, SQUID magnetometry would be an ideal technique because of its ability to measure absolute magnetic moments and to resolve changes of the magnetic moment in the order of 10^{-8} emu [62]. However,

[h] As mentioned in the introduction of this thesis (Chapter 1), parts of the content of this chapter are based on published articles (Paper III, Ref. [45] and Paper IV, Ref. [46]).

the application of SQUID magnetometry to determine the magnetic moment of thin films is limited by the fact that also the magnetic moment of the significantly thicker substrate is measured by this integral method and that an accurate subtraction of this signal is difficult [65, 67, 68]. Therefore, in most cases, other, more indirect methods such as polarized neutron reflection (PNR) or x-ray magnetic circular dichroism (XMCD) are used to measure the absolute magnetic moment of ultrathin films (see [65] and references therein).

One way to correct the magnetic background signal of the substrate in integral SQUID measurements precisely would be the in-situ growth of the magnetic thin film in the SQUID magnetometer. Since the background signal would be exactly the same before, during and after the growth, measurements of the absolute magnetic moment of ultrathin films in a SQUID magnetometer should become possible. Further, the oxidation of the thin film could be prevented by the in-situ growth. For such an in-situ growth, a suitable preparation technique has to be chosen. The standard preparation techniques of magnetic thin films, such as molecular beam epitaxy (MBE), pulsed laser deposition (PLD) and sputtering [69], cannot be implemented in a commercial SQUID magnetometer because of the limited sample space in the SQUID and the requirement for UHV conditions. As an alternative, electrodeposition, which has developed as a suitable preparation technique of magnetic thin films over the last years [3–5], can be used, since it can be conducted in the limited sample space and does not require UHV conditions. As further benefits, electrodeposition facilitate an easy adjustment of the film thickness and enables not only the creation of the film but also its subsequent dissolution. Therefore, it is ideally suited for in-situ measurement of the magnetic properties of thin films during their growth and dissolution.

So far, only few in-situ characterization techniques during electrodeposition of magnetic thin films have been developed and applied, such as magneto-optical Kerr effect (MOKE) [4, 5, 22, 25–33], alternating gradient field magnetometry (AGFM) [5, 29, 34–38] and ferromagnetic resonance (FMR) [39] measurements. Whereas these measurements yield information about spin orientation, coercivity and ratio between the remanent and saturation magnetization, only relative values of the magnetic moment are obtained by these methods. The absolute magnetic moment, which is one of the most fundamental magnetic properties, could not be measured in-situ so far.

To enable such in-situ measurements of the magnetic moment of thin films, an electrochemical cell for in-situ electrodeposition in a SQUID magnetometer is design. As shown in this

chapter, the proper design of this cell (Sec. 4.2.1) and the implemented data evaluation procedure (Sec. 4.2.2) enable a complete elimination of the magnetic background signal including the substrate. Therefore, the absolute magnetic moment, which arises exclusively from the deposited magnetic thin film during its growth and subsequent dissolution, can be determined precisely. The feasibility and reliability of this set-up first is demonstrated by means of the electrodeposition of a Co film of several atomic layers in Section 4.3.1. Then, this novel measurement set-up is applied to study the thickness dependence of the magnetic moment of ultrathin Co films (Sec. 4.3.2). Finally, the obtained results are compared with literature in Section 4.4.

4.2 Experimental: Electrochemical cell and measurement procedure

4.2.1 Electrochemical cell design

Based on the requirements listed in Section 3.3, a cell for in-situ electrodeposition in a SQUID magnetometer has been designed as described in what follows. A sketch of the cell is given in Fig. 4.1; Fig. 4.2 shows photographs of a cell taken at different stages of the cell assembling.

As electrolyte compartment, a 17.78 cm long, thin-walled borosilicate glass NMR tube (505-PS-7, Wilmad-LabGlass, Vineland, NJ, USA) with an outer diameter of 4.96 mm is chosen since it exhibits a low magnetic susceptibility and a high homogeneity. Because of the large length of the compartment extending over all three SQUID pick-up coils, neither the tube itself, nor the electrolyte therein lead to flux changes in the detection coils. The selected tube also fits well into the standard plastic straws used for sample mounting in the MPMS® magnetometer and, therefore, allows an easy attachment to the sample transfer rod.

As well-defined substrate for electrodeposition, stripes (9.8 cm×0.3 cm) of a Au(111)-coated Si(100) wafer (Sigma Aldrich, St. Louis, MO, USA) are used. As shown by Manios et al. [70] the magnetic signal of a substrate of this length vanishes nearly completely. As sketched in Fig. 4.1, the Au-coated side of the substrate is masked with a thin layer of a chemically resistant epoxy resin (Loctite 1C Hysol, Henkel), leaving an area of about $2\times3\,\mathrm{mm}^2$ uncovered in the middle of the substrate for electrodeposition (see Fig. 4.2a). In this area epoxy is also applied on the backside of the substrate (see Fig. 4.2b), in order to achieve a continuous epoxy deposit over the whole length of the substrate so that magnetic

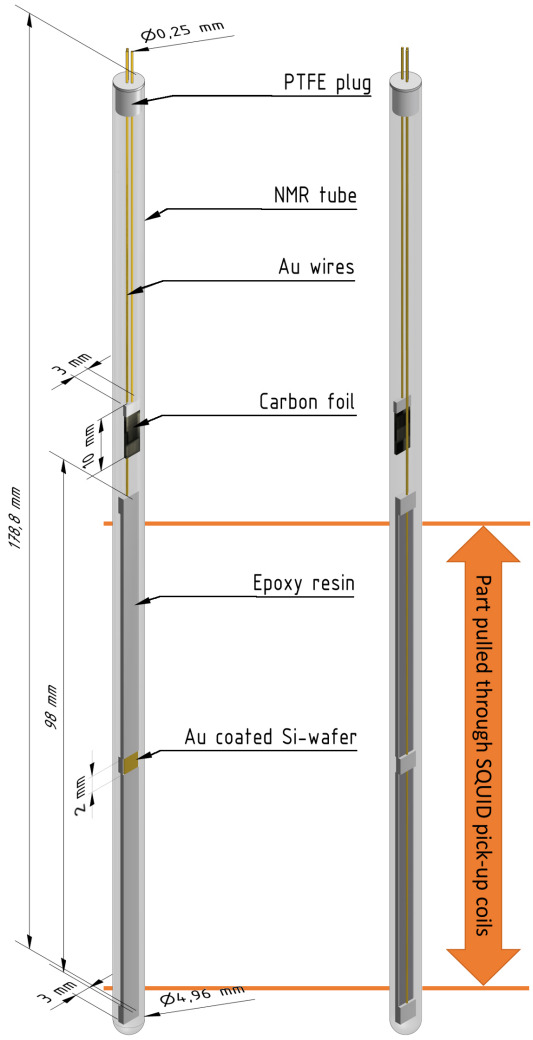

Figure 4.1: Sketch of the electrochemical cell designed for the in-situ electrodeposition of magnetic thin films in a SQUID magnetometer. The large arrow indicates the part of the cell, which is pulled through the SQUID pick-up coils during a measurement scan over a length of 6 cm. Electrolyte and polyethylene tubes for insulating Au wires are not shown in this sketch (see text)[i].

flux changes from the epoxy in the gradiometer coils are suppressed. At the top of the substrate, a thin Au wire (Ø=0.25 mm, 99.9%, ChemPur, Karlsruhe, Germany) is attached by an adhesive tape beneath the epoxy resin for electrical connection to the unmasked Au layer on which the electrodeposition is performed and which serves as working electrode. At the backside of the substrate, an additional Au wire of the same diameter is fixed, using the epoxy dot in the middle and two further ones at the top and bottom end of the substrate (see Fig. 4.2b). This second Au wire serves as quasi-reference electrode. As shown in the sketch of Fig. 4.1, the Au(111)/Si substrate is mounted vertically at the lower end of the NMR tube after cleaning in an ultrasonic bath with ethanol (99.9%, AustrAlco, Spillern, Austria) for 15 min. As counter electrode, a graphite foil, also connected with a Au wire,

[i] The author would like to thank Sandra Winkler for drawing this sketch.

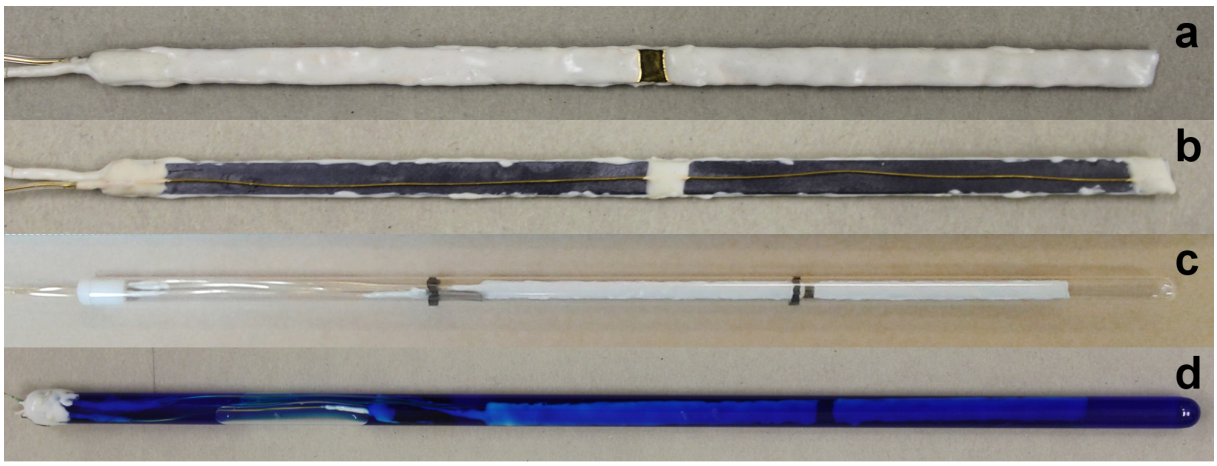

Figure 4.2: Photographs of an electrochemical cell used for in-situ Co electrodeposition in the SQUID magnetometer at different stages of the cell assembling. (a) Au(111)/Si substrate masked with epoxy resin. The deposition takes place at the unmasked window in the center. (b) Backside of the Au(111)/Si substrate with the Au wire acting as quasi-reference electrode fixed by three epoxy dots. (c) Assembled cell not yet filled with electrolyte and sealed with epoxy. (d) Completed cell with electrolyte and sealing. Note that the photographs are rotated 90° counter-clockwise with respect to the vertical measurement position in the SQUID.

is placed about one centimeter above the top end of the substrate (see right side of the left black mark in Fig. 4.2c). The gold wires of the working and the counter electrode are insulated using polyethylene tubes and the same epoxy as for masking (both not shown in Fig. 4.1), thus preventing unwanted electrodeposition on and dissolution from these wires. To avoid short circuits in the cell, the upper part of the wire used as reference electrode is insulated in the same way. The NMR tube is filled with electrolyte (not shown in Fig. 4.1) up to about two centimeters under its top end. The cell is closed with a conical PTFE plug provided with three feedthroughs for the Au wires connecting the three electrodes. The same epoxy as for masking is used to seal the cell. To ensure that the epoxy penetrates into the feedthroughs of the PTFE plug and inbetween the plug and the NMR tube to close the cell properly, it is heated with a heat gun for several seconds, making it more fluid. A photograph of a complete assembled cell is shown in Fig. 4.2d.

In Fig. 4.1, the area of the cell is marked, which is pulled through the magnetometer pick-up coils during a measurement scan of 6 cm. As can be seen from this sketch, all parts of the cell within this area are highly symmetric and homogenous and extend beyond the pick-up coils during the whole sample movement, except the electrodeposited film which grows at the uncovered part of the substrate. The asymmetric parts of the cell, such as the counter electrode, are placed well apart from the coils. Hence, the bare cell should not lead to a magnetic flux change in the pick-up coils and, therefore, the measured magnetic moment

obtained from the induced flux change should originate exclusively from the electrodeposited film. In practice, minor inhomogeneities of the cell within the measuring length arise from thickness variations of the epoxy mask, as it is spread manually and therefore not perfectly homogenous and symmetric, as can be seen in Fig. 4.2a. However, as will be shown, the small remaining contribution to the magnetic signal arising from the cell can be corrected perfectly by the data evaluation procedure, which is presented next.

4.2.2 Data evaluation procedure

Although the magnetic background signal of the cell is already minimized owing to an optimum design, the small remaining background is further eliminated by the data evaluation method: Prior to the onset of the electrodeposition, the residual SQUID output voltage curve $U_{cell}(z)$, which arises from the cell exclusively, is recorded. Even if the output voltage signal is identical within the accuracy of the SQUID for successive scans, an average of 100 measurements is used to determine $U_{cell}(z)$. This curve is afterwards subtracted from the voltage curve measured during the electrodeposition $U_{meas}(z)$, yielding the voltage curve $U_{film}(z) = U_{meas}(z) - U_{cell}(z)$, which arises solely from the electrodeposited film since $U_{cell}(z)$ is exactly the same before and during the electrodeposition. To determine the magnetic moment from this voltage signal, eq. (3.1) is fitted to $U_{film}(z)$ by means of the "nlinfit" function in Matlab® (The MathWorks Inc., Natick, MA, USA). Extracting the amplitude P_3 obtained from this fit, the magnetic moment m_{film} is calculated using eq. (3.2). As stated above, this moment m_{film} arises exclusively from the deposited film.

4.2.3 SQUID measurement procedure

For the in-situ measurements in the SQUID magnetometer, the closed electrochemical cell was mounted into a standard plastic straw, which was attached to a modified sample rod with electrical feedthroughs, connecting the Au leads of the electrodes with a potentiostat placed next to the magnetometer. Since there was no magnetic film deposited when the cell was inserted into the magnetometer, the standard procedure for sample centering [71] could not be applied. For proper vertical centering, the distance between the upper sliding clamp of the sample transfer rod and the sample center was determined by a calibration measurement with a small Pb sphere. For a scan length of 6 cm, a distance of 125.5 cm was obtained. The distance between the clamp and the deposition area of the substrate was adjusted accordingly.

For the Co electrodeposition, 0.2 M $CoCl_2$ (anhydrous, ≥98%, Sigma Aldrich, St. Louis, MO, USA) dissolved in ethanol (99.9%, AustrAlco, Spillern, Austria) was used as electrolyte. The Co films were deposited and subsequently dissolved using cyclic voltammetry (see Sec. 3.1.1). A small scan rate of 0.5 mV/s was employed to ensure that the deposition/dissolution occurs slowly, so that the magnetic moment m_{film} does not change considerably during a measuring scan of the magnetometer. To demonstrate the feasibility by means of a thicker Co film, $U_{low} = -1200$ mV was used as lower potential limit (Sec. 4.3.1). For the thickness-dependent measurements, U_{low} was varied between −1030 mV and −1180 mV (Sec. 4.3.2). Depending on the film thickness, −100 mV or +100 mV was used as upper potential limit. All potentials reported in this chapter are referred to the Au quasi-reference electrode. Reference measurements have shown that in the present electrolyte, this electrode has a potential of about +100 mV vs. a Ag/AgCl (3 M KCl) reference electrode, meaning that the potential value vs. the Ag/AgCl (3 M KCl) can be estimated by subtracting 100 mV from the potential value given with respect to the Au quasi-reference electrode.

The measurements of the magnetic moment were conducted using a scan length of 6 cm with 32 data points recorded in each scan. These settings yielded one measurement point of the magnetic moment every 15 s. All measurements were performed at a temperature of 300 K and at an applied magnetic field of 5 kOe. As well documented by in-situ MOKE measurements [4, 25, 28], the magnetic moment of the Co film is saturated at this field. This was further confirmed by field-dependent measurements on Co films that were electrodeposited ex-situ.

4.3 Results

The result section of this chapter is divided into two parts. In Section 4.3.1, the feasibility and reliability of the presented in-situ electrodeposition approach are demonstrated by means of the electrodeposition of a Co film of several atomic layers. In Section 4.3.2, results of the thickness dependence of the absolute magnetic moment of ultrathin Co films are reported.

4.3.1 Feasibility and reliability of the measurement set-up

Figure 4.3 shows the cyclic voltammogram (CV) for the Co electrodeposition and subsequent dissolution, which was recorded with the in-situ electrochemical cell inside the SQUID

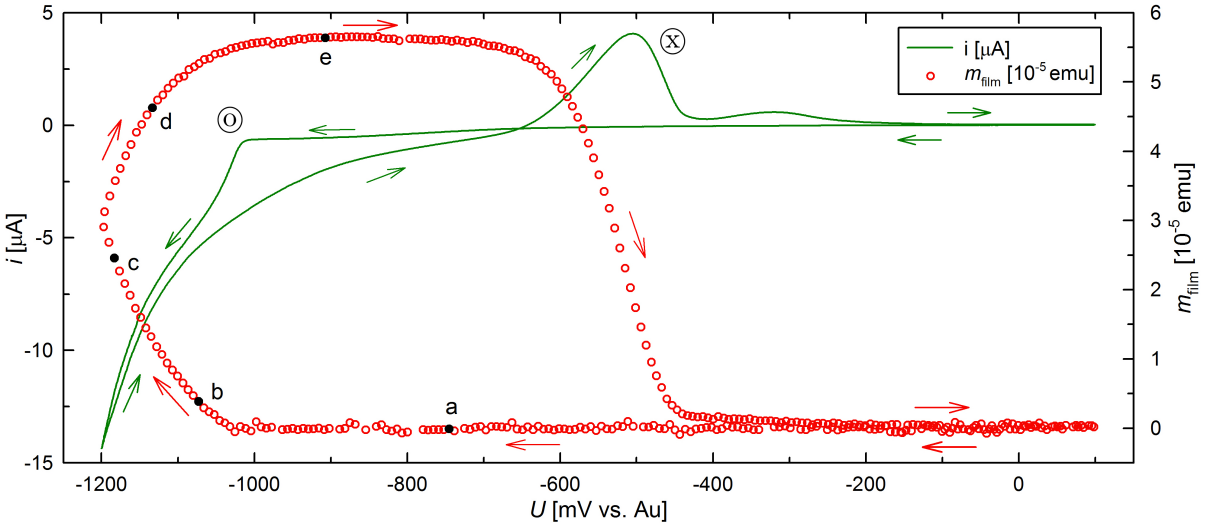

Figure 4.3: Cyclic voltammogram (line) of Co electrodeposition and subsequent dissolution recorded with the in-situ electrochemical cell for the lower potential limit of U_{low}=−1200 mV and the corresponding magnetic moment m_{film} (circles) of the deposited Co film (electrolyte: 0.2 M $CoCl_2$ dissolved in ethanol, substrate: Au(111), scan rate: 0.5 mV/s). The arrows show the direction of the potential sweep. The filled circles, indicated by the letters, mark the data points of the magnetic moment m_{film}, for which the SQUID output voltage curves $U_{film}(z)$ and the corresponding fits are shown in Fig. 4.4b. ⓞ and ⓧ indicate the onset of the Co electrodeposition and the dissolution peak, respectively.

magnetometer for the lower potential limit U_{low} of −1200 mV. The CV exhibits the typical characteristics for Co deposition and subsequent dissolution [72, 73]. The ongoing electrochemical processes are described based on this CV, starting at the upper potential limit U_{up} of +100 mV. Decreasing the potential initially, nearly no current is flowing until a potential of −1015 mV is reached. At $U = -1015$ mV the current drops abruptly to large negative values, signifying the onset of the Co deposition (indicated by ⓞ in Fig. 4.3). The absolute value $|i|$ of the current rises towards the lower potential limit of −1200 mV, signifying an increasing deposition rate. Reversing the scan direction of the potential, the absolute current value $|i|$, thus the deposition rate, decreases again and the deposition comes to halt at a potential of about −950 mV. Increasing the potential further, the rise of the anodic peak at −670 mV indicates the dissolution of the electrodeposited Co film (indicated by ⓧ in Fig. 4.3). When the current is nearly zero again, the Co film is dissolved completely.

The magnetic moment of the electrodeposited Co film m_{film} measured during the electrodeposition is also shown in Fig. 4.3. Starting again at the upper potential limit of +100 mV, m_{film} is initially zero. Decreasing the potential, m_{film} stays zero at first, until, together with the onset of the Co deposition at −1015 mV, m_{film} begins to rise. With further lowering of U, the magnetic moment m_{film} increases progressively with deposition and grows faster at higher deposition rates. Reversing the scan direction of the potential from the

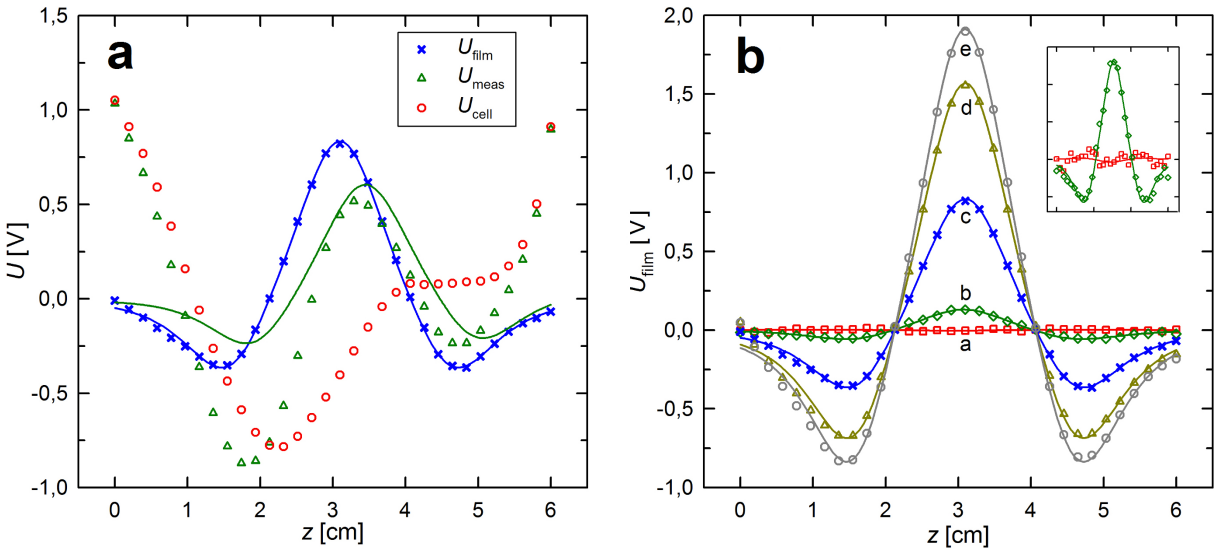

Figure 4.4: Measured SQUID output voltage curves (symbols) and corresponding fits (lines) used to determine the magnetic moment of the electrodeposited Co film m_{film}. (a) Signal prior (U_{meas}) and after (U_{film}) the subtraction of the remaining background signal of the cell (U_{cell}). (b) Examples of U_{film} recorded for different Co film thicknesses corresponding to the data points of m_{film} marked by the letters in Fig. 4.3. The signal in (a) corresponds to the data of c in (b) (blue curves). The inset in (b) shows a zoom of curves a and b.

lower potential limit of $-1200\,\mathrm{mV}$, the rise of m_{film} decelerates consistently with decreasing deposition rate. When the deposition ceases at about $-950\,\mathrm{mV}$, the rise of m_{film} stops and m_{film} remains constant with a further potential increase until the onset of the anodic dissolution peak is reached at a potential of $-670\,\mathrm{mV}$. Then, m_{film} decreases along with the dissolution of the Co film, showing the fastest decline at the highest dissolution currents. After the entire Co film is dissolved, m_{film} is zero again.

In summary, Fig. 4.3 clearly demonstrates that the custom-designed electrochemical cell allows to monitor the magnetic moment of the Co film m_{film} continuously during its growth and subsequent dissolution. The growth and dissolution can be repeated several times, yielding reproducible results (not shown). Further, by comparing the progressions of the current i and the magnetic moment m_{film}, it becomes obvious from Fig. 4.3 that the current i does not influence the measured magnetic moment m_{film}. For instance, m_{film} is constant after the deposition stops in the reverse scan at a potential of about $-950\,\mathrm{mV}$, whereas the current i, which is caused by side reactions, clearly shows a decrease in this potential region.

In order to check that the measurement set-up together with the presented data evaluation method yields reliable values of the magnetic moment of the electrodeposited Co film, the SQUID output voltage curves and the corresponding fits of some data points of Fig. 4.3 are shown in Fig. 4.4. In Fig. 4.4a, the voltage curves before ($U_{meas}(z)$) and after ($U_{film}(z)$)

the correction of the residual background signal of the cell ($U_{cell}(z)$) are plotted for the state marked by the letter c in Fig. 4.3. The initially measured voltage curve $U_{meas}(z)$ obviously differs from the theoretical response function of a magnetic point dipole, shown in Fig. 3.2b. Therefore, the corresponding fit does not coincide with the curve. This deviation occurs because $U_{cell}(z)$ cannot be suppressed completely, as can be seen in Fig. 4.4a. This is probably due to inhomogeneities (e.g. uneven distribution of the epoxy resin) in the actual cell set-up. However, after subtracting the contribution of the cell (including the substrate and epoxy), the signal $U_{film}(z) = U_{meas}(z) - U_{cell}(z)$ coincides perfectly with the corresponding fit. Hence, m_{film}, determined by eq. (3.2) after fitting eq. (3.1) to $U_{film}(z)$, results in an accurate value of the absolute magnetic moment of the electrodeposited film.

Figure 4.4b shows $U_{film}(z)$ for different states during the film growth, which clearly indicates that the method of data correction works well for all film thicknesses. For data point a in Fig. 4.3, where no Co film has been deposited, only a small noise of $U_{film}(z)$ around zero occurs (curve a in Fig. 4.4b), leading to m_{film} of nearly zero. The rise of m_{film} during the film growth can be discerned from the increasing amplitude of $U_{film}(z)$ going from the data points b to e. Even right after the onset of the deposition (data point b in Fig. 4.3, curve b in Fig. 4.4b), $U_{film}(z)$ coincides well with the corresponding fit. Thus, reliable values of the magnetic moment of ultrathin magnetic films can be obtained with the presented measurement set-up. In fact, the magnetic moment of data point b of 3.85×10^{-6} emu corresponds to approximately 2 atomic layers and even lower thicknesses can be unambiguously detected (see data points right from b in Fig. 4.3).

The reliability of the measurements can be further demonstrated by calculating the magnetic moment per deposited Co atom as shown in the following. The maximum number N_{Co} of deposited Co atoms during the CV cycle can be calculated from the consumed charge. Since the electrodeposition is accompanied by simultaneous H_2 gas evolution, the charge of the anodic dissolution peak Q_A has to be used [28]. In order to quantify Q_A from the CV, the background current has to be taken into consideration by an extrapolation of the baseline current left and right of the peak. The extrapolation was performed by means of the software of the potentiostat (Nova 1.10, Metrohm Autolab, Utrecht, Netherlands) using an exponential function. Since the progression of the baseline is not unambiguous, the extrapolation was repeated 14 times using different baselines. Most of these baselines differ only slightly, since a certain baseline form was found to be the best for describing the data according to visual judgment of the author. Minimum and maximum baselines,

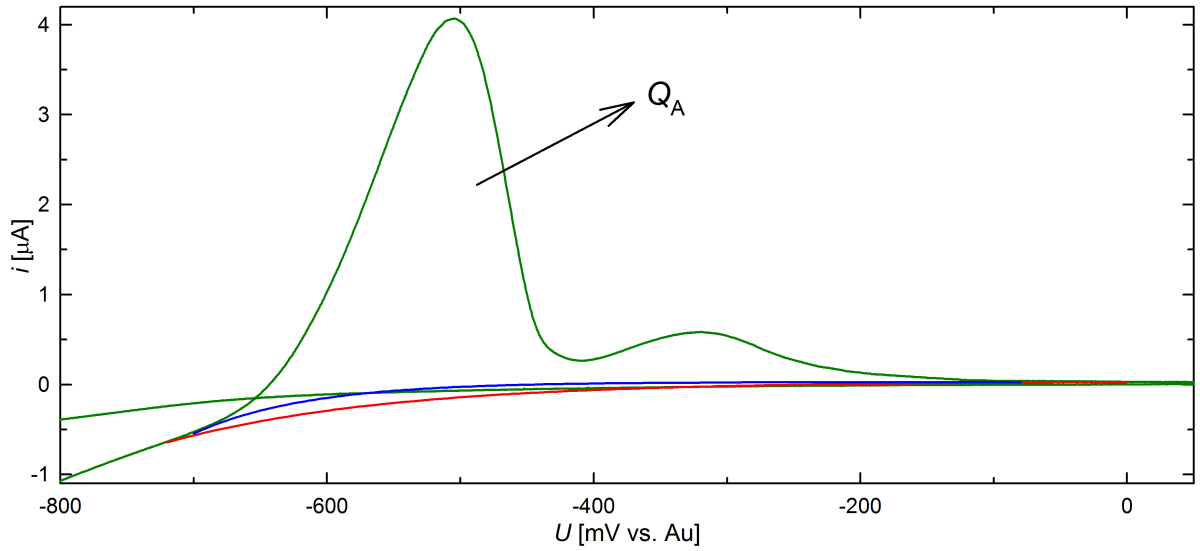

Figure 4.5: Magnification of the anodic dissolution peak area of the cyclic voltammogram (green line) of Co deposition and subsequent dissolution shown in Fig. 4.3. The red and blue lines are the maximum and minimum baselines applied to quantify the charge of the anodic dissolution peak Q_A (see text).

which still describe the background current reasonably, were taken as the error of the charge determination. In this way, a charge of $Q_A = 1.11^{+0.08}_{-0.04}\,\mathrm{mC}$ was determined for the anodic dissolution peak of the CV shown in Fig. 4.3. The obtained error is asymmetric since the average of the 14 baselines assumed by the author deviate to different extents from the maximum and minimum ones. To illustrate the sensitivity of the charge determination on the applied baseline, the minimum and maximum baselines applied to quantify Q_A are plotted in Fig. 4.5. Even if the two baselines do not differ extensively, the resulting charge varies by 11 %.

Considering that two electrons are transferred per Co atom ($Co^{2+}+2e^- \rightarrow Co$), the obtained charge of $Q_A = 1.11^{+0.08}_{-0.04}\,\mathrm{mC}$ corresponds to a maximum number N_{Co} of deposited Co atoms of $3.47^{+0.26}_{-0.12}\times10^{15}$. Relating this maximum amount of deposited Co to the maximum value of the magnetic moment m_{film} of $(5.62\pm0.04)\times10^{-5}$ emu[j], which occurs in the potential region between $-950\,\mathrm{mV}$ and $-660\,\mathrm{mV}$ (see Fig. 4.3), yields a magnetic moment of $1.75^{+0.08}_{-0.13}\,\mu_B$ per Co atom. This value coincides well with the bulk value of hcp Co which is equal to $1.72\,\mu_B$ for a temperature of 287 K [74][k]. As shown by structural characterization measurements the formation of hcp Co is expected for Co electrodeposition on Au(111) [5, 34], although the concurrent formation of a minor fcc phase cannot be excluded [75]. However, the minor

[j] The given error of m_{film} accounts for the noise of m_{film} in the potential region between $-950\,\mathrm{mV}$ and $-660\,\mathrm{mV}$ in Fig. 4.3.

[k] Our measurements were performed at 300 K. 287 K is the temperature closest to 300 K for which a value of the magnetic moment is given in [74].

difference of the magnetic moment of fcc and hcp Co of $0.03\,\mu_B$ [74] is less than the presented experimental uncertainty.

To ascertain if bulk behavior is reasonable for the present measurement, the thickness of the Co film has to be determined. In-situ STM measurements predict a layer-by-layer like growth for Co electrodeposition on Au(111), which starts with the nucleation of monoatomic high islands and the formation of a twin layer of Co [73]. Assuming this layer-by-layer like growth, the maximum mean film thickness d_{Co} received during a CV cycle can be calculated from Q_A taking into account that one atomic Co layer corresponds to a charge of $0.59\,\mathrm{mC/cm^2}$ [35]. With the size of the deposition area that is uncovered on the Au(111) substrate, which was determined to be $(5.3 \pm 0.3)\,\mathrm{mm^2}$ by images recorded with an optical microscope, a mean film thickness of $d_{Co} = 35.6^{+4.9}_{-3.1}$ atomic layers is obtained for the present measurement. This thickness is well above the limit of about 8 atomic layers, above which the bulk magnetic moment of $1.72\,\mu_B$ can be expected [76]. Hence, the accordance of the value of $1.75^{+0.08}_{-0.13}\,\mu_B$ received by the measurements with this bulk value, confirm that reliable values of the magnetic moment per Co atom are achieved with the presented technique.

4.3.2 Thickness dependence of the magnetic moment of ultrathin Co films

The measurement results of the last section have shown that the presented in-situ electrodeposition approach is a reliable method to determine the absolute magnetic moment of ultrathin magnetic films. In this section, it is applied to study the thickness dependence of the magnetic moment of Co films.

To acquire Co films with different thicknesses, which can be assigned to a certain magnetic moment, cyclic voltammetry measurements were performed using various lower potential limits U_{low} between $-1030\,\mathrm{mV}$ and $-1180\,\mathrm{mV}$. In total, 38 cycles were performed with the same electrochemical cell, starting with $U_{low} = -1030\,\mathrm{mV}$ and decreasing U_{low} stepwise for the further cycles. Exemplary, three CV cycles and the corresponding magnetic moment m_{film} of the deposited Co film measured during the electrodeposition are shown in Fig. 4.6 for the lower potential limits U_{low} of $-1045\,\mathrm{mV}$ (green solid line, full green circles), $-1140\,\mathrm{mV}$ (red dashed line, empty red squares) and $-1170\,\mathrm{mV}$ (blue dotted line, full blue triangles). The cyclic voltammograms as well as the magnetic moment m_{film} exhibit the same behavior as the one described in Section 4.3.1 (Fig. 4.3). Decreasing the potential U, the deposition starts to take place at $U = -1015\,\mathrm{mV}$ and m_{film} begins to rise from zero just together with the onset of the deposition. Towards the lower potential limit U_{low}, the absolute value of

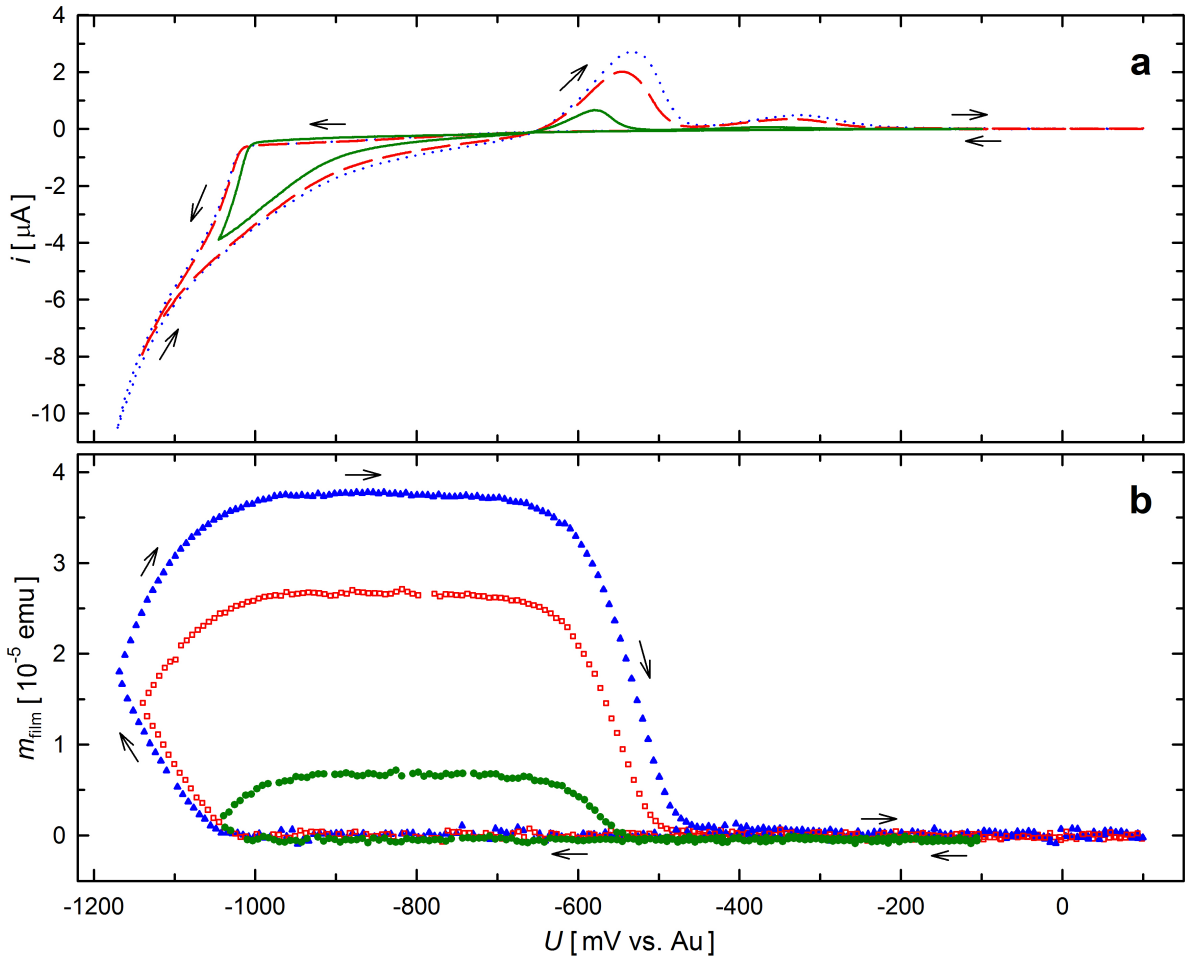

Figure 4.6: (a) Cyclic voltammograms of electrodeposition and subsequent dissolution of Co film on a Au(111) substrate measured with the in-situ electrochemical cell (electrolyte: 0.2 M $CoCl_2$ dissolved in ethanol, scan rate: 0.5 mV/s) and (b) corresponding magnetic moment m_{film} of the deposited Co film measured during the electrodeposition for different lower potential limits U_{low}. $U_{low} = -1045$ mV (green solid line and full green circles), $U_{low} = -1140$ mV (red dashed line and empty red squares), $U_{low} = -1170$ mV (blue dotted line and full blue triangles). The arrows show the direction of the potential sweep.

the current increases, signifying an increasing deposition rate. By lowering U_{low}, the Co deposition is prolonged and higher deposition rates are received and, therefore, thicker Co films are achieved. In consequence, the anodic dissolution peak increases and gets broader for the cycles with a more negative lower potential limit U_{low}. The higher deposition rates received for the cycles with a more negative lower potential limit U_{low} are clearly visible by the faster rise of m_{film} in vicinity of U_{low}. The increase of the thickness of the deposited films with decreasing U_{low} becomes apparent by the higher maximum values of m_{film}, which are reached after the end of the deposition in the potential region between about -950 mV and -670 mV. Regarding the decrease of m_{film} with Co dissolution, the broadening of the dissolution peak (see Fig. 4.6a), leads to a shift of the decline of m_{film} to higher potentials

Table 4.1: Charge Q_A of the anodic dissolution peak, maximum mean film thickness d_{Co} during a CV cycle (in atomic layers, a.l.), maximum number N_{Co} of deposited Co atoms during a CV cycle and maximum of the measured magnetic moment m_{film}, which occurs in the potential region between −950 mV and −660 mV. The data are given for the three CV cycles with different lower potential limits U_{low} shown in Fig. 4.6 and correspond to Fig. 4.7a (cell 1).

U_{low} [mV]	Q_A [mC]	d_{Co} [a.l.]	N_{Co}[10^{15} atoms]	m_{film} [10^{-5} emu]
−1045	$0.122^{+0.015}_{-0.012}$	$3.9^{+0.5}_{-0.4}$	$0.38^{+0.05}_{-0.04}$	0.67±0.02
−1140	$0.49^{+0.05}_{-0.02}$	$15.8^{+1.8}_{-1.0}$	$1.53^{+0.15}_{-0.05}$	2.67±0.03
−1170	$0.71^{+0.06}_{-0.03}$	$22.8^{+2.4}_{-1.5}$	$2.22^{+0.19}_{-0.08}$	3.75±0.03

(see Fig. 4.6b). All in all, the variations in the CVs with changing U_{low} in Fig. 4.6a correlate perfectly with the alterations of the progression of m_{film} in Fig. 4.6b.

To obtain values of the magnetic moment m_{atom} per Co atom as a function of the film thickness, the maximum mean thickness d_{Co} of the deposited Co film during a CV cycle is calculated from the charge Q_A of the anodic dissolution peak. The determination of Q_A was performed analogously as described on page 32, applying 14 baseline extrapolations per CV cycle. Since the form of the anodic dissolution peak varies just slightly from step to step with the stepwise variation of U_{low}, care was taken that the baseline progression applied to the different CV cycles (this means for the different U_{low} values) does not vary significantly from step to step. However, this also means that if the baseline current is under-/overestimated, this deviation will be the same for all CV cycles performed with the same electrochemical cell. The obtained values of Q_A for the three CV cycles shown in Fig. 4.6a are listed in Table 4.1. Further, the maximum mean Co film thickness d_{Co} during the CV cycle, the maximum number N_{Co} of deposited Co atoms and the maximum of the magnetic moment m_{film} measured during the CV cycle are given in this table. The calculation of these quantities from Q_A was done analogously as described in Section 4.3.1. Dividing these values of m_{film} by N_{Co} gives the magnetic moment per deposited Co atom m_{atom}.

Fig. 4.7a shows m_{atom} as a function of the mean film thickness d_{Co} for the three CV cycles of Fig. 4.6 and for 35 additional cycles which were performed with the same electrochemical cell using various values of U_{low} between −1030 mV and −1180 mV. From this plot, a distinct enhancement of the magnetic moment m_{atom} per Co atom becomes obvious for the first few atomic layers. m_{atom} increases steadily with reducing the film thickness d_{Co} for ultrathin films and amounts up to $2.6^{+0.5}_{-0.4}\,\mu_B$ for $d_{Co} = 1.07^{+0.22}_{-0.18}$ atomic layers. For thicker films, m_{atom}

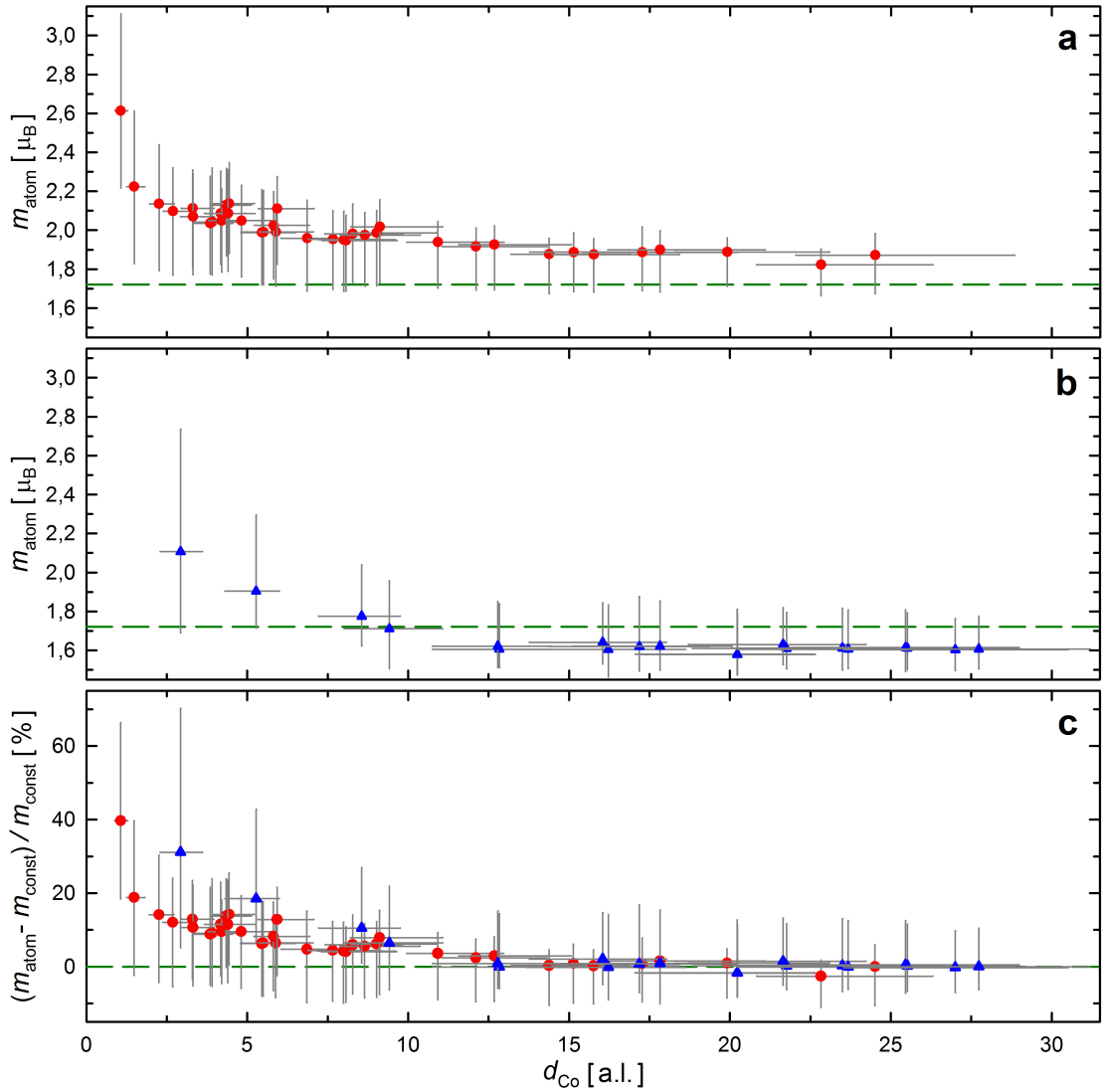

Figure 4.7: Magnetic moment m_{atom} per Co atom of electrodeposited Co films as a function of the mean film thickness d_{Co} (in atomic layers, a.l.), as obtained for electrochemical cell 1 (a) and cell 2 (b). (c) Relative enhancement $(m_{atom} - m_{const})/m_{const}$ of the magnetic moment m_{atom} with respect to the constant magnetic moment m_{const} reached for thicker films. In (a) and (b) the dashed green line indicates the Co bulk magnetic moment of $1.72\,\mu_B$ [74]. In (c) this line corresponds to a relative enhancement of 0 %. The error bars shown reflect the error of the charge determination together with the error in the determination of the windowed area of the Au(111) substrate and, the noise of m_{film} in the plateau regime corresponding to the maximum film thickness.

reaches a constant value, which agrees within the error bars with the Co bulk magnetic moment of $1.72\,\mu_B$ for hcp Co [74].

Fig. 4.7b shows an analogous plot, which was obtained by repeating the measurements with a second electrochemical cell. Since U_{low} was varied in larger steps for this cell, this plot contains fewer data points. As for the first cell, m_{atom} is clearly enhanced for films with a few atomic layer thickness, showing a continuous rise of m_{atom} with lowering d_{Co}. A

constant value of m_{atom} is attained for thicker Co films, which also coincides with the bulk value within the error limits.

As can be seen from Fig. 4.7a and b, the magnetic moment converges to the bulk value for thicker films within the error bars, but the mean values of m_{atom} (indicated by the symbols in Fig. 4.7) deviate slightly from it. Since the error of m_{atom} mainly originates from the uncertainty in the charge determination, this variation is considered to arise from slightly over-/underestimating on average the baseline current used for the determination of Q_A. As stated above, the over/underestimation is the same for all data points of a distinct electrochemical cell, because the average baseline form applied to the CVs with different U_{low} values (this means different d_{Co}) recorded with the same cell did not vary significantly. Hence, the relative enhancement $(m_{atom} - m_{const})/m_{const}$ of the magnetic moment in comparison to the magnetic moment m_{const} obtained for the thickest film is unaffected by this uncertainty in the determination of Q_A. Fig. 4.7c shows this relative enhancement as a function of the mean film thickness d_{Co}. The data of the two different cells coincide in this plot, showing an enhancement of the magnetic moment for films with d_{Co} smaller than about 10 atomic layers, which reaches an excess of 40 % for d_{Co} of one atomic layer.

4.4 Discussion

The results presented in Section 4.3 demonstrate that the absolute magnetic moment of ultrathin magnetic films can be measured reliably with a commercial SQUID magnetometer aplying the presented in-situ electrodeposition approach. Varying the film thickness d_{Co}, an enhancement of the magnetic moment of Co of up to 40 % could be observed. In this section this enhancement is compared with values reported in literature.

The appearance of an enhancement of the magnetic moment of the first few layers of Co thin films is well documented in literature by means of theoretical as well as experimental investigations[1]. For example, first principle calculations predicted an increase of the spin magnetic moment for a free-standing Co monolayer, which was attributed to a reduction of the number of valence electrons in the minority spin band [77]. Later calculations have shown that the orbital magnetic moment is also enhanced for a free-standing Co monolayer [78, 79]. Hjortsam et al. [78], who predicted an enhancement of the orbital moment by a

[1] For an extended literature review, see Chapter 5.6 of the review paper by Vaz et al. [65].

factor 2, argued that this increase can be caused by the lowered symmetry at the surface, larger values of the density of states at the Fermi level, band filling effects and the enhanced spin moment. The enhancement of the spin moment was attributed to band narrowing effects.

Enhanced spin and orbital moments were also predicted by first principle calculations for Co thin films on non-magnetic substrates (see e.g. [78, 80, 81]). Hjortstam et al. [78] calculated the spin and orbital magnetic moment for Cu(001) covered by a Co monolayer and Shick et al. [80] for Cu(001) covered by up to 3 Co layers, showing that the enhancement is most pronounced in the first layer. Šipr et al. [81] theoretically determined the spin as well as the orbital magnetic moment of Co monolayers on different substrates and they revealed, for instance, that both are higher for Au substrates in comparison to Cu substrates.

Furthermore, an enhanced magnetic moment was also measured by ex-situ techniques for uncapped (see e.g. [76, 82, 83]) and capped Co thin films (see e.g. [84–86]). With XMCD measurements, Tischer et al. [82] could show that the orbital magnetic moment of ultrathin Co films increases continuously relative to the spin magnetic moment, with lowering the film thickness down to two atomic layers. As possible explanations for the increase of the orbital moment, again the lowering of the symmetry at the surface, an increased value of the density of states at the Fermi level and the enhanced spin moment were given. By using XMCD sum rules, Srivastava et al. [83] could determine the spin and orbital contributions to the total magnetic moment of 2.1 Co atomic layers on Cu(001), and thus provided the experimental proof that both the spin and the orbital magnetic moment are enhanced. Ney et al. [76] used a custom-built UHV high-T_c SQUID magnetometer to measure the absolute magnetic moment of Co films on Cu(001) as a function of the film thickness and determined a continuous increase of the magnetic moment with decreasing the film thickness. By growing an additional Cu layer on top of the Co, the same group could separate the influence of the surface and interface and revealed that the increase of the moment at the surface is partially counterbalanced by a reduction of the magnetic moment at the Co/Cu interface [86].

In Fig. 4.8, the relative enhancement of the magnetic moment measured by the in-situ electrodeposition approach is shown as a function of the inverse film thickness $1/d_{Co}$ compared with the experimental values of the total magnetic moment of uncapped Co thin films, which were obtained by Srivastava et al. [83] and by Ney et al. [76]. In general, the data compare well to each other and coincide within error bars (not shown in Fig. 4.8). A linear increase of $(m_{atom} - m_{const})/m_{const}$ with respect to $1/d_{Co}$ is observed, in accordance with Ney et

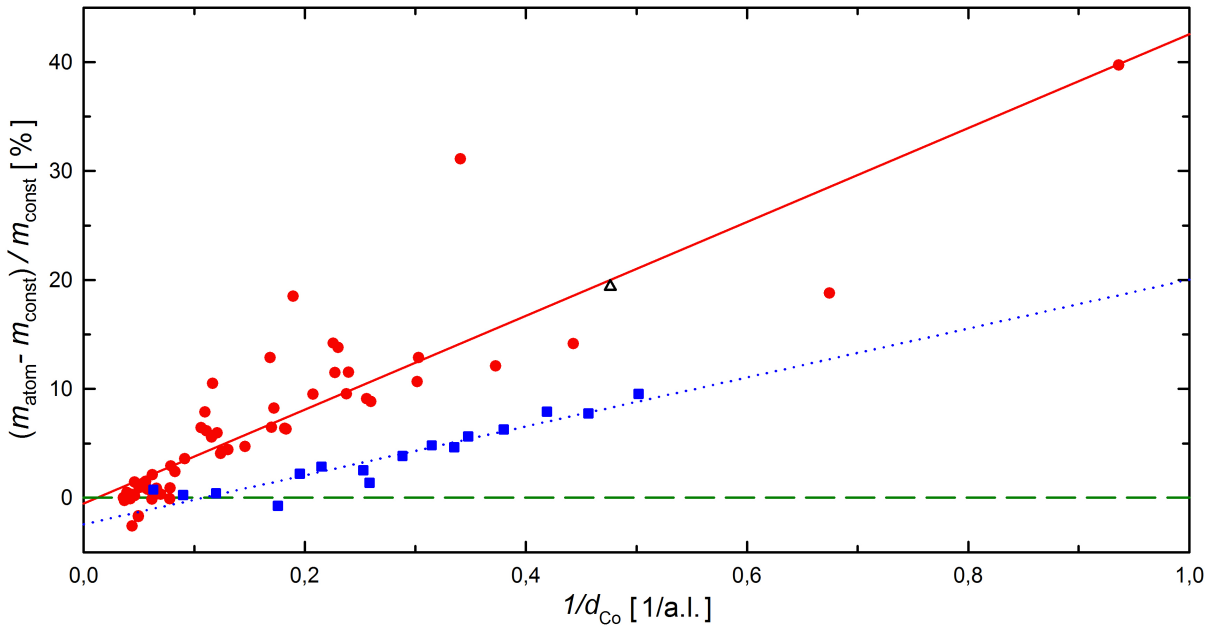

Figure 4.8: Relative enhancement of the magnetic moment m_{atom} of Co films (per Co atom) in comparison to the converging magnetic moment obtained for thicker films (m_{const}) as a function of the inverse film thickness $1/d_{Co}$ (in atomic layers, a.l.). The data obtained in this work by in-situ electrodeposition in a SQUID magnetometer (red circles) are compared with experimental values from literature, by Srivastava et al. [83] (empty black triangle) and by Ney et al. [76] (blue squares). The plotted relative enhancement of the literature values refers to the respective bulk value obtained in the quoted work. The red full and the blue dotted line are linear fits to own data and the data of Ney et al., respectively. For clarity error bars are omitted.

al. [76]. The greater enhancement and the stronger thickness dependence, as indicated by the higher slope of the regression line, in the present studies is attributed to a higher magnetic moment at the Co/Au(111) interface (present studies) compared to the Co/Cu interface (Ref. [76]). This conclusion is based on the following: (i) An observed reduction of the magnetic moment in the case of the Cu substrate could be caused by the formation of a Cu-Co alloy at the interface [86]. For the Co/Au(111) system intermixing does not occur at the Co/Au interface [87, 88], thus the formation of an alloy causing a reduced magnetic moment can be excluded for Co/Au(111). (ii) Furthermore, as already mentioned above, the ab initio electronic structure calculations by Šipr et al. predict a higher magnetic moment of a Co monolayer on Au substrates than on Cu substrates [81]. (iii) Moreover, as shown by XMCD measurements [89], a magnetic moment of up to $0.062\,\mu_B$ is induced per Au interface atom at the Co/Au interface through polarization, which leads to a further increase of the interface magnetic moment.

In addition to the influence of the different types of Co/substrate interfaces, the observation of an enhanced magnetic moment in our measurements in comparison with the measure-

ments at Co/Cu(001) (Ref. [76]) might also be caused – at least partly – by a higher surface magnetic moment compared to the one obtained by the measurements of Ney et al. (Ref. [76]). The emergence of a distinct surface magnetic moment is not surprising, since the measurements of Ney et al. were performed under UHV conditions, whereas in our studies the surface layer is in contact with an electrolyte. As recently shown in several publications (see e.g. [22]) and as demonstrated in Chapter 5 of this thesis, the interaction between an electrolyte and a magnetic material having a high surface fraction (like thin films or nanoporous materials) influences the magnetic properties of the material.

Finally, it should be mentioned that our data show a continuous enhancement of the magnetic moment with decreasing the average film thickness down to $d_{av} = 1$ atomic layer at $T = 300\,\mathrm{K}$, whereas a decrease of the magnetic moment was observed for ultrathin Co films on Cu(001) at 300 K [76][m]. For Cu(001), the reduction is attributed to a reduced Curie temperature T_C, which drops from about 330 K to about 20 K when decreasing the film thickness from 2 atomic layers to 1 atomic layer for the Co/Cu(001) system (see e.g. [90]). However, for Co/Au(111) the occurrence of superparamagnetic behavior at room temperature (respectively 300 K) at submonolayer Co coverages is well documented in literature [91–93], indicating a Curie temperature above 300 K even at these low coverages. Therefore, the magnetic moment for Co/Au(111) in the monolayer regime is not reduced at 300 K in contrast to Co/Cu(001).

The occurrence of a Curie temperature above 300 K for the Co/Au(111) system at monolayer coverage, in contrast to Co/Cu(001), could have two causes: On the one hand, the strong reduction of T_C for Co/Cu(001) with reducing the film thickness is attributed to the intermixing of Co and Cu and the formation of a Co-Cu alloy [94], whereas, as already stated above, no intermixing occurs at 300 K for the Co/Au(111) system [87, 88]. On the other hand, the growth mechanism of the Co film differs for the two systems. As well documented in literature (see e.g. [91]) bilayer high Co islands are formed for Co/Au(111) at low coverages rather than a homogenous monolayer. For the Co/Cu(001) system, only a small fraction of bilayer islands occurs [94]. Due to the formation of bilayer high islands at small coverages, the mean film thickness d_{Co} of 1 atomic layer for Co/Au(111) corresponds to a state where half of the Au substrate is covered by a Co film of 2 atomic layers. For 2 atomic layers T_C lies above 300 K also for the Co/Cu(001) system [90]. Thus, the different growth mechanism of Co/Cu(001) and Co/Au(111) could be the cause for the different T_C

[m] Note: The data of Ney et al. [76] shown in Fig. 4.8 were obtained by extrapolation to $T = 0\,\mathrm{K}$ (see [76]).

values at low coverages.

4.5 Conclusion and outlook

In summary, an electrochemical cell for SQUID measurements on magnetic thin films during electrodeposition was presented. To enable measurements of the small absolute magnetic moment of thin films, a cell was designed, which minimizes the magnetic background signal of the cell. In combination with the data evaluation procedure, considering the residual cell contribution to the magnetization, a perfect elimination of the background signal, including that of the substrate, could be achieved. Thus, the presented measurement set-up allows an exact determination of the magnetic moment m_{film} which arises exclusively from the electrodeposited film. This was demonstrated using as example the Co electrodeposition on Au(111) by cyclic voltammetry. It was shown that the in-situ electrodeposition approach enables not only a continuous, repetitive and background-free monitoring of the magnetic moment of ultrathin Co films during film growth and subsequent dissolution, but also an easy adjustment and determination of the mean film thickness d_{Co}. Hence, the thickness-dependence of the magnetic moment of the deposited Co films could be studied for films with thicknesses ranging from one up to some tens of atomic layers. A distinct enhancement of the magnetic moment m_{atom} per Co atom was observed for the first few atomic layers, with a continuous rise of m_{atom} with lowering d_{Co}. The appearance of such an enhanced magnetic moment for ultrathin Co films is in line with theoretical and ex-situ experimental data in literature. Consequently, the presented in-situ electrodeposition in combination with SQUID magnetometry represents a promising new method for the determination of absolute magnetic moments of ultrathin magnetic films.

In future experiments, it would be interesting to apply the presented in-situ electrodeposition approach to perform the same measurements for other magnetic materials, for instance Fe and Ni. Moreover, the measurements could be extended by performing field-dependent hysteresis measurements. However, even if the presented approach enables a total elimination of the magnetic background signal, hysteresis measurements for ultrathin films will be difficult because of the small magnetic moments at low magnetic fields and especially in vicinity of the coercivity field.

Furthermore, the influence of the interface between the magnetic thin film and the substrate could be studied by performing the electrodeposition on different substrates. Another

possibility to study interface effects is the electrodeposition of multilayer structures from single electrolytic baths, like Co/Cu [10, 11] or Fe/Pt [12]. Further possible applications of the present in-situ technique are in the fields of electrodeposition of magnetic nanoparticles [95, 96] and of template assisted electrodeposition of magnetic nanowires [13, 14], where modified magnetic moments due to the high surface-to-volume ratio are of high relevance.

CHAPTER 5

Electrochemical tuning of magnetic properties

5.1 Introduction

Besides many other applications of magnetic materials in everyday life, one of the technologically most important applications is in the field of data-storage devices, such as magnetic hard disk drives and magnetic random access memories (MRAMs)[n]. In the last few decades, the emergence of various spintronic devices, which utilize both the electrical charge and the spin of electrons to create new functionality, led to significant improvements in this area. For instance, the giant magnetoresistance (GMR) [97,98] and the tunnel magnetoresistance (TMR) [99–103] effects, which correspond to a large variation of the electrical resistance when the relative orientation of one towards another ferromagnetic layer in spin valves or magnetic tunnel junctions (MTJs) is changed, find application in read heads of magnetic hard disk drives. Furthermore, MTJs are used as memory elements in MRAM devices.

Whereas the read-out process in magnetic hard disk drives was advanced by the aforementioned developments, the writing of the information is still performed by the magnetic field produced by an electric current passing through the write head [104]. Also in the first MRAM generations, the magnetic bits were switched by magnetic fields induced by a current. The discovery of the spin-transfer torque (STT) effect [105–108], which enables the manipulation and switching of the magnetization of one of the ferromagnetic layers in the

[n] As mentioned in the introduction of this thesis (Chapter 1), parts of the content of this chapter are based on published articles (Paper I, Ref. [43] and Paper II, Ref. [44]).

spin valve or MTJ by a spin-polarized current, has led to the development of the so-called STT-MRAMs [109], where the writing can now be performed by passing a current directly through the MTJ instead of using it to generate the magnetic field. This new switching process enables a scaling down of the device area [110], but as for the generation of the magnetic field, large currents are required to generate the spin torque. Hence, both of these methods to manipulate the magnetization are quite energy consuming due to Joule heating and power consumption by the current flow. Thus, the development of more efficient methods of magnetization switching could lead to significant reductions of the device power consumption of these magnetic memory devices.

An energy effective way of switching is given by the manipulation of the magnetization purely by an electric field through an applied voltage rather than by currents. Since in this case of E-field switching, charge is only required for loading a capacitor, this method could reduce the energy dissipation by a factor of 100 compared to the switching by spin-polarized currents in STT-MRAM devices [111]. For this reason and because of the fundamental interest in the novel physics occurring in magnetic materials under E-field gating, the electric field manipulation of magnetism has attracted considerable attention over the last years[o].

One promising material class to achieve E-field control of magnetization are multiferroic materials, where the intrinsic coupling between ferroelectric and magnetic properties allows the tuning of the magnetization by applying an electric field [114, 115]. However, the rare occurrence in nature and difficult synthesis of multiferroics, as well as the fact that no single-phase ferromagnetic multiferroics exist at room temperature [116], limits their application in electronic devices. Alternatively, magnetic properties can be modified by the direct application of an electric field to the magnetic sample. This was first demonstrated for magnetic semiconductors, where the magnetism can be controlled by the E-field dependence of the charge carrier concentration [117,118]. However, because of the low Curie temperature T_C of magnetic semiconductors, which is below room temperature, this effect is again limited to low temperatures.

In contrast to magnetic semiconductors, metals can exhibit a high T_C. However, getting E-field control of their properties is quite difficult, since the electric field is screened by the conduction electrons within a few Ångstroms from the surface. Therefore, a high surface-

[o] For extended literature reviews on electric field controlled magnetism the reader is referred to the review papers by Matsukura et al. [111], Chiba and Ono [112] and Brovko et al. [113].

to-volume ratio as well as high electric fields are required to allow E-field penetration and by that to obtain E-field control of magnetism. Using the conventional approach, this was achieved within the last years by the using ultrathin films and a high-κ oxide thin film as solid dielectric (see e.g. [119–121]). Alternatively, as proposed by Gleiter et al. [40], the high electric field appearing in the electrochemical double layer between a metal electrode and a liquid electrolyte (see Sec. 2.1) can be used to tune the material properties reversibly. Beyond that, the electrochemical charging is not limited to the double layer regime, but can also induce electrochemical surface reactions (adsorption/desorption of ions from the solution, redox reactions), which can as well be used for tuning the material properties reversibly in case that the reactions are reversible. Since this method of electrochemical charging does not require a solid dielectric, it is perfectly suitable to achieve voltage control of material properties not only in ultrathin films, but also in porous nanophase materials, exhibiting a high surface-to-volume ratio. Besides for magnetic properties (see below), this approach of Gleiter et al. was successfully applied in recent years to tune the mechanical (see e.g. [122–128]), electrical (see e.g. [126, 129–134]), as well as optical (see e.g. [135]) properties of various materials.

The first reports on electrochemical tuning of magnetic properties using the concept of Gleiter et al. [40] were published about ten years ago. In these papers, it was reported that the magnetization of Pd-Ni [15], Pd [17] and Pd-Co [16] can be varied reversibly by charging in the electrochemical double layer regime. In 2007, Weisheit et al. [19] showed that also the magnetic coercivity H_C of FePt and FePd thin films can be tuned by this concept. An overview of these and following studies of electrochemical tuning of magnetism is given in Table 5.1. This table is restricted to publications monitoring directly magnetic property variations during in-situ electrochemical charging in a liquid electrolyte. The table does not include studies which monitor magnetic property variations more indirectly, e.g by deducing T_C variations from pure electrical measurements (see e.g. [136,137]), in-situ studies where magnetism is altered by redox reactions induced by ion migration from a solid gate oxide [138, 139], as well as ex-situ studies which characterize the magnetic properties before and after an electrochemical induced chemical reaction (see e.g. [140–143]). For the sake of completeness, it is noted that in-situ electrochemical charging in a SQUID magnetometer was also applied to probe E-field-induced superconductivity [144, 145].

Table 5.1: Summary of literature on in-situ measurements of magnetic properties during electrochemical charging. The publications are listed chronologically. N, Rev and E-Chem indicate the number of electrodes used for the in-situ charging, the reversibility of the observed effect and if the effect was mainly attributed to the electric field (E) or to chemical processes (Chem). The given relative variation is always the maximum value achieved in the quoted work. A positive/negative sign of the variation indicates that the given property increases/decreases with positive charging. The works enclosed in this thesis are in bold face.

First author	Material	Electrolyte	Measurement	N	Property[A]	Rev	E-Chem
Lemier (2005) [15]	Pd-Ni[B]	1 M $LiClO_4$	Extraction magnetometer	2	M(300 K): up to 1.3 %[C]	yes	E
Drings (2006) [17]	Pd[B]	1 M KOH[D]	Extraction magnetometer	2	χ(300 K): +1 %	yes	E
Ghosh (2006) [16]	Pd-Co[B]	1 M $LiClO_4$	Extraction magnetometer	2	M(300 K, 100 Oe): −3 %	yes	E
Weisheit (2007) [19]	FePt, FePd thin films	$C_4H_6O_3$ with Na^+OH^-	MOKE	2	H_C(RT): FePt+4.5 %, FePd −1 %	yes	E
Hiraoka (2009) [20]	Ni thin films	borate buffered solution (pH 9)	Faraday ellipticity	3	M_S(300 K): −15 % for 10 nm thick film	yes	Chem
Mishra (2010) [132]	Au_{55}-Fe_{45}[B]	1 M $LiClO_4$	Extraction magnetometer	2	M(275 K, 60 kOe): −0.2 %	yes	E
Zhernenkov (2010) [41]	$Co_{50}Pd_{50}$ thin film	$C_4H_6O_3$	PNR	3	M(RT, 3 kOe): −4.5 %	–	E
Ghosh (2011) [146]	Pd-Ni[B]	1 M $LiClO_4$	Extraction magnetometer	3	M(RT): up to 0.5 %[C]	yes	E
Traußnig (2011) [18]	γ-Fe_2O_3/Pt[B]	1 M KOH	SQUID magnetometer	2	M(300 K, 50 kOe): −10.4 %	yes	Chem
Yamada (2011) [147]	$Ti_{0.9}Co_{0.1}O_2$ thin film	Ionic liquid	Anomalous Hall effect	2	σ_{AH}(300 K): ferromagnetic behavior under gating	yes	E
Shimamura (2012) [148]	Co thin film	Ionic liquid	SQUID magnetometer	2	T_C varies by 100 K and leads to variations of M and H_C at 300 K	yes	E
Kawaguchi (2012) [149]	Fe thin film	Ionic liquid	SQUID magnetometer	2	M_S(10 K): +50 %	–	Chem
Leistner (2012) [21]	FePt thin film	1 M $LiPF_6$	Anomalous Hall effect	2	M_S: −10 %	yes[E]	Chem
Tournerie (2012) [22]	Co thin film	0.1 M K_2SO_4+1 mM KCl+1 mM H_2SO_4	MOKE	3	H_C(RT): −50 %, χ(RT): −55 %	yes	E
Topolovec (2013) [43]	**γ-Fe_2O_3/Pt[B]**	**1 M KOH**	**SQUID magnetometer**	**3**	**M(300 K, 5 kOe): −4.2 %**	**yes**	**Chem**
Mishra (2013) [150]	$La_{0.75}Sr_{0.25}MnO_3$[B]	0.5 M $LiClO_4$	Extraction magnetometer	3	M(350 K,1 kOe): +2.5 %[F]	yes	E
Leistner (2013) [23]	FePt thin film	0.1 M $LiClO_4$	Anomalous Hall effect	2	M_S: −2 %	yes	Chem
Reichel (2013) [151]	CoPt thin films	0.1 M $LiClO_4$	Anomalous Hall effect	2	M_S(290 K): −4 %, H_C(290 K): −212 %	no	Chem
Yamada (2013) [152]	Prussian blue analogues	1 M $LiPF_6$	SQUID magnetometer	2	M(2 K,10 kOe): −130 %, T_C +50 %	yes	Chem

Leistner (2013) [153]	FePt thin film	0.1-1 M $LiPF_6$[G]	Anomalous Hall effect	2	M_S: −4 %, K_{eff}: +25 %	yes	Chem
Steyskal (2013) [44]	**Pt[B]**	**1 M KOH**	**SQUID magnetometer**	**3**	**M(300 K, 5 kOe): −1 %**	**yes**	**E**
Ghosh (2013) [154]	$Pd_{67}Ni_{33}$[B]	1 M KOH	Extraction magnetometer	2	M(300 K, 1 kOe): 25 %[H]	yes	Chem
Shimizu (2013) [155]	Pt thin film	Ionic liquid	Anomalous Hall effect	2	ρ_{AH}: ferromagnetic behavior under gating	no	Chem
Herrera Diez (2014) [156]	FePt film	Ionic liquid	MOKE	2	H_C: −11 %	–	E
Dasgupta (2014) [157]	γ-Fe_2O_3[I]	1 M $LiPF_6$	Extraction magnetometer	2	M(300 K, 10 kOe): +27 %	yes	Chem
Gershinsky (2014) [158]	$FeSb_2$[I]	1 M $LiPF_6$	SQUID magnetometer	2	M(300 K, 20 kOe) increases stepwise with Li intercalation	no	Chem
Akiyama (2014) [159]	$Cr_{1-\delta}Te$ thin film	Ionic liquid	SQUID magnetometer	2	M(15 K, 20 kOe): 195 %, H_C(15 K): 50 %[J]	–	E
Yamada (2014) [160]	Fe_3O_4[I]	1 M $LiPF_6$	SQUID magnetometer	2	M(300 K, 1 kOe): +13 %	yes	Chem
Reitz (2014) [161]	LCMO thin film[M]	Ionic liquid	SQUID magnetometer	2	M(230 K, 0.5 kOe): +13 %	yes	E
Shimizu (2014) [162]	$SrRuO_3$ thin film	Ionic liquid	Anomalous Hall effect	2	ρ_{AH}(2 K): +40 %	–	E
Tournerie (2015) [33]	Co thin film[K]	0.1 M K_2SO_4+0.1 mM KCl+2 mM H_2SO_4[L]	MOKE	3	H_C(RT): −50 % for H-terminated film, +35 % for CO-terminated film	yes	E+Chem
Di (2015) [163]	Co thin film	1 mM KOH	MOKE	3	Complete spin reorientation with oxidation for d <4 nm	yes	Chem
Wang (2015) [164]	IrMn thin film on Co/Pt	Ionic liquid	Anomalous Hall effect	2	H_E(10 K): +250 %	yes	E
Topolovec (2015) [47]	**$LiCoO_2$[I]**	**1 M $LiPF_6$**	**SQUID magnetometer**	**3**	**χ(300 K): +167 %**	**yes[N]**	**Chem**

[A] The following abbreviations are used in this column: M... magnetic moment, χ... magnetic susceptibility, H_C... coercivity field, RT... room temperature, M_S... saturation magnetization, σ_{AH}... anomalous Hall conductivity, T_C... Curie temperature, K_{eff}... effective anisotropy constant, ρ_{AH}... anomalous Hall resistance, H_E... exchange bias field.

[B] Nanoparticles were compacted into a porous sample.

[C] The given value is the maximum value which can be read out of the quoted work. The actual value and its sign depend on the composition and the magnetic field.

[D] Alternatively, 1 M $LiClO_4$ was used as electrolyte.

[E] For the measurements between 2 and 3 V, where a variation of 8 % occurs.

[F] The actual value and its sign are not only dependent on the temperature and the applied magnetic field, but also on the surface to volume ratio of the sample.

[G] Alternatively, 0.1 M $LiClO_4$ was used as electrolyte.

[H] The sign changes during the potential scan and is positive or negative dependent on the potential.

[I] The given material was intermixed with carbon and a binder to form an electrode.

[J] M increases and H_C decreases at negative and positive voltages.

[K] The Co thin films were either covered by a monolayer of H or CO.

[L] Alternatively, different supporting electrolytes where the main cation were Li^+, Na^+, K^+ and Cs^+ were used.

[M] $La_{0.68}Ca_{0.30}Mn_{1.02}O_{3-\delta}$

[N] Smaller parts of the observed variation of χ are irreversible.

As Table 5.1 shows, different measurement techniques were applied to monitor the magnetic properties during electrochemical charging. Whereas MOKE and anomalous Hall effect (AHE) measurements were applied for most of the studies on thin films, SQUID and extraction magnetometers were most often used for studies on porous nanophase samples. These direct magnetometry techniques have the advantage that absolute values of the magnetic moment are obtained, whereby SQUID is distinguished by its high sensitivity. Furthermore, the experimental set-ups differ in respect to the electrochemical measurements. Most of the in-situ measurements were performed with electrochemical cells containing only two electrodes and the magnetic properties of the investigated sample were monitored stepwise at certain potentials. As already stated in Chapter 3, a three-electrode set-up is necessary for reliable in-situ cyclic voltammetry measurements. Only by means of the three-electrode set-up, the variations of the magnetic properties can be directly related to the different electrochemical reactions (double layer charging, adsorption/desorption, redox reaction) and the magnetic properties can be monitored continuously during the potential scan.

For these reasons, the aim of this work was to design a three-electrode electrochemical cell for operation in a SQUID magnetometer, enabling in-situ cyclic voltammetry measurements. This new cell design is applied to examine the tunability of the magnetic moment of γ-Fe_2O_3 nanoparticles[p]. In a previous study performed in two-electrode geometry [18], we could show that the magnetic moment of these γ-Fe_2O_3 nanoparticles can be varied reversibly up to several percent upon electrochemical charging. In the study reported here, the three-electrode cell is used to derive more detailed information on the correlation between the electrochemical processes and the magnetic behavior.

Furthermore, the tunability of the magnetic moment of porous nanophase Pt upon electrochemical oxidation is investigated with this new cell and compared with variations of the electrical resistance[q]. Pt is chosen as model system for this direct comparison of electrical resistance and magnetic moment variations, since the electrochemical reactions occurring on Pt during charging are well documented in literature. Monitoring these two different electronic properties during electrochemical charging represents an ideal combination to better understand the underlying charging-related processes since both properties are expected to respond differently on double layer charging and chemical modification.

[p] This study on the tunability of the magnetic moment of γ-Fe_2O_3 nanoparticles was published in [43] (Paper I).

[q] This study on the tunability of the magnetic moment and electrical resistance of porous nanophase Pt was published in [44] (Paper II). The measurements of the electrical resistance were performed by Eva-Maria Steyskal.

The remainder of this chapter is structured as follows: First, the cell design and other experimental details, as well as results of pre-characterization measurements on the investigated materials are described in Section 5.2. Then, the results of the tunability of the magnetic moment are presented for Pt in Section 5.3.1 and for γ-Fe_2O_3 in Section 5.3.2, followed by a discussion in Section 5.4. Finally, a conclusion and outlook is given in Section 5.5.

5.2 Experimental and pre-characterization

In this experimental part, first the preparation and pre-characterization of the porous nanophase electrodes, which were investigated with respect to the tunability of their magnetic moment, are described in Section 5.2.1. Then, the design of the electrochemical cells used for the in-situ measurements in the SQUID is presented in Section 5.2.2. Finally, the experimental procedures used is described in Section 5.2.3.

5.2.1 Preparation and pre-characterization of porous nanophase electrodes

The porous nanophase electrodes investigated with respect to tunable magnetic moment were prepared from the following starting materials, which were either provided by cooperation partners or commercially available:

- γ-Fe_2O_3 nanopowder: The γ-Fe_2O_3 (maghemite) nanopowder was synthesized by Dorothée Vinga Szabó at the Karlsruhe Institute of Technology by means of the microwave plasma synthesis method. $Fe(CO)_5$ was used as precursor material and a mixture of 80 % Ar and 20 % O_2 as reaction gas. Further details on the preparation method can be found in [165–167]. As shown by transmission electron microscopy, the typical particle size of the γ-Fe_2O_3 nanoparticles obtained by this method is 4-6 nm [168, 169] and hysteresis measurements revealed that the particles show superparamagnetic behavior at 300 K [169].

- Pt nanopowder: A commercially available Pt nanopowder was purchased ("Platinum Black", Chempur GmbH, Karlsruhe, Germany). According to the manufacturer, this powder has a specific surface area of 20-40 m^2/g. An X-ray diffraction pattern of this powder can be seen in Fig. 5.1 which was recorded using a Bruker D8 Advance powder diffractometer with CuK_α radiation in Bragg-Brentano geometry. Using the Scherrer formula [170], a crystallite size of 7 ± 1 nm was determined from the width of the peaks. Field-dependent SQUID measurements at 300 K have shown that this powder

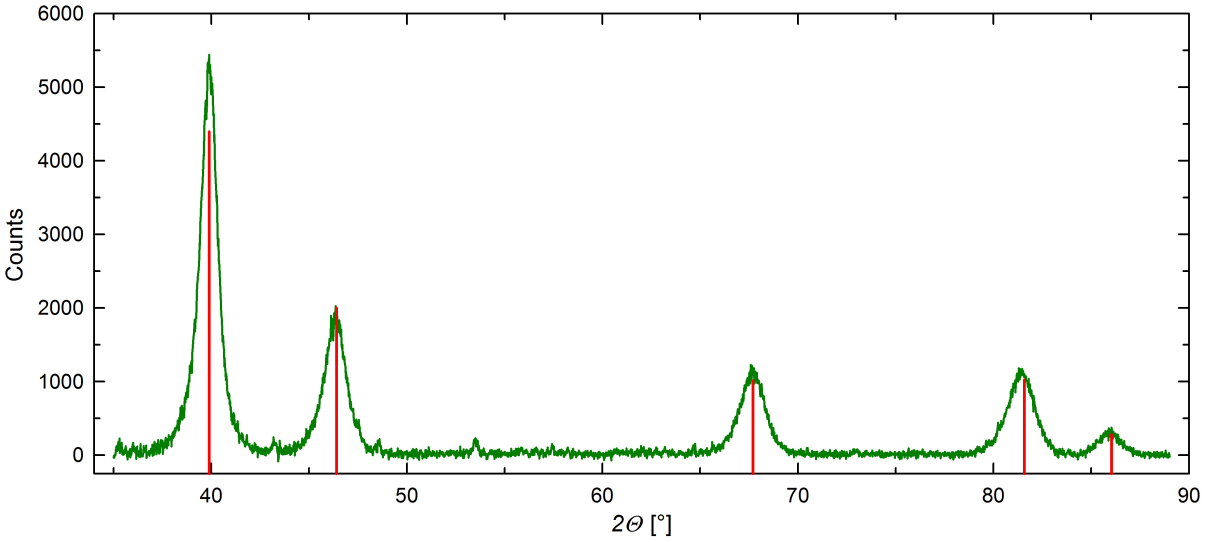

Figure 5.1: X-ray diffraction pattern of Pt nanopowder used for the preparation of the porous nanophase electrodes. The vertical, red lines represent the positions and relative peak intensities of Pt according to the reference database [172].

exhibits paramagnetic behavior [171].

To enable charging of the insulating γ-Fe_2O_3 nanoparticles, a nanocomposite of the oxide and of Pt nanoparticles was formed, based on the concept that the surface of the γ-Fe_2O_3 nanoparticles can be charged at the γ-Fe_2O_3-Pt-electrolyte interface by means of the conductive network made out of the Pt particles. Therefore, the γ-Fe_2O_3 nanopowder was ultrasonically intermixed with the Pt nanopowder in a nominal weight ratio of 1:10. To obtain a porous γ-Fe_2O_3/Pt nanocomposite for the SQUID measurements, the intermixed powder was filled in a pellet die (see Fig. 5.2a). After pre-compaction by hand, the filled die was mounted in a bench vise, where the final compaction was carried out manually. That way, cylindrical pellets with a diameter of 3 mm and a height of about 0.5 mm were obtained. In the same manner, a porous Pt electrode is made from the Pt nanopowder. The weight was 14.5 mg for the γ-Fe_2O_3/Pt nanocomposite pellet and 17.8 mg for the Pt pellet (further referred to as sample Pt_{SQUID}). Finally, the pellets were carefully wrapped by a Au wire (diameter: 0.1 mm, purity: 99.9 %) for electrical contacting (see Fig. 5.2b).

For the measurements of the electrical resistance, 104 mg of the Pt nanopowder were compacted into a PTFE groove (further referred to as sample Pt_{ER}). Similar to previous work in our research group [129], Pt wires (Ø=0.2 mm, 99.9%, ChemPur, Karlsruhe, Germany) were embedded in the groove as electrical contacts, and improved by adding a fifth wire providing an independent contact for electrochemical charging.

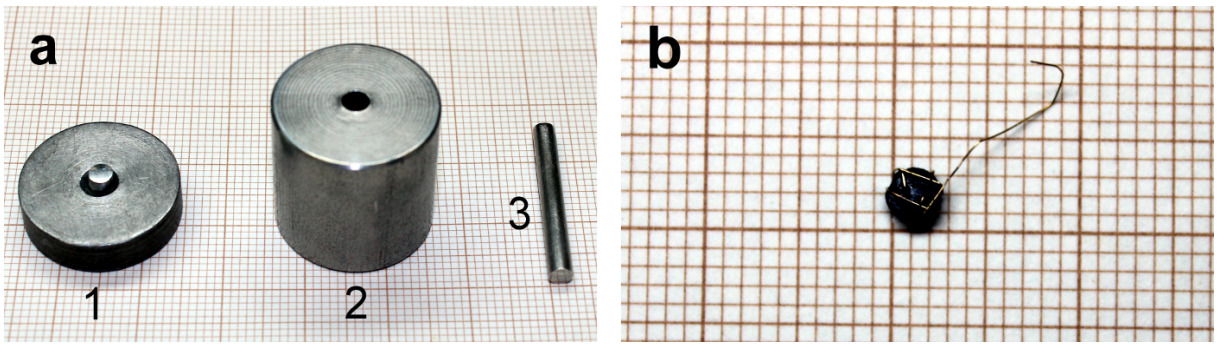

Figure 5.2: Photographs of (a) pellet die used for the preparation of the porous nanophase electrodes and of (b) porous Pt pellet produced therewith, wrapped by a gold wire for electric contact. Part (a) shows the base anvil (1), the die body (2) and the top anvil (3). The photographs were taken with millimeter-scale paper in the background.

To confirm the porosity of the Pt samples, their electrochemical active surface area was determined by cyclic voltammetry measurements in the hydrogen adsorption/desorption regime (for details on this method see [173]). The surface area of the samples was determined from the charge under the H desorption peaks in the cyclic voltammogram (see potential region between $-1000\,\mathrm{mV}$ and $-560\,\mathrm{mV}$ in anodic scan direction in Fig. 3.1b), taking into account that the adsorption/desorption of one monolayer of H on Pt corresponds to a charge of $210\,\mu\mathrm{C/cm^2}$ [173]. That way, specific surface areas of $6\,\mathrm{m^2/g}$ for the $\mathrm{Pt_{SQUID}}$ and $5\,\mathrm{m^2/g}$ for the $\mathrm{Pt_{ER}}$ sample were obtained. These high values of the specific surface area indicate the existence of a porous structure for these samples. Since the currents arising from the Pt and γ-$\mathrm{Fe_2O_3}$ are superimposed in the CV of the γ-$\mathrm{Fe_2O_3}$/Pt nanocomposite (see Fig. 5.10b), the electrochemical active surface area of this sample cannot be determined by the same method. However, the relative high currents in the CV suggest the existence of a high surface area as well.

To analyze the structure and composition of the γ-$\mathrm{Fe_2O_3}$/Pt nanocomposite pellet, and thereby also confirm the porosity of this sample, Scanning Electron Microscopy (SEM) and Energy-Dispersive X-ray spectroscopy (EDX) measurements were conducted[r]. Fig. 5.3 shows four of the recorded electron micrographs. From Fig. 5.3a it becomes obvious that the structure of the pellet is not homogeneous, but rather shows a lamellar-like structure consisting of elongated inclusions embedded in a matrix. In Fig. 5.3b, an image of the same area of the sample is shown, which was recorded with an energy-selective backscatter detector yielding a higher compositional contrast. This image reveals that the composition of the elongated inclusions and the surrounding matrix differ from each other. Indeed, EDX

[r] The SEM and EDX measurements were performed by Ilse Letofsky-Papst and Sanja Simic from the Institute of Electron Microscopy and Nanoanalysis at the Graz University of Technology.

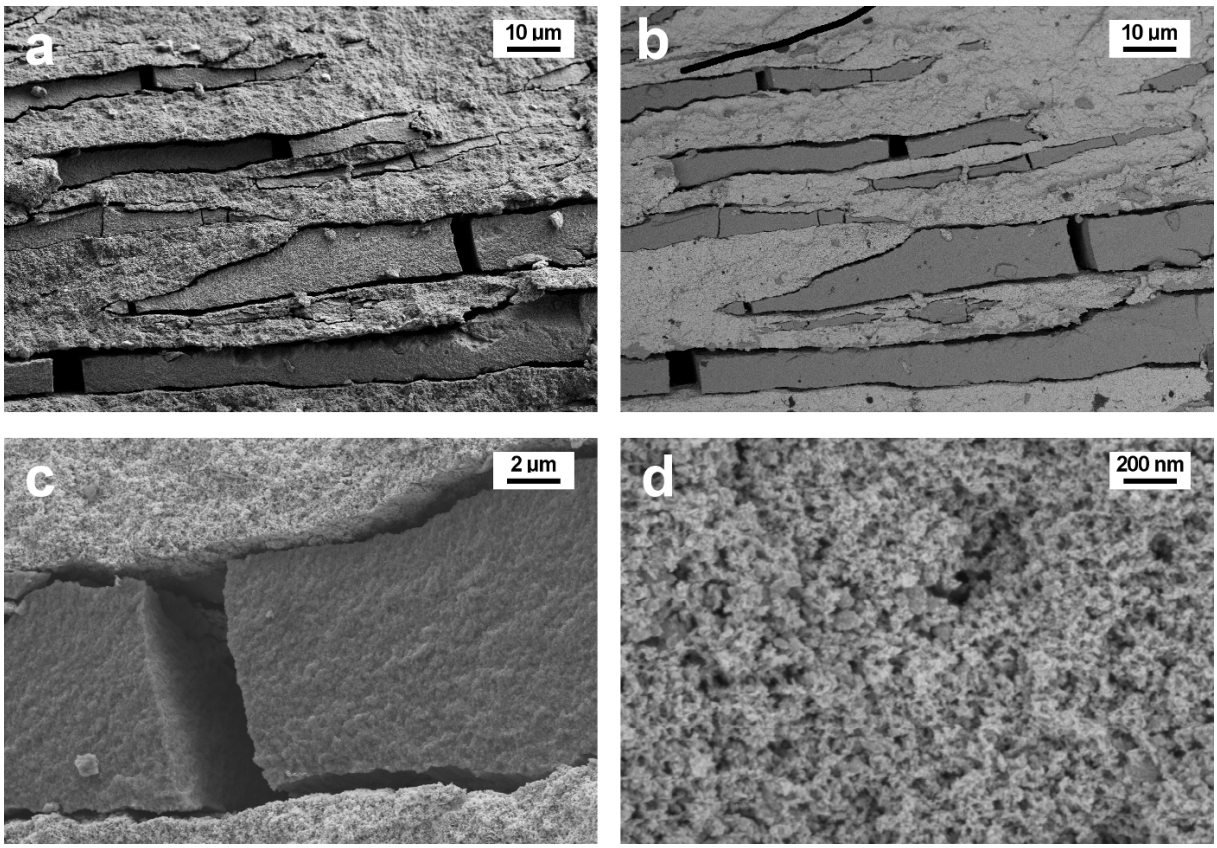

Figure 5.3: Scanning electron micrographs of γ-Fe_2O_3/Pt nanocomposite pellet recorded using secondary electron detector (a,c,d) and energy-selective backscatter detector (b). See text for further description.

spectra taken at the two different regions proved that the matrix phase contains 97.7 wt% of Pt, whereas only 12.3 wt% of Pt are present in the elongated inclusions. This suggests that the Pt and γ-Fe_2O_3 nanopowders were not mixed homogeneously prior to the compaction of the composite pellet. The elongated shape of the γ-Fe_2O_3 rich inclusions can be ascribed to the compaction process, where the pressure was applied in the vertical direction of the micrographs. Fig. 5.3c and d show SEM micrographs recorded at higher magnifications, where the porous structure of the γ-Fe_2O_3/Pt nanocomposite can be discerned.

5.2.2 Electrochemical cell design

To study the charging-induced variations of the magnetic moment m of the Pt_{SQUID} and the γ-Fe_2O_3/Pt nanocomposite sample, electrochemical cells were designed enabling charging of these porous nanophase electrodes by cyclic voltammetry during the measurement of m by the SQUID magnetometer. The cell design is based on the requirements listed in Section 3.3 and differs slightly for the Pt_{SQUID} and the γ-Fe_2O_3/Pt nanocomposite sample because of the various demands on the magnetic background signal of the cell. Whereas

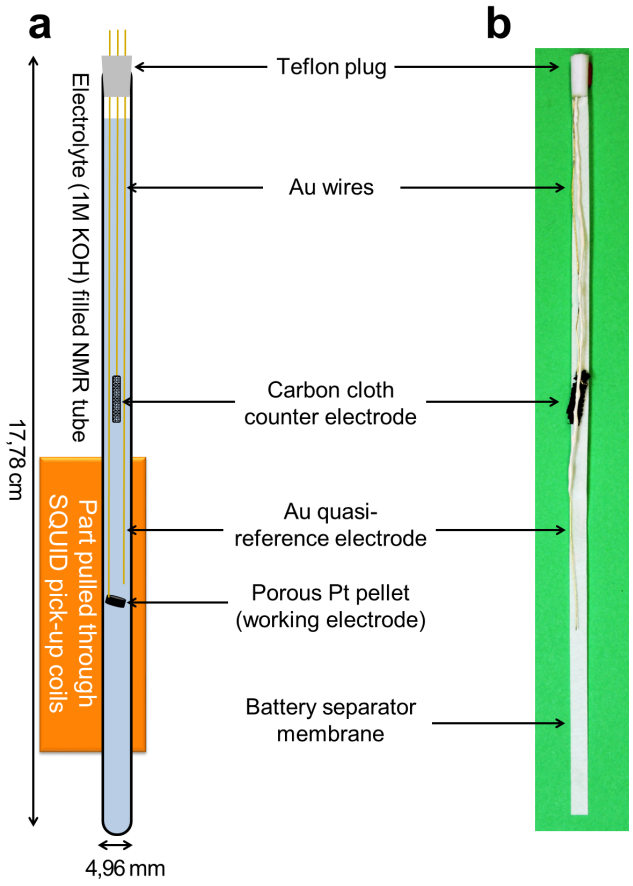

Figure 5.4: (a) Sketch and (b) photograph of electrochemical cell used for in-situ cyclic voltammetry measurements in SQUID magnetometer at Pt electrodes. The partial masking of the Au wire serving as quasi-reference electrode and the battery separator membrane are not shown in (a), but can be seen in (b). In (b) the porous Pt pellet is located behind the battery separator membrane, which extends over the entire lenght of the NMR tube. The orange area in (a) indicates the part of the cell which is pulled through the SQUID pick-up coils during a measurement scan over a length of 6 cm.

the pure Pt sample is a paramagnet and thus exhibits a relative small magnetic moment at moderate magnetic fields, the γ-Fe_2O_3/Pt nanocomposite sample has a relative high magnetic moment already at moderate fields. Thus, the magnetic background signal of the cell has to be reduced as far as possible for the Pt_{SQUID} sample by proper cell design. For the γ-Fe_2O_3/Pt nanocomposite sample, however, the usage of diamagnetic materials for the cell assembly alone is sufficient to reduce the magnetic background signal of the cell in such a way that measurements on the charging-induced variation of the magnetic moment of the γ-Fe_2O_3/Pt nanocomposite become possible.

A sketch of the electrochemical cell used for the measurements at the Pt_{SQUID} sample is presented in Fig. 5.4. As for the Co electrodeposition (see Sec. 4.2.1), a long borosilicate glass NMR tube (length 17.78 cm, diameter 4.96 mm, 505-PS-7, Wilmad-LabGlass,

Vineland, NJ, USA) is used as electrolyte compartment. The porous nanophase Pt pellet (sample Pt_{SQUID}), which is wrapped by a Au wire serves as working electrode. A high surface area carbon cloth, also contacted by a Au wire, and a Au wire are used as counter and quasi-reference electrode, respectively. The placement of the electrodes can be seen in Fig. 5.4. To avoid short circuits in the cell, the upper part of the Au wire acting as quasi-reference electrode is masked by an epoxy resin (Loctite 1C Hysol, Henkel) and a battery separator membrane (FS 2226, Freudenberg Vliesstoffe KG, Weinheim, Germany) is placed horizontally in the cell in-between the working and quasi-reference electrodes (see Fig. 5.4b). The whole cell is filled with 1 M KOH as electrolyte and closed with a PTFE plug, provided with three feedthroughs for the Au wires connecting the electrodes. Finally, the cell is sealed with epoxy resin (UHU plus endfest 300, UHU GmbH & Co KG, Bühl, Germany).

In Fig. 5.4a, the area of the cell is indicated, which is pulled through the magnetometer pick-up coils during a measurement scan of 6 cm. As can be seen from this sketch, the NMR tube extends well beyond the coils and the counter electrode is located outside the coils during the whole measurement scan. Thus, neither the electrolyte filled tube nor the counter electrode cause changes of the SQUID output voltage signal. Since the minor contributions of the thin Au wires to the magnetic signal can be neglected, the measured magnetic signal and, therefore, the magnetic moment m determined from it, arises exclusively from the Pt pellet.

The electrochemical cell used for the measurements at the γ-Fe_2O_3/Pt nanocomposite sample is sketched in Fig. 5.5. The γ-Fe_2O_3/Pt nanocomposite pellet serves as working electrode and is placed at the bottom of a cylindrical shaped PTFE compartment (outer diameter: approx. 5.5 mm, height: approx. 18 mm). The bottom zone of this compartment is electrically isolated from the upper zone by a battery separator membrane (FS 2226, Freudenberg Vliesstoffe KG, Weinheim, Germany). In the middle of the upper zone, a Au wire (diameter: 0.25 mm, purity: 99.9%), wrapped in a same battery separator membrane is positioned as quasi-reference electrode (QRE). As counter electrode serves a high surface area carbon cloth contacted with a Au wire (diameter: 0.25 mm, purity: 99.9%) which is positioned off-axis in the upper part of the compartment. In the end, the compartment is filled with 1 M KOH as aqueous electrolyte, closed with a PTFE plug and sealed with epoxy resin (UHU plus endfest 300, UHU GmbH & Co KG, Bühl, Germany).

With this cell design used for the measurements at the γ-Fe_2O_3/Pt nanocomposite sample,

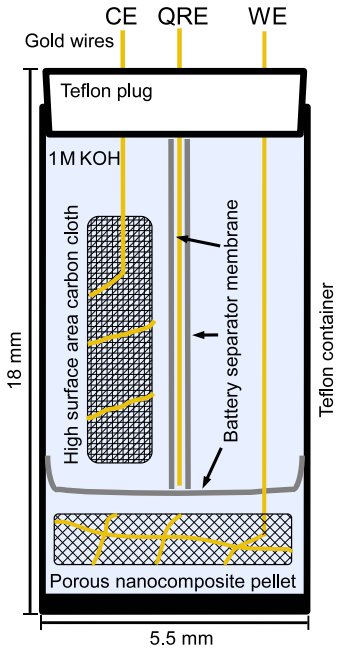

Figure 5.5: Sketch of electrochemical cell used for in-situ cyclic voltammetry measurements in SQUID magnetometer at γ-Fe_2O_3/Pt nanocomposite electrodes. WE, QRE and CE denote working, quasi-reference and counter electrode, respectively.

the magnetic SQUID signal of the γ-Fe_2O_3/Pt nanocomposite pellet is always superimposed by the magnetic signal of the cell. However, as demonstrated in Section 5.3.2, the signal of the cell is small in comparison to the signal of the γ-Fe_2O_3/Pt nanocomposite and, therefore, does not influence the measured variations of the magnetic moment of the γ-Fe_2O_3/Pt nanocomposite significantly.

5.2.3 Procedure for SQUID and resistance measurements

For the in-situ charging experiments in the SQUID magnetometer, the electrochemical cells described above were mounted into a standard plastic straw and attached to a modified sample rod with electrical feedthroughs, connecting the Au leads of the electrodes with a potentiostat placed next to the magnetometer. The measurements of the magnetic moment m were conducted using a scan length of 6 cm with 32 and 64 data points recorded in each scan for the Pt_{SQUID} and γ-Fe_2O_3/Pt nanocomposite sample, respectively. The measurements were performed at 300 K. If not otherwise stated, the applied magnetic field was 5 kOe.

The measurements of the electrical resistance variation were performed at ambient temperature in a standard electrochemical cell using a PGZ-100 potentiostat (Radiometer Analytical, Villeurbanne Cedex, France). In this set-up, the Pt_{ER} sample serves as working

electrode and is charged via the Pt wire contacted at the center of the sample. A high surface area carbon cloth and a commercial Ag/AgCl (saturated KCl) electrode (Radiometer Analytical, Villeurbanne Cedex, France) are used as counter and reference electrode, respectively. Like for the charging in the SQUID, 1 M KOH was used as aqueous electrolyte. The electrical resistance was measured in four-point geometry with a Keithley 2400 multimeter (Keithley Instruments Inc., Cleveland, OH, USA) using the outer contact pair for current supply and the inner contact pair for voltage measurement.

The charging of the porous nanophase electrodes during the SQUID and the electrical resistance measurements was performed by cyclic voltammetry. Unless otherwise stated, the scan rate v used for the cyclic voltammetry measurements was 0.5 mV/s. Such a small scan rate is necessary due to the porous structure of the samples, leading to a limited transport kinetics. Furthermore, this small scan rate enabled measurements of the magnetic moment in relative small potential steps. Prior to the measurements, the electrodes were activated by repeatedly cycling between the oxygen and hydrogen evolution regimes.

For a direct comparison of the behavior of the electrical resistance and the magnetic moment of the Pt samples, all potential values in Section 5.3.1 are given relative to the Ag/AgCl reference electrode, i.e., the data taken with the Au quasi-reference electrode are converted to corresponding values relative to the Ag/AgCl electrode. Since only SQUID measurements were performed for the γ-Fe_2O_3/Pt nanocomposite, all potential values in Section 5.3.2 are given with respect to the Au quasi-reference electrode. However, a comparison with measurements performed with a Ag/AgCl reference electrode is presented on page 64.

5.3 Results

5.3.1 Porous nanophase Pt

As stated above, the measurements on the porous nanophase Pt samples aim at a direct comparison of the tunability of the electrical resistance and the magnetic moment and, therefore, at getting a deeper understanding of the underlying charge-related processes since both properties are expected to respond differently on charging and chemical modifications. A particular emphasis was laid on how the electrical resistance R and the magnetic moment m of Pt vary with charging in the oxygen adsorption and desorption regime.

To display the investigated potential regime of oxygen adsorption and desorption, a typ-

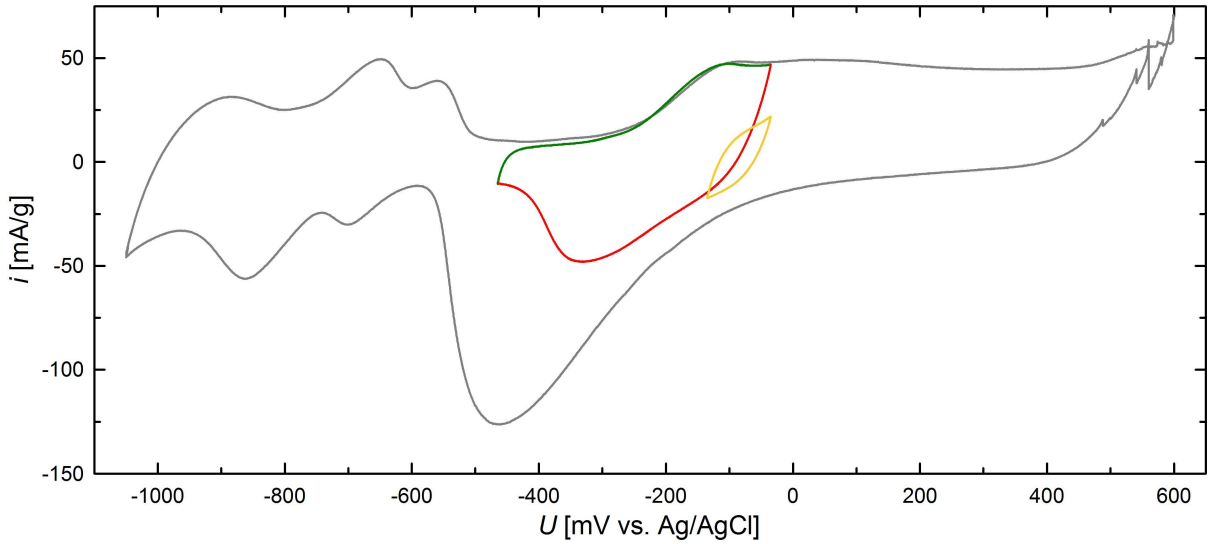

Figure 5.6: Cyclic voltammograms (CVs) of porous nanophase Pt (sample Pt_{ER}) measured in 1 M KOH at a scan rate of $v = 0.5$mV/s in different potential ranges from -1050 mV to $+600$ mV (gray), -465 mV to -35 mV (green, red) and-135 mV to -35 mV (yellow).

ical cyclic voltammogram taken for sample Pt_{ER} is shown by the gray curve in Fig. 5.6. This CV exhibits all the characteristic features of a Pt CV [59–61], which were already described in Section 3.1.1. In short, upon anodic scanning the peak system due to hydrogen desorption (-950 mV to -530 mV), the double layer region characterized by low charging currents (-500 mV to -300 mV), as well as the shoulder and plateau of oxygen adsorption/sample oxidation (-250 mV to $+600$ mV) followed finally by O_2 gas evolution can be discerned. In opposite direction, oxygen remains on the surface until the desorption peak is reached (extremum at -460 mV), followed by the region of hydrogen adsorption (-630 mV to -1050 mV) and finally by the onset of H_2 gas evolution. The colored CV curves in Fig. 5.6 indicate the various potential regions which are discussed in what follows with respect to charging-induced variations of the electrical resistance and the magnetic moment. All of these CVs are located within the oxygen governed regime and they are shown in steady state, which means that subsequent cycles perfectly superpose each other and thus identical electrochemical processes take place in all cycles. The CV between -465 mV and -35 mV is characterized by the formation (anodic direction, green line) and subsequent removal (cathodic direction, red line) of a thin oxygen layer to an extent of less than one oxygen atom per Pt surface atom [59]. In the narrow CV regime between -135 mV and -35 mV (yellow line) the adsorbed oxygen remains on the Pt surface and the small currents can be attributed to a pseudocapacitive charging process.

The CV between -465 mV and -35 mV (green and red) is shown in more detail in Fig. 5.7a

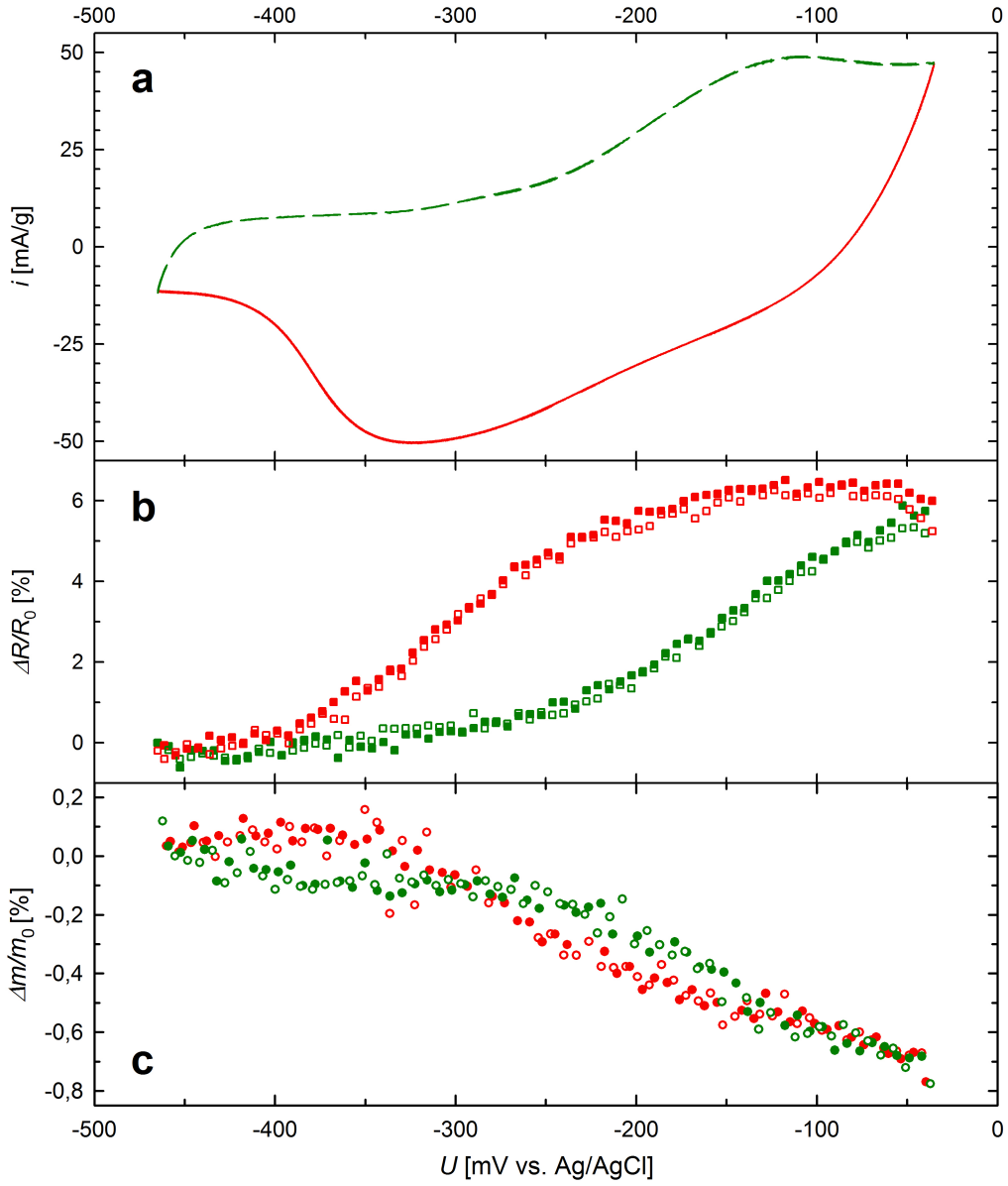

Figure 5.7: (b) Relative variation of electrical resistance $\Delta R/R_0$ and (c) magnetic moment $\Delta m/m_0$ of porous nanophase Pt upon (a) electrochemical CV-cycling in 1 M KOH between -465 mV and -35 mV (scan rate: 0.5 mV/s). The CV shown in (a) was measured for sample Pt_{ER} simultaneously with the electrical resistance R. Measurements of m were performed at a magnetic field of 5 kOe. Anodic scan indicated by green dashed line and green symbols. Cathodic scan indicated by red solid line and red symbols. To demonstrate the good reproducibility and reversibility two cycles (full and empty symbols) are shown in each plot. $R_0 = 5.84 \times 10^{-3}\,\Omega$ and $m_0 = 1.87 \times 10^{-4}$ emu correspond to the first data point of the electrical resistance and magnetic moment, respectively.

along with the corresponding variation of the electrical resistance $\Delta R/R_0$ (Fig. 5.7b) and of the magnetic moment $\Delta m/m_0$ (Fig. 5.7c). As reference values for the resistance and the magnetic moment, the initial values R_0 and m_0 of the respective measurement are used. The green- and red-colored data in Fig. 5.7b and Fig. 5.7c again indicate the anodic and cathodic scan direction. In each plot, two subsequent voltammetric cycles are shown, which hardly

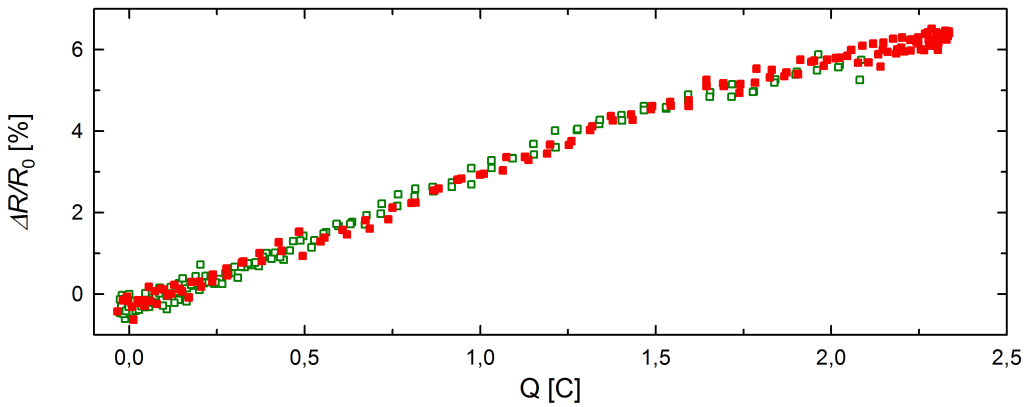

Figure 5.8: Relative variation of electrical resistance $\Delta R/R_0$ of porous nanophase Pt as a function of the transferred charge Q. The charge Q was calculated by integration of the current i of the CV shown in Fig. 5.7a. $Q = 0$ corresponds to the first data point of the electrical resistance R_0. The green/red data indicate the anodic/cathodic scan of the CV. $\Delta R/R_0$ correspond to these shown in Fig. 5.7b.

can be discerned, illustrating the good reversibility of the measurements in the steady-state CV. The electrical resistance R reversibly increases upon positive charging, exhibiting a total variation $\Delta R/R_0$ of about 6 % (Fig. 5.7b). The variation of R with the potential U exhibits a pronounced hysteresis which indicates a high sensitivity of R with respect to superficial oxygen adsorption. This sensitivity is also clearly reflected by the steep increase or decrease of R right in the CV regimes where oxygen adsorption (shoulder and plateau in anodic scan, which start to rise at $-250\,\mathrm{mV}$) or desorption (peak in cathodic scan exhibiting its extremum at $-325\,\mathrm{mV}$) takes place. Taking a closer look at the high potential edge, a further increase in R can be observed after the scan direction is reversed (start of red curve) as the charging current i is still positive. When i finally changes its sign at about $-75\,\mathrm{mV}$, also the resistance starts to decrease. This suggests that the R-variation is proportional to the transferred charge Q. This is proven by Fig. 5.8, showing the variation of the electrical resistance $\Delta R/R_0$ as a function of the charge Q transferred during the CV measurement. The linear correlation between $\Delta R/R_0$ and Q clearly indicates that the oxygen adsorption and desorption process, which mainly account for the charge flow, is the decisive factor for the variation of the electrical resistance.

In contrast to the resistance R, the magnetic moment m decreases (increases) with increasing (decreasing) the potential U (see Fig. 5.7c). A total variation of the magnetic moment of approximately 1 % occurs during cycling the potential between $-465\,\mathrm{mV}$ and $-35\,\mathrm{mV}$. The reversibility of this variation is again indicated by the fact that data for two subsequent cycles shown in Fig. 5.7c perfectly agree with each other. The variation of the magnetic moment also changes strongly with the onset of oxygen adsorption, showing a more pro-

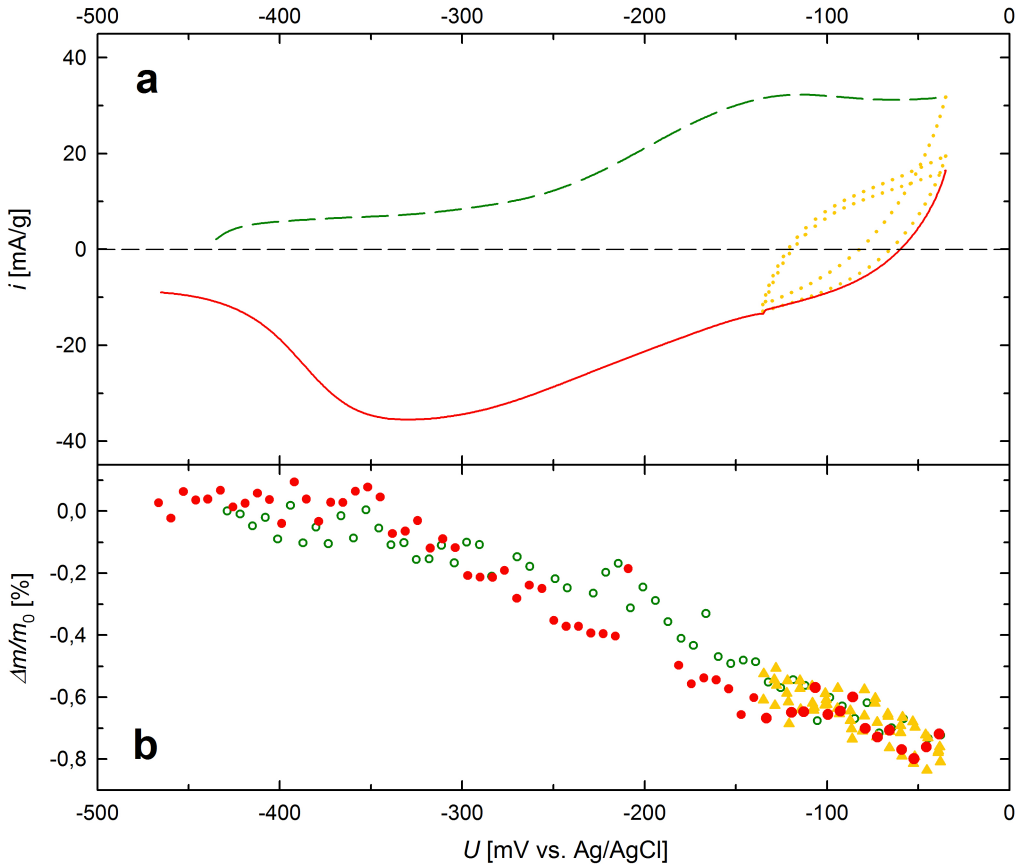

Figure 5.9: Relative variation of (b) magnetic moment $\Delta m/m_0$ of porous nanophase Pt upon electrochemical oxidation ($-435\,\mathrm{mV}$ to $-35\,\mathrm{mV}$, green: dashed line, open circles), electrochemical cycling between $-135\,\mathrm{mV}$ and $-35\,\mathrm{mV}$ (yellow: dotted line, full triangles) and electrochemical reduction ($-35\,\mathrm{mV}$ to $-465\,\mathrm{mV}$, red: solid line, full circles). (a) CV measured in-situ at the identical sample ($\mathrm{Pt_{SQUID}}$). Measurements performed in 1 M KOH with a scan rate of $0.5\,\mathrm{mV/s}$ at a magnetic field of $5\,\mathrm{kOe}$. $m_0 = 1.87 \times 10^{-4}\,\mathrm{emu}$ corresponds to the first data point of the magnetic moment.

nounced variation when oxygen is adsorbed on the Pt surface. Contrary to R, the slope of the $\Delta m/m_0 - U$ characteristic remains at a high value in the entire oxygen adsorbed regime, reversing its sign immediately at the upper potential limit of $-35\,\mathrm{mV}$. This indicates that the variation of the magnetic moment correlates with the electric field generated by the charging of the electrochemical double layer, because the charging current of the double layer reverses sign directly with the potential scan direction. This also explains why there is no hysteresis for $\Delta m/m_0 - U$ in contrast to $\Delta R/R_0 - U$.

To further demonstrate that the variation of m with applied potential is governed by capacitive processes, the variation of m was studied in more detail by cycling in the potential range between $-135\mathrm{mV}$ and $-35\mathrm{mV}$ (see Fig. 5.9). In order to do this, the sample was first oxidized (green-colored data), similar to the measurement in the potential range between $-465\,\mathrm{mV}$ and $-35\,\mathrm{mV}$. After this oxidation, the potential was cycled two times in the

potential range between −135mV and −35mV (yellow-colored data), followed by reduction (red-colored data), which was again similar to the measurement in the potential range between −465 mV and −35 mV. The same variation $\Delta m/m_0$ with potential is observed for the range between −135 mV and −35 mV, irrespective whether the CV cycling is limited to this regime (yellow-colored data in Fig. 5.9) or whether the potential is scanned through the entire regime of electrochemical oxidation (green-colored data) and reduction (red-colored data). Since in the narrow CV regime the adsorbed oxygen remains on the sample, which is indicated by the relative low currents during cycling in this regime, this leads again to the conclusion that the variation $\Delta m/m_0$ is more directly governed by the potential (i.e, the electric field) rather than by the superficial adsorption or desorption of oxygen. In contrast to these findings for m, no significant variation in R can be observed in this narrow potential range (data not shown).

5.3.2 γ-Fe_2O_3/Pt nanocomposite

At first, CVs were recorded in two different set-ups for testing the in-situ electrochemical cell used for the measurements at the γ-Fe_2O_3/Pt nanocomposite and correlating the potential of the Au quasi-reference electrode to the potential of a standard reference electrode. Beside the measuring set-up with the closed three-electrode cell mounted in the SQUID-magnetometer (see Sec. 5.2.2 for a description), measurements were conducted with the open cell being mounted into a glass vial. In this set-up, a commercial Ag/AgCl (3 M KCl) reference electrode (Metrohm Autolab, Utrecht, Netherlands) was positioned in the glass vial instead of the Au quasi-reference electrode. As for the measurements in the magnetometer, the pellet and the carbon cloth — both placed in the PTFE cell — acted as working and counter electrode, respectively.

Fig. 5.10a shows the CVs of the γ-Fe_2O_3/Pt nanocomposite measured in the two different set-ups (red solid line: ex-situ with the standard Ag/AgCl reference electrode, black dotted line: in-situ cell at an applied magnetic field of 5 kOe). Both CVs exhibit the same general shape. This demonstrates that the specially designed in-situ electrochemical cell yields reliable CVs. The slightly lower current in the ex-situ measurements performed after the in-situ measurements may be due to break off of small fragments of the brittle sample pellet or due to exposure to ambient atmosphere during sample transfer. A potential difference of approximately 325 mV between the Au quasi-reference electrode and the Ag/AgCl reference

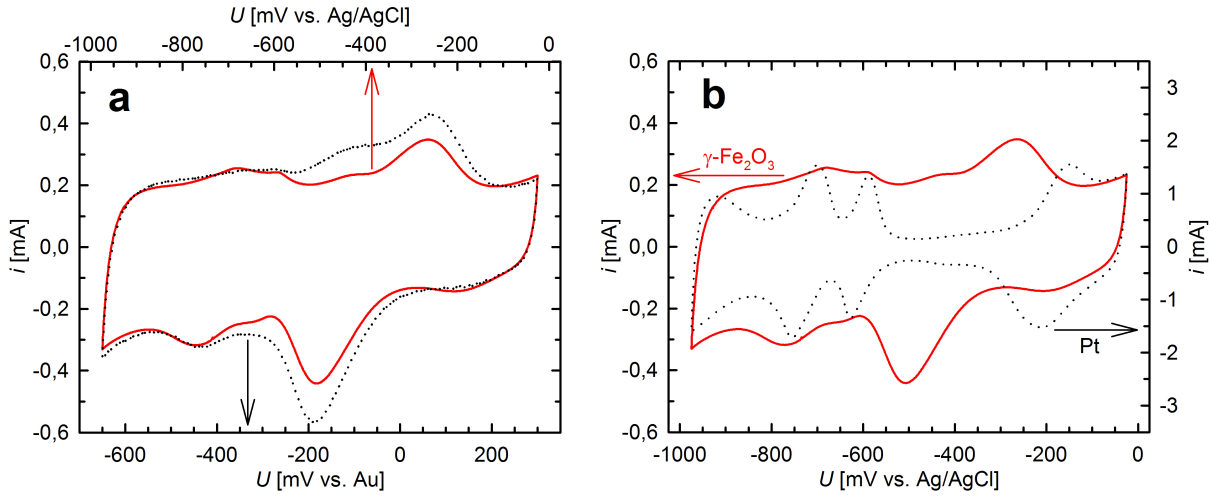

Figure 5.10: Cyclic voltammograms of porous nanophase samples measured with a scan rate of v=0.5 mV/s in 1 M KOH (in each case the last of three subsequent cycles is shown, which corresponds to the steady-state CV). (a) CVs of the γ-Fe_2O_3/Pt nanocomposite measured in two different set-ups: In-situ electrochemical cell in a SQUID magnetometer at a constant magnetic field of 5 kOe, using Au wire as quasi reference electrode (black dotted line); same cell measured ex-situ with standard Ag/AgCl reference electrode (red solid line). (b) Comparison of the CV of the γ-Fe_2O_3/Pt nanocomposite (red solid line) with that of pure Pt sample (black dotted line), both measured with a standard Ag/AgCl reference electrode outside the SQUID magnetometer. The current scales are normalized to the peak currents of the hydrogen adsorption/desorption peaks of Pt.

electrode can be deduced from this measurement[s].

In Fig. 5.10b, the CV of the γ-Fe_2O_3/Pt nanocomposite is compared with that of a pure Pt reference sample, like it was used for the measurements presented in the previous section. Both CVs were measured with the Ag/AgCl reference electrode. The CV of the Pt reference sample shows the typical features of a Pt electrode in an aqueous electrolyte, which were already described earlier. In the CV of the γ-Fe_2O_3/Pt nanocomposite, an additional broad anodic peak with a maximum at −260 mV vs. Ag/AgCl as well as a corresponding cathodic peak (−515 mV vs. Ag/AgCl) appear. These two peaks suggest that a reversible electrochemical surface reaction takes place at the γ-Fe_2O_3 nanoparticles and, therefore, will be denoted "maghemite peaks" in what follows. At potentials more negative than these maghemite peaks, the relative currents with respect to the peak currents of the hydrogen adsorption/desorption peaks of Pt are higher for the composite electrode. Possible reasons for these higher relative currents and the details of the reaction at the maghemite peaks are discussed later.

During the in-situ charging experiments in the SQUID magnetometer, cyclic voltammo-

[s] As already stated in Section 5.2.3, if not otherwise stated, the potential values in this section are given with respect to the Au quasi-reference electrode.

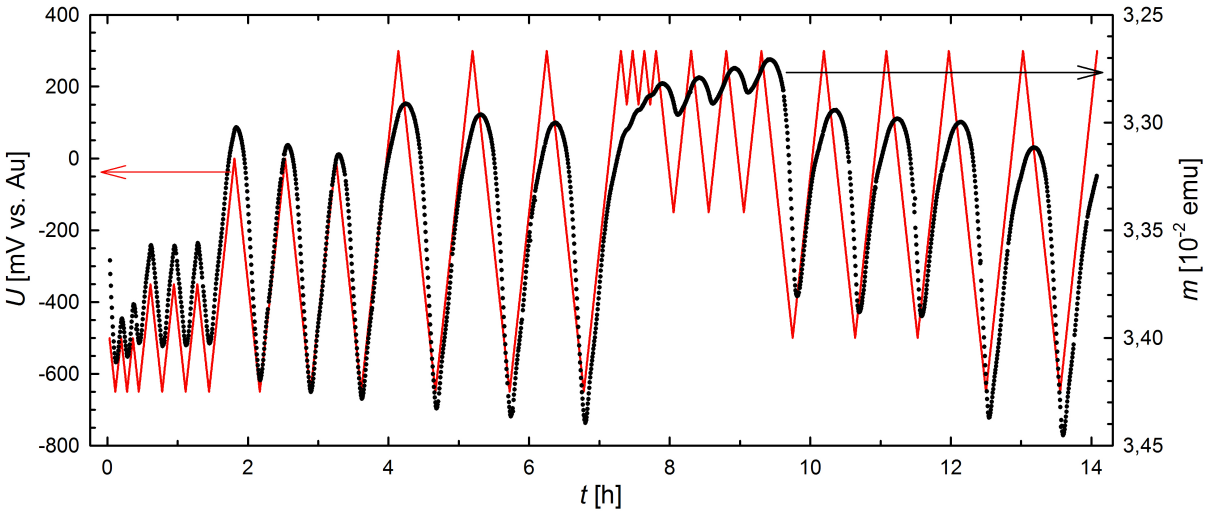

Figure 5.11: Variation of the magnetic moment m (black dots) of the porous γ-Fe_2O_3/Pt nanocomposite with time t during electrochemical cycling in different potential ranges between -650 mV and $+300$ mV in 1 M KOH at an applied magnetic field of 5 kOe. The potential U (red line) was measured versus a Au quasi-reference electrode and cycled with a scan rate v of 0.5 mV/s. Note that the direction of the m-axis (right-hand axis) is inverted to enable a better comparison of the progressions of m and U.

grams in different potential ranges were recorded simultaneously with the measurements of the magnetic moment m of the γ-Fe_2O_3/Pt nanocomposite (including the magnetic moment of the cell). In a first run, the potential was cycled several times at a scan rate of v=0.5 mV/s between -650 mV and different upper potential limits (-500, -350, 0, $+300$ mV) and subsequently between $+300$ mV and different lower potential limits ($+150$, -150, -500, -650 mV). The cycling in each of this potential range was repeated consecutively three times. As shown in Fig. 5.11, where the magnetic moment m and the potential U are plotted as a function of time t, m varies synchronously but in opposite sign direction with respect to the voltage[t]. In agreement with our previous measurements on other γ-Fe_2O_3/Pt nanocomposite samples in the two-electrode set-up [18], m increases with negative charging and decreases with positive charging with extrema close to the potential limits. With increasing the upper potential limit U_{up} from -500 mV to $+300$ mV at a fixed lower potential limit of -650 mV, the amplitude of the m-variation increases (t = 0 to 7.3 h in Fig. 5.11). When fixing U_{up} at $+300$ mV, at first only a faint oscillation of m can be discerned in the high potential range between $+150$ and $+300$ mV. Decreasing U_{low} from $+150$ mV to -650 mV, the amplitude of the variation of the magnetic moment increases again (t = 7.3 to 14 h in Fig. 5.11).

As can be seen from Fig. 5.11, a slight linear drift is superimposed to the variation of

[t] Note that the direction of the m-axis is inverted in Fig. 5.11 and Fig. 5.13 to enable a better comparison of the progressions of m and U.

m, the sign and slope of which depend on the scanned potential range. This drift of the magnetic moment might be caused by a slight shift of the potential of the Au quasi-reference electrode during cycling. The total reversible variation $\Delta m = m_{max} - m_{min}$ between the maximum (m_{max}) and minimum value (m_{min}) of the magnetic moment within one cycle after a linear drift correction is dependent on the investigated potential range (see below). The relative variation of the magnetic moment amounts up to $\Delta m/m_{min} = 4.2\,\%$. The good reproducibility and reversibility of the m-variation is not only demonstrated by the same progression of m for each of the three consecutive cycles with the same potential limits, but also by the measurements in the potential range between $-650\,\mathrm{mV}$ and $+300\,\mathrm{mV}$, which were performed twice ($t = 3.6$ to $7.3\,\mathrm{h}$ and $t = 12$ to $14\,\mathrm{h}$ in Fig. 5.11). Irrespective of the potential range studied in advance, the same variation of m is observed in both cases.

To enable a direct correlation of the variation of the magnetic moment with the ongoing electrochemical processes, the cycling of the magnetic moment in the various voltage ranges (plotted in Fig. 5.11 as a function of time) is shown in Fig. 5.12 in more detail as a function of the potential U along with the cyclic voltammograms monitored simultaneously. The numbers in Figs. 5.12a and b refer to the sequence in which the CVs were recorded. The nearly perfect overlapping cycles of the magnetic moment (each of the potential ranges was scanned three times), again demonstrates the reversibility of the voltage-induced variation of the magnetic moment. Two different regions with strong and weak voltage-induced variation of m become obvious, as indicated by the different slopes in the $m - U$ plots (Figs. 5.12c and d). Cycling in potential ranges more negative than the cathodic maghemite peak in the CV (i.e., the cycling sequences 1 and 2 (Figs. 5.12a and c)), the variation of m with U is strong, whereas in the potential ranges between $-150\,\mathrm{mV}$ and $+300\,\mathrm{mV}$ (cycling sequences 5 and 6), the variation of m with U is low (Figs. 5.12b and d). Extending the potential range so that the maghemite peaks are crossed during cycling (sequences 3, 4 and 7, 8), the voltage-induced variation of m starts to decrease in the anodic scan (upper $m - U$ branch, Figs. 5.12c and d) at approximately $-50\,\mathrm{mV}$ and then rises again at the cathodic scan at approximately $-200\,\mathrm{mV}$ (lower $m-U$ branch). This shows that the voltage-induced variation of m, i.e., the slope $\Delta m/\Delta U$ of the $m - U$ curves, changes just in the potential region of the maghemite peaks in the cyclic voltammogram.

In Figs. 5.12e and f, the magnetic moment m is plotted as a function of the accumulated charge Q, which was obtained by integrating the current of the CVs. From a linear fit of the variation of m with Q a charge coefficient $s_1{=}\Delta m/\Delta Q$ of $-3.66 \times 10^{-3}\,\mathrm{emu/C}$ is obtained

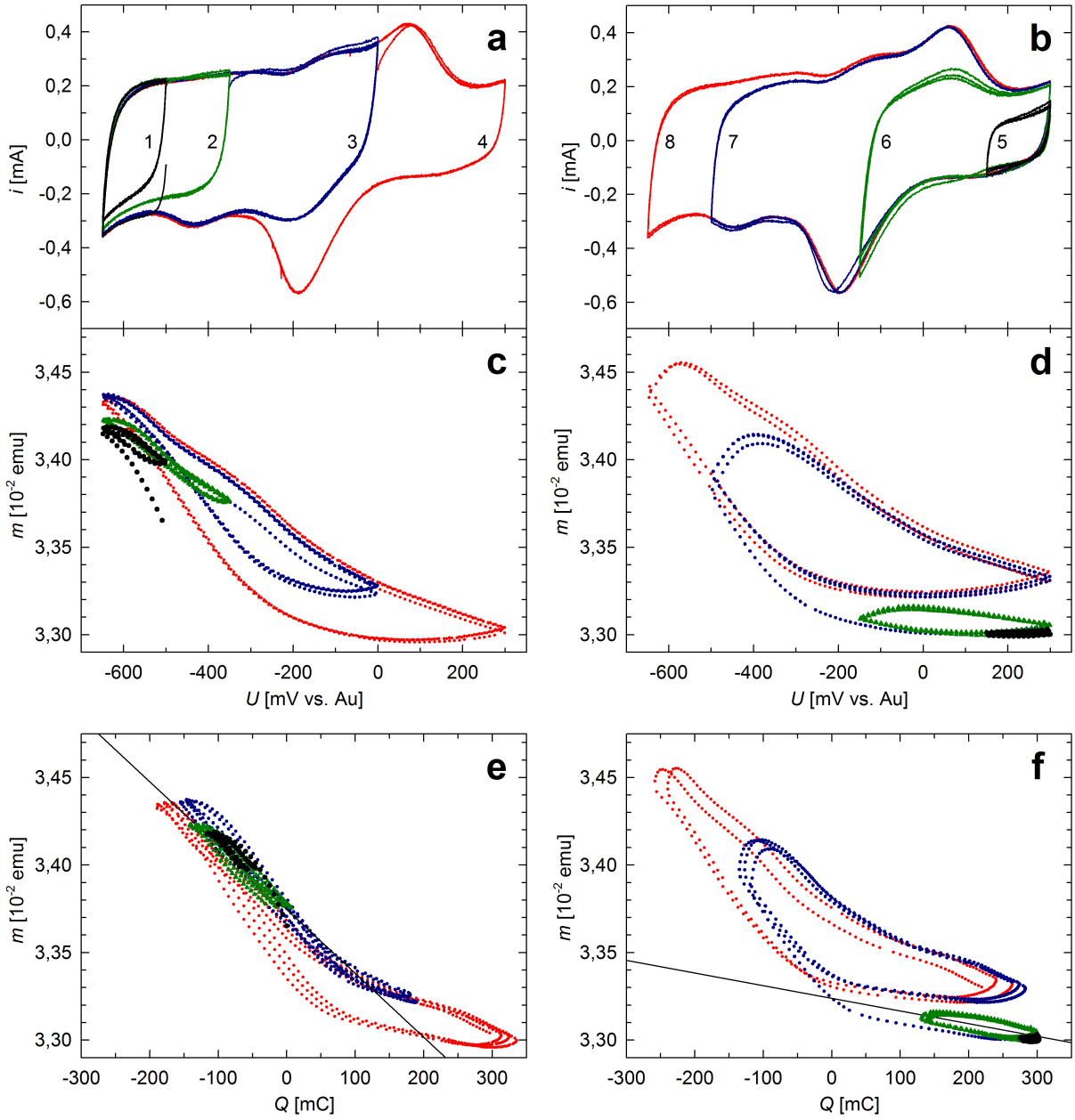

Figure 5.12: Combined magnetic and electrochemical measurements of porous γ-Fe_2O_3/Pt nanocomposite upon in-situ charging in 1 M KOH electrolyte with a scan rate v of 0.5 mV/s at an applied magnetic field of 5 kOe. (a), (b) Cyclic voltammograms (CVs) measured in-situ in SQUID magnetometer. The numbers indicate the sequence in which the CVs were recorded. Each potential range was scanned three times (compare Fig. 5.11). (c), (d) Magnetic moment m (after linear drift correction) as a function of the applied potential U measured simultaneously with CV. (e), (f) Plots of m as a function of the accumulated charge Q ((e) belongs to (a, c); (f) to (b, d)). $Q = 0$ corresponds to the first data point of m. Linear fits of the $m - Q$ behavior in the potential range -650 mV to -350 mV (e) and -150 mV to $+300$ mV (f) are plotted as faint black lines visualizing the different slopes in the two charging regions (see text, s_1, s_2).

for the potential range between -650 mV and -350 mV and $s_2 = -0.72 \times 10^{-3}$ emu/C for the range between -150 mV and $+300$ mV. As for the $m - U$ behavior, the change of the charge coefficient is related to the maghemite peaks in the CV. On the negative side, the

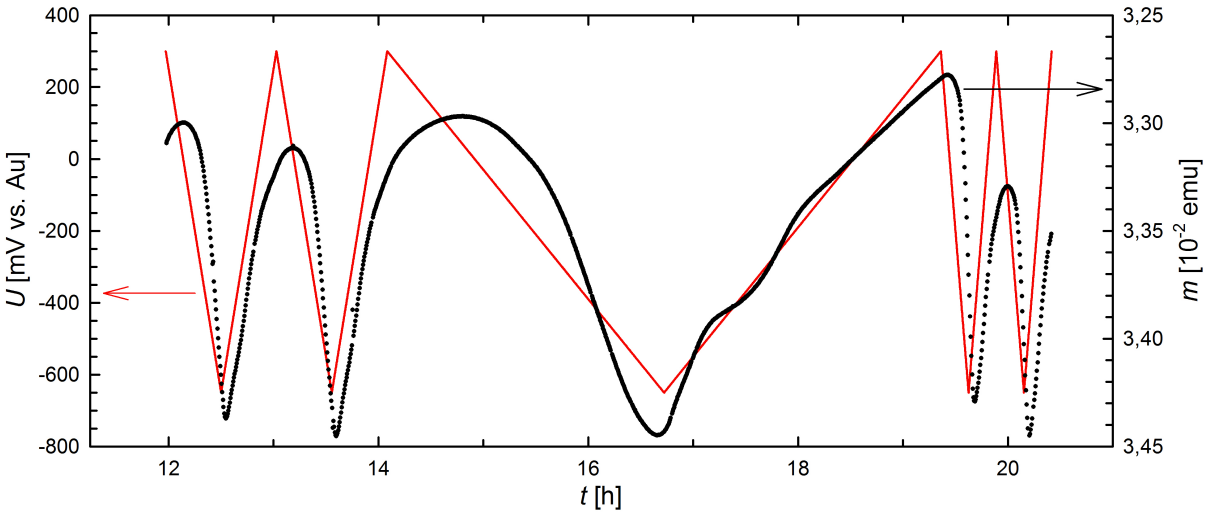

Figure 5.13: Variation of the magnetic moment m (black dots) of porous γ-Fe_2O_3/Pt nanocomposite with time t during electrochemical cycling with different scan rates v (in the sequence: 0.5 mV/s, 0.1 mV/s and 1 mV/s) in the potential range from −650 mV to +300 mV in 1 M KOH at an applied magnetic field of 5 kOe. The potential U (red line) was measured versus a Au quasi-reference electrode. The data for v=0.5 mV/s (left-hand side) are identical to those in Fig. 5.11 (right-hand side). Note that the direction of the m-axis (right-hand axis) is inverted to enable a better comparison of the progressions of m and U.

absolute value of the charge coefficient is by a factor 5 higher compared to the positive side. This indicates that electrochemical reactions of maghemite sensitively affect the tunability of the magnetic moment upon charging.

For studying the influence of scan rates v, measurements with various v (in the sequence: 0.5 mV/s, 0.1 mV/s and 1 mV/s) were performed at a fixed potential range between −650 mV and +300 mV. As shown in Fig. 5.13, the variation of m is rather similar for the different scan rates. The relative variation $\Delta m/m_{min}$ increases slightly with decreasing v from 3.7 % for v=1 mV/s to 4.9 % for v=0.1 mV/s. This indicates that slow electrochemical processes contribute to the charging-induced variation of m.

All measurements on the γ-Fe_2O_3/Pt nanocomposite sample presented so far for an applied magnetic field H of 5 kOe were also performed for magnetic fields of 50 Oe, 500 Oe and 50 kOe. These measurements were performed in a sequence starting at the highest field of 50 kOe and decreasing the field stepwise afterwards. Exemplary, the variation of the magnetic moment with cycling in the potential range between −650 mV and +300 mV is shown in Fig. 5.14 for all fields investigated. As can be seen from this figure, the general behavior of the charging-induced m-variation is the same for all fields. In particular the slope of the $m - U$ curves changes at the potentials of the maghemite CV peaks for all the fields. However, the relative variation of m becomes larger with increasing H and reaches

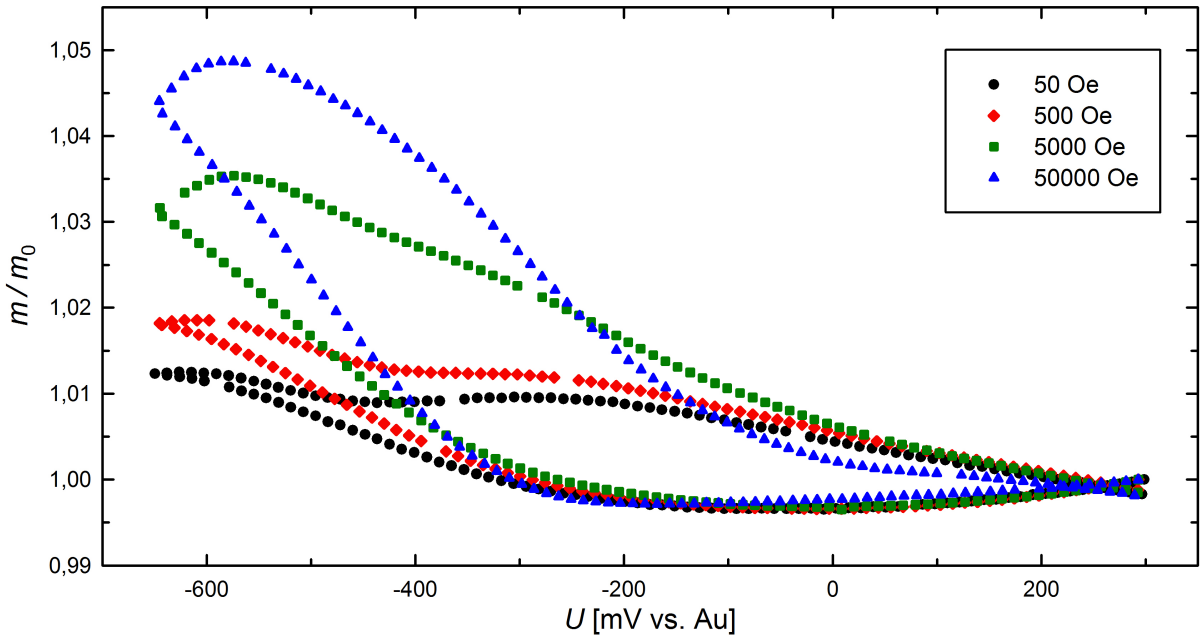

Figure 5.14: Relative variation of the magnetic moment m/m_0 of porous γ-Fe_2O_3/Pt nanocomposite during electrochemical cycling in the potential region between $-650\,\mathrm{mV}$ and $+300\,\mathrm{mV}$ as a function of the applied potential U for different magnetic fields H (see legend). U was varied with a scan rate of $0.5\,\mathrm{mV/s}$. m_0 refers to the magnetic moment at the start of each measurement (U=+300 mV).

a maximum of 4.9 % for $H = 50\,\mathrm{kOe}$. Further, it becomes obvious from this figure, that the difference between the slopes on the positive and negative side of the maghemite peaks becomes more pronounced at higher magnetic fields. For instance, the charge coefficients $\Delta m/\Delta Q$ for the two different regions in the CVs differ by a factor of 40 at $H = 50\,\mathrm{kOe}$, whereas this factor is 5 for $H = 5\,\mathrm{kOe}$.

The relative variation of the magnetic moment $\Delta m/m_{min}$ as a function of the applied field H for all the examined potential ranges is shown in Fig. 5.15. The relative variation increases with H not only for the potential range between $-650\,\mathrm{mV}$ and $+300\,\mathrm{mV}$, but rather for nearly all the examined potential ranges. The only exception is the high potential range between $-150\,\mathrm{mV}$ and $+300\,\mathrm{mV}$, where the relative variation shows a decrease when the magnetic field is enhanced from 5 kOe to 50 kOe.

In order to examine whether the charging-induced variation of the magnetic moment is caused by the γ-Fe_2O_3 nanoparticles exclusively or whether interactions between the γ-Fe_2O_3 and Pt nanoparticles play a role, additional measurements were performed on a composite sample of γ-Fe_2O_3 and high surface area carbon cloth. This sample was prepared by dropping $180\,\mu\mathrm{l}$ of a dispersion ($10\,\mathrm{mg/ml}$) of γ-Fe_2O_3 nanoparticles in ethanol on the carbon cloth. For the in-situ charging experiments in the SQUID magnetometer, this composite

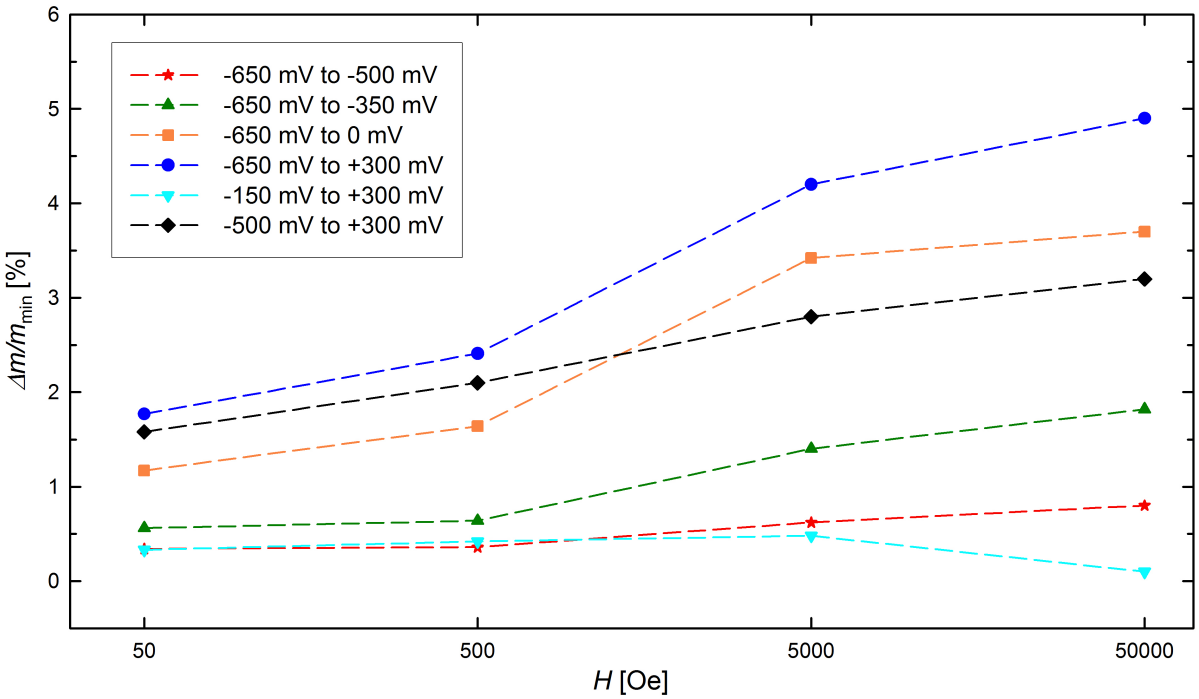

Figure 5.15: Relative variation of the magnetic moment $\Delta m/m_{min}$ of porous γ-Fe_2O_3/Pt nanocomposite during electrochemical cycling in different potential regions (see legend) as a function of the applied magnetic field H. $\Delta m = m_{max} - m_{min}$, with m_{max} and m_{min} the maximum and minimum of the magnetic moment occurring during a CV cycle. The plot comprises the data which were obtained for the measurements with a scan rate of 0.5 mV/s. Since in the high potential range between +150 mV and +300 mV only a faint oscillation of m can be discerned (see Fig. 5.11), a reliable determination of Δm is not possible. Therefore, this potential range is not included in this plot.

sample was mounted as working electrode in a two-electrode electrochemical cell as used in our earlier works [18]. Carbon cloth of the same type was used as counter electrode and 1 M KOH as electrolyte. As can be seen in Fig. 5.16, measurements of m at 50 kOe upon stepwise charging from −850 mV to +850 mV versus the carbon counter electrode causes reversible variations of m. After a linear drift correction, the variation amounts to 1.4 %. Thus, the magnitude as well as the sign of this variation are in line with the results achieved for the γ-Fe_2O_3/Pt nanocomposite. This indicates that the reversible variations of m observed for the γ-Fe_2O_3/Pt nanocomposite are not due to chemical interactions at the γ-Fe_2O_3–Pt interfaces but are exclusively due to charging of the γ-Fe_2O_3 nanoparticles. The somewhat smaller relative variation for the carbon cloth supported γ-Fe_2O_3 nanoparticles in comparison to the γ-Fe_2O_3/Pt nanocomposite is most probably due to the fact that not all γ-Fe_2O_3 nanoparticles stuck on the carbon cloth when immersing the sample in the electrolyte. Consequently only parts of the particles were affected by the charging. Indications for detached particles were found by dismantling the cell after the SQUID measurements.

Finally, test measurements were performed in order to verify that the diamagnetic response

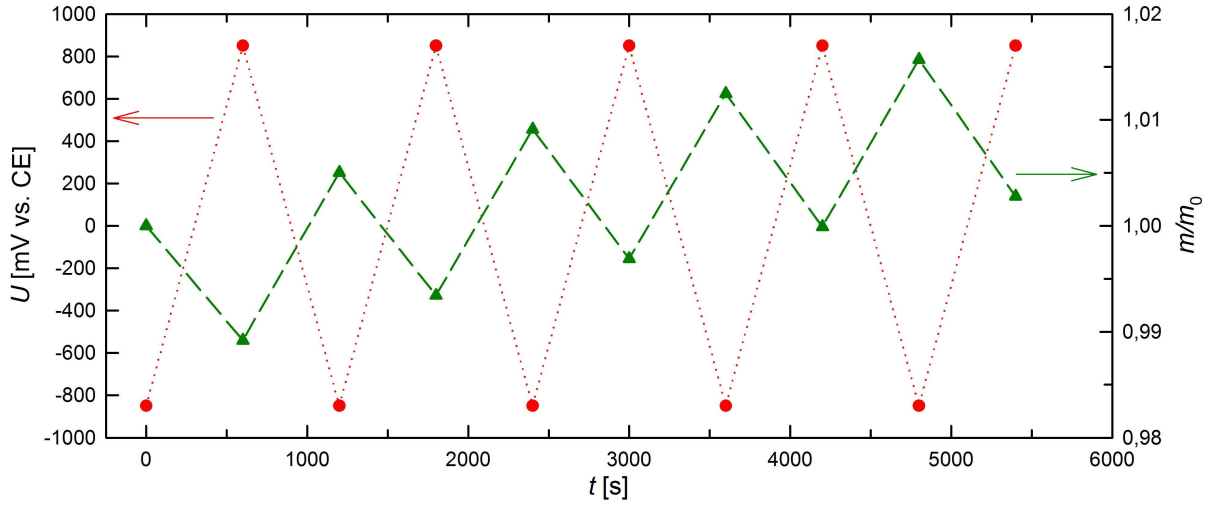

Figure 5.16: Relative variation of the magnetic moment m (green triangles) with time t of γ-Fe_2O_3 nanoparticles deposited on carbon cloth (including cell) upon electrochemical cycling between the charging voltages U (red circles) at a magnetic field of 50 kOe. The potential U was measured with respect to the carbon counter electrode. $m_0 = 8.23 \times 10^{-3}$ emu refers to the magnetic moment at the start of the measuring sequence.

of the cell does not affect the present measurements of the charging-induced variation of m. This was done by measuring the magnetic moment of an electrochemical cell without a γ-Fe_2O_3/Pt nanocomposite pellet as working electrode. These measurements showed that the electrochemical cell has a diamagnetic susceptibility in the order of -10^{-7} emu/Oe. Therefore, the influence of the cell on the measured magnetic moment is negligibly small. For 5 kOe for example, the magnetic moment m of the sample is by a factor of 54 higher than the diamagnetic response of the cell. Even the variation Δm, which occurs when cycling between -650 mV and $+350$ mV, is by a factor of 2.2 larger than the diamagnetic response. As can be seen in Table 5.2, m as well as Δm are considerably larger than the signal of the cell also for the other magnetic fields.

Table 5.2: Ratios m_0/m_{cell} and $\Delta m/m_{cell}$ of the magnetic moment m_0 or of the electrochemical charging-induced variation Δm with respect to the magnetic signal m_{cell} of the diamagnetic cell for different applied magnetic fields H. m_0 refers to the start of the measuring sequence at a distinct field and $\Delta m = m_{max} - m_{min}$ to the variation in response to cycling in the potential range between -650 mV and $+300$ mV with a scan rate of 0.5 mV/s.

H [Oe]	m_0/m_{cell}	$\Delta m/m_{cell}$
50	190	3,8
500	175	4,1
5000	54	2,2
50000	7	1,6

5.4 Discussion

5.4.1 Exclusion of parasitic effects

Before coming to the discussion of the charging-induced variations of the magnetic moment m of the Pt and the γ-Fe_2O_3/Pt nanocomposite sample, it should beensured, that the observed variations of m do not arise from parasitic effects.

A first issue to be taken into consideration pertains the question whether the current i flowing during electrochemical charging may generate a magnetic field that might give rise to a signal in the SQUID magnetometer. In such a case, the current i would influence the magnetic moment m determined by the SQUID magnetometer and variations of i would lead to variations of m.

As already shown by reference measurements in our previous studies with the two-electrode set-up, the effect of the current is negligibly small compared to the charging-induced variations of m of the γ-Fe_2O_3/Pt nanocomposite [18]. With the present measurements performed with the three-electrode set-up, the conclusion that the measured magnetic moment m is not influenced significantly by the charging current i is further supported in a more direct way. As can be seen in Fig. 5.7 for the Pt sample and in Fig. 5.12 for the γ-Fe_2O_3/Pt nanocomposite, the variations of m are not directly correlated with the variations of the charging current i in the CVs. Hence, this variations of m cannot be caused by the alterations of the current. Furthermore, the measurements on the γ-Fe_2O_3/Pt nanocomposite performed with different scan rates indicate that an appreciable interference of the charging current on the magnetic moment can be excluded. As shown in Fig. 5.13, the charging-induced variation of m is only scarcely affected by the scan rate v and the relative variation of m even decreases slightly with increasing v, whereas the charging current i increases almost linearly.

Another possible parasitic effect, which might influence the measured variation of m at an inappropriate cell design, concerns the charging of the counter electrode. The counter electrode is always charged simultaneously with the investigated working electrode (Pt, γ-Fe_2O_3/Pt nanocomposite). Thus, it cannot be excluded that the magnetic moment m_{CE} of the counter electrode also varies with charging. However, with the present cell design, it can be ensured that variations of m_{CE} do not influence the measured magnetic moment m. In the cell used for the measurements on the Pt sample (see Fig. 5.4), the counter electrode

is placed in such a way that it is located outside the SQUID pick-up coils during the whole measurement scan. Thus, solely the magnetic moment of the Pt sample is detected by this set-up, making possible variations of m_{CE} irrelevant. In case of the cell design used for the measurements on the γ-Fe_2O_3/Pt nanocomposite (see Fig. 5.5), the magnetic moment m_{cell} of the cell, including that of the counter electrode m_{CE}, is superimposed to the magnetic moment of the γ-Fe_2O_3/Pt nanocomposite. However, as shown in Table 5.2 m_{cell}, and thus m_{CE}, are significantly smaller than the measured magnetic moment m. Hence, possible variations of m_{CE} will not affect m considerably.

5.4.2 Porous nanophase Pt

The present measurements on the porous nanophase Pt sample revealed that the charging-induced response of the electrical resistance R and of the magnetic moment m - although nicely correlated - exhibits distinct different behavior. As shown in Section 5.3.1 the variation of R is directly governed by the adsorption and desorption of oxygen on the Pt surface, whereas m seems to be influenced mainly by capacitive charging currents (i.e., the electric field). Based on these results, possible underlying processes, which could lead to the observed variations of R and m, are discussed in the following paragraphs.

In the most simple picture, the electrical resistance R and the magnetic moment m depend on the charge carrier density n. As the charge carrier density is altered upon electrochemical charging, its variation $\Delta n/n$ could lead to the variation of R and of m. However, as already shown in earlier works, neither the variation of the magnetic moment nor that of the resistance can simply be attributed to a variation of the charge carrier density $\Delta n/n$ upon electrochemical charging [16,17,131,133]. A simple $\Delta n/n$-dependence for both effects can further be excluded by the present measurements because for that an equal magnitude of variation $|\Delta R/R_0| = |\Delta m/m_0|$ would have to be expected, but as shown in Section 5.3.1 the magnitude of the R- and m-variation differ by a factor of 6. The obviously weaker sensitivity of the magnetic moment to the formation and removal of a thin oxygen layer, compared to the electrical resistance, can yet be understood by looking more closely at the different magnetic and electronic response of the metal-electrolyte interface upon adsorption and desorption of oxygen species.

On the one hand, the increase in R with increasing potential U (see Fig. 5.7b) can be understood as dominated directly by surface effects in good agreement with previous results [129,133]. Besides a reduced charge carrier density due to positive charging [174] and a

shrinking conductor cross-section of Pt in favor of a superficial formation of platinum oxide with ongoing oxidation, the electrical resistance is strongly affected by charge-carrier scattering processes at the metal-electrolyte interface [129, 131, 133]. In the examined potential regime, indicated by the green/red curves in Fig. 5.6, oxygen adsorption takes place at a clean platinum surface. Since the ion transfer in this regime corresponds to less than one oxygen atom per platinum surface atom [59], each adsorbed ion may effectively act as additional charge-carrier scattering center at the platinum surface. Therefore, the resistance increases strongly in this regime and, moreover, is directly related to the transferred charge Q (see Fig. 5.8) which reflects the amount of adsorbed oxygen.

The electrochemical tunability of the magnetic moment is more than one half order of magnitude lower than that of the electrical resistance. The magnetic response is less sensitive to charging since the macroscopic magnetic moment m represents a volume average of the interior and surface regions of the Pt sample, only the latter part being affected by charging. In contrast to that, the electrical resistance, which is governed by interfacial charge carrier scattering, selectively probes the Pt-electrolyte interfaces. The observed decrease of the magnetic moment of porous nanophase Pt with electrochemically induced oxygen adsorption (see Fig. 5.7c) is in line with with earlier studies of the influence of chemisorbed oxygen on the magnetic susceptibility of Pt [175]. The trend of a decreasing magnetic moment with oxygen adsorption is also supported by recent DFT-calculations according to which the density of states at the Fermi level of Pt monotonically decreases with increasing oxygen coverage [176]. This also demonstrates that a simple minded notion of voltage-induced filling or depletion of rigid electronic bands fails, because within such a picture, positive charging, i.e., extraction of electrons from the nearly filled d-band of Pt, would give rise to an increase of the density of states rather than to a decrease.

Although oxygen adsorption causes a decrease of the magnetic moment m, it does not fully account for the observed voltage-induced variation of m. In fact, in contrast to the voltage-induced variation of R, the $\Delta m/m_0 - U$ behavior shows no hysteresis (see Fig. 5.7c) but, on the other hand, m changes also in the narrow potential regime between -135mV and -35mV where the adsorbed oxygen is not removed from the Pt surface (see Fig. 5.9). This indicates that the variation $\Delta m/m_0$ is not mainly governed by the oxygen adsorption/desorption, but rather by the electric field at the Pt-electrolyte interface.

A possible explanation of such an electric field-induced variation of the magnetic moment of Pt could be based on the electric field dependence of the Rashba spin-orbit coupling.

As known for metallic surfaces, the lack of inversion symmetry at the surface causes strong spin-orbit coupling with mobile spins (Rashba effect, see e.g. [177]). This is reflected by the formation of an effective magnetic field due to unbalanced orbital currents, which polarizes the electron spins. Indications for such a spin polarization at Pt surfaces were found by spin-polarized positron annihilation spectroscopy [178,179] and scanning tunneling spectroscopy measurements [180]. Furthermore, it was shown by Shimizu et al. [155] that spin polarization is induced in thin Pt films under electrolytic gating. Since this Rashba spin-orbit coupling varies with an applied electric field E [177, 181, 182], this may directly give rise to an E-dependence of the magnetization. In addition, the Rashba effect is also associated with a magnetic surface anisotropy [181]. The E-dependence of the latter may also cause variations of the magnetic moment in nanophase systems according to recent theoretical studies by Subkow and Fähnle [183, 184].

Finally, we briefly consider whether the present results of charging-induced m-variation may be related with charging-induced strain in combination with magnetoeleastic coupling, as sometimes discussed in literature [15,16,132,146]. Since, as shown by dilatometry measurements, the surface strain $-U$ behavior of Pt shows a hysteresis in the potential range of oxygen adsorption/desorption [123], whereas $m-U$ does not, it can be ruled out that a direct influence of the surface stress on the magnetic moment is the decisive factor for the observed variations of m of our Pt sample.

5.4.3 γ-Fe_2O_3/Pt nanocomposite

Compared to our previous studies performed with the two-electrode set-up [18], the present measurements with the three-electrode electrochemical cell enable a more precise analysis of the correlation between the m-variation and the underlying electrochemical processes. The result that the "maghemite peaks" in the CV affect the slope $\Delta m/\Delta U$ and the charge coefficient s but not directly the magnetic moment, is hardly compatible with the notion of a reversible transformation of the surface shell between Fe_3O_4 and δ-FeOOH as supposed in earlier studies [18]. Instead, this behavior rather suggests that the peaks are due to the reversible adsorption and desorption of hydroxyl ($(OH)^-$) species on the oxide nanoparticles. Indeed, hydroxyl species adsorbed on the γ-Fe_2O_3 nanoparticles at the positive potential side of the maghemite peaks do not change the magnetic moment, but may screen the electrochemical charge. Therefore, this adsorption layer may suppress a charging-induced variation of m in agreement with the low charge coefficient s found in this regime (see CVs

5 and 6 in Fig. 5.12). Upon desorption of the hydroxyl species on the negative potential side of the CV peak, on the other hand, the magnetic behavior becomes more sensitive to charging as indicated by the substantially higher charge coefficient (see CVs 1 and 2 in Fig. 5.12).

The charging-induced variation of m in the negative potential regime may either be of electronic or chemical origin. Although there are no further additional peaks assigned to the γ-Fe_2O_3 nanoparticles in the CV, the variation of the magnetic moment upon electrochemical charging could be caused by another redox reaction. Indeed, highly reversible faradaic redox processes may be characterized by pseudocapacitive currents rather than by distinct CV peaks [185]. Such type of a process was found for Fe_3O_4 electrodes by Castro et al. [186]. Among others, the authors considered a continuous transformation of the surface oxide between Fe_3O_4 and γ-Fe_2O_3 caused by a voltage-induced variation of stochiometry between Fe^{2+} and Fe^{3+} [186]. The relatively high currents in comparison to the pure Pt sample at the negative side of the maghemite CV peaks in our measurements (see Fig. 5.10b) may indeed indicate such pseudocapactive processes. More important, the formation of Fe_3O_4 upon negative charging would be in line with the observed increase of the magnetic moment since Fe_3O_4 exhibits a higher magnetic moment than γ-Fe_2O_3 [187]. This also agrees with literature, where the charging-induced variation of the magnetic moment of FePt thin films of several percent observed by Leistner et al. [21, 23, 153] was attributed to such a pseudocapacitive redox reaction in the surface oxide layer of the films.

Moreover, a consideration of the imposed charge supports the view of the pseudocapacitive redox reaction between γ-Fe_2O_3 and Fe_3O_4. By dividing the difference of the bulk magnetic moments of γ-Fe_2O_3 (87.2 emu/g) and Fe_3O_4 (95.5 emu/g) [187] by the charge necessary for the reduction of γ-Fe_2O_3 to Fe_3O_4, as proposed by Castro [186], a theoretical charge coefficient of $s_{1,theo} = -2.21 \times 10^{-2}$ emu/C is obtained. This theoretical coefficient is a factor 6 higher than the one observed in our experiment for the considered potential range ($s_1 = -3.66 \times 10^{-3}$ emu/C). A factor of this order appears to be quite reasonable owing to the fact that the major part of the charge is expected to be accumulated on the conductive Pt network.

As was evident for the pure Pt sample, alternatively to a chemically induced variation of m, electronic contributions have to be taken into consideration. As shown in recent studies, the magnetic moment of porous nanophase metals [17, 149] and alloys [15, 16, 41, 132, 146] can be reversibly varied by several percent exclusively by means of capacitive double-layer

charging. This variation of m is assigned to a combined effect of charging-induced strain and magnetoelastic coupling [15,16,132,146]. In addition, according to most recent ab-initio theoretical studies of a metallic porous nanostructure, charging may also affect the magnetic surface anisotropy and, thus, may cause variations of the magnetization of up to several percent [183,184]. Indication for a electic field-induced variation of the magnetic anisotropy could also derive from density-functional calculations of the surface magnetoelectric effect of ferromagnetic thin metal films [188]. Further, MOKE measurements revealed that the magnetic surface anisotropy of magnetic thin films [19,22,33,156] varies with electrochemical charging. Since information on charge-dependence of magnetic surface anisotropy or surface stress is not available for γ-Fe_2O_3, studied in the present work, neither of these electronic processes can be excluded.

As shown in Fig. 5.14 and Fig. 5.15, the relative variations of the magnetic moment $\Delta m/m$ becomes smaller with decreasing the magnetic field H. This suggests that the absolute variation Δm of the magnetic moment decreases more rapidly with decreasing H in comparision to m. This seems to be quite reasonable considering that Δm occurs in the surface region of the γ-Fe_2O_3 nanoparticles, whereas both the surface and the core region of the nanoparticles contribute to the magnetic moment m. As shown for γ-Fe_2O_3 [189, 190] and Fe_3O_4 [191] nanoparticles, the surface magnetization of these particles decreases more rapidly with lowering H than the core magnetization. This is due to the spin disorder in the surface regions. Indeed, also for the γ-Fe_2O_3 nanoparticles investigated in the present measurements indications for spin disordering were deduced from the reduced saturation value of m found in hysteresis measurements [169].

5.4.4 Comparison with literature

Finally, our measurements and results are compared with the literature on in-situ measurements of the magnetic properties during electrochemical charging, listed in Table 5.1. As already stated in the introduction of this chapter (Section 5.1), the main advantage of the present three-electrode set-up is the ability to record reliable cyclic voltammograms during continuous monitoring of the magnetic moment and, therefore, to correlate the variations of the magnetic moment directly to a specific electrochemical process (double layer charging, adsorption/desorption, redox reaction). As can be seen from Table 5.1, there are only few examples in literature where such a three-electrode set-up has been used. Most of those used rather indirect measurements of MOKE or Faraday ellipticity to characterize the magnetic

properties [20, 22, 33, 163], whereas the others using direct magnetometry measurements restricted their investigations to the potential regime of pure double layer charging [146, 150] or did not perform electrochemical characterization measurements at all [41]. Hence, the present combination of SQUID magnetometry and in-situ cyclic voltammetry is the sole experimental approach allowing for continuous, direct determination of the magnetic moment during electrochemical characterization measurements. The advantages of this approach become evident by comparing our measurements on the Pt and γ-Fe_2O_3/Pt nanocomposite with other studies on similar material systems.

In the case of Pt, relevant studies are those by Drings et al. [17] investigating porous nanophase Pd and by Shimizu et al. [155] dealing with Pt thin films. Both of these works lack a precise electrochemical in-situ characterization. Drings et al. [17] determined the potential range for double layer charging by ex-situ cyclic voltammetry measurements, which was then correlated to the potential range for in-situ charging in two-electrode set-up. With this method, it cannot be definitely excluded that other processes than double layer charging occur also during the in-situ measurements. Shimizu et al. [155] performed no electrochemical characterization measurements at all and their suggestion that chemical processes such as hydrogen adsorption are involved besides electrostatic effects arises solely from the behavior observed by Hall effect measurements. In contrast, the present measurements allowed for a clear distinction between the influence of electrostatic and chemical effects on the variation of the magnetic properties and, therefore, it could be shown that the electrostatic effects are the dominant ones. A further advantage of the present study, which becomes important especially at measurements on paramagnetic samples like Pt and Pd, is the reduced background signal of the cell. The electrochemical cell used by Drings et al. had a background signal of about one-half of the moment of the paramagnetic Pd sample [17]. As stated in Section 5.2.2, at our novel electrochemical cell design the measured magnetic signal arises exclusively from the Pt sample.

For pure Fe [149] and FePt [21, 23, 153] thin films, as well as for iron oxides [18, 157, 160], the observed variations of the magnetization of several percent was attributed in each case to chemical reactions. Whereas this reaction is Li intercalation and extraction in the case of iron oxides and Li containing electrolytes [157, 160], the nature of this reaction is not as obvious for the other systems. Kawaguchi et al. [149] performed no electrochemical characterization measurements and suggested an oxidation-reduction reaction at the MgO/Fe interface as possible explanation for the observed m-variations, solely based on the fact that

the large variations cannot be caused exclusively by electronic effects. As already stated above, we explained the observed variation of the magnetic moment of γ-Fe_2O_3 nanoparticles in our previous work by a redox reaction [18] and Leistner et al. [21, 23, 153] attributed the charging-induced variation of the magnetization of FePt thin films to a pseudocapacitive redox reaction in the surface oxide layer of the films. However, the in-situ charging at the latter measurements was performed in a two-electrode set-up, where the magnetic measurements were conducted solely for certain potentials and the electrochemical characterization by cyclic voltammetry was done separately in three-electrode set-ups. The present measurements on the γ-Fe_2O_3/Pt nanocomposite, however, enabled a continuous monitoring of the magnetic moment m during cyclic voltammetry measurements and revealed that m changes continuously during charging. This is considered as more direct evidence that a pseudocapacitive redox reaction is responsible for the observed m-variations.

As a last point, the obtained results of the tunability of the magnetic moment of the γ-Fe_2O_3/Pt nanocomposite, are compared in more detail with our previous measurements on another γ-Fe_2O_3/Pt sample in the two-electrode set-up [18]. The magnitude of the m-variations and the sign of the variations are in reasonable agreement with each other. However, in the present work, m-variations of up to 4.9 % were observed, whereas variations of up to 10.4 % occurred in our previous studies when charging in about the same potential range [18]. The smaller variation achieved for the γ-Fe_2O_3/Pt nanocomposite in the present work is presumably caused by a smaller fraction of the γ-Fe_2O_3 nanoparticles in the composite which is affected by charging. Indeed, as indicated by SEM and EDX measurements (see page 53), an incomplete intermixing of the Pt and γ-Fe_2O_3 nanopowders occurred for the present sample, which led to the formation of γ-Fe_2O_3-rich inclusions in the composite. The reduced fraction of only about 2 wt% of Pt present in these inclusions is obviously insufficient to guarantee a complete conducting network for quantitatively charging of the γ-Fe_2O_3 nanoparticles.

5.5 Conclusion and outlook

The present measurements on the tunability of the magnetic moment of porous nanophase Pt and of a γ-Fe_2O_3/Pt nanocomposite upon electrochemical charging have shown that the novel three-electrode electrochemical cell, allowing for in-situ cyclic voltammetry measurements in a SQUID, enables a direct correlation between the magnetic behavior and the ongoing electrochemical processes.

In the case of Pt, the comparison of the charging-induced variations of the magnetic moment with the variations of the electrical resistance upon electrooxidation revealed that these variations are governed by different processes. Whereas the reversible oxygen adsorption/desorption leads to the generation/removal of charge-carrier scattering centers and, therefore, turns out as the decisive factor for the alterations of the electrical resistance, the magnetic moment is varied mainly by the electric field E at the Pt-electrolyte interface. A possible explanation for this E-field-induced reversible variation of the magnetic moment of up to 1 % is given by a E-field-dependent spin-orbit coupling.

For the γ-Fe_2O_3/Pt nanocomposite, charging-induced reversible variations of the magnetic moment of up to 4.9 % were observed. The most remarkable feature of the present study in the three-electrode set-up is that the induced variation of the magnetic moment sensitively depends on the potential range. The slope $\Delta m/\Delta U$ changes just in the potential region of the maghemite CV peaks. Obviously, the electrochemical reactions, manifested by these CV peaks, are not reflected in discontinuous steps of the magnetic moment of the γ-Fe_2O_3/Pt nanocomposite, but the pronounced $m-U$ variation rather occurs at the negative potential side of these peaks (Fig. 5.12), even when cycling is entirely limited to this potential range (cycling sequences 1 and 2). This nicely demonstrates the major advantage of using a three-electrode set-up compared to the initial studies in the two-electrode [18], where the charge-induced variation of the magnetic moment could not be unambiguously allocated to the corresponding electrochemical regime.

Owing to the possibility of the presented measurement set-up to correlate the charging-induced variations of the magnetic moment m directly to the ongoing electrochemical processes, and thus, to distinguish if the E-field or chemical processes (adsorption/desorption, redox reactions) governs the m-variation, future measurements on different material systems could lead to a deeper understanding of the mechanisms behind these variations. Furthermore, it would be attractive to achieve larger relative variations of the magnetic moment in future experiments. One way to do so would be the application of non-aqueous electrolytes and ionic liquids, which facilitate operation in a larger potential window. Moreover, larger charging-induced effects can be obtained if a higher fraction of the magnetic phase is affected by the electrochemical charging. In the case of the γ-Fe_2O_3/Pt nanocomposite, this could be reached by a better intermixing of the γ-Fe_2O_3 and Pt nanopowders. For pure metals, an enhanced electrochemical active surface area could be obtained by preparing a nanoporous sample by means of electrochemical dealloying instead of compaction of

nanopowders. Due to its ferromagnetic character, nanoporous Ni, for which successful dealloying was reported in literature [192, 193], would be of particular interest. Nanoporous Pt [133, 194] and Pd [195], which can be prepared by electrochemical dealloying with very high surface-to-volume ratios, are interesting candidates as well, since theoretical works predict that ferromagnetism can be induced in a Pd surface under electric field gating [196].

CHAPTER 6

In-operando SQUID magnetometry on Li_xCoO_2 cathodes during charging and discharging

6.1 Introduction

Owing to the high technological relevance of Li-ion batteries, tremendous effort has been put into their further development in the last few years[u]. One focus of research is on exploring new cathode and anode materials with increased energy densities. Another focus is on a deeper understanding of the chemical and physical processes taking place in these materials during charging and discharging. For this purpose, various kinds of in-situ and in-operando techniques were developed, such as X-ray absorption and diffraction, scanning probe techniques, electron microscopy and optical spectroscopy [197–199].

Since magnetic properties of Li-ion battery electrode materials are sensitive to phase composition, structural disorder, defects and impurities as well as to the oxidation state of the transition metal ions, magnetometry offers a powerful tool to gain insights into the reaction mechanism of these electrode materials (for a review see [42]). Except for a few rare cases, all magnetic measurements on electrode materials, e.g. on the most common commercial cathode material Li_xCoO_2 [200–211], were performed ex-situ for samples of a predefined Li-ion concentration x, to mimic a specific charging state.

The advantages of magnetic in-operando compared to ex-situ measurements are quite ob-

[u] As mentioned in the introduction of this thesis (Chapter 1), parts of the content of this chapter are based on a published article (Paper V, Ref. [47]).

vious. Variations with Li concentration x cannot only be monitored continuously, but also much more precisely since imponderabilities to adjust a distinct Li-content ex-situ are avoided. Moreover, repetitive monitoring of charge cycling is indispensable and can only be performed by in-operando measurements. In addition, the in-operando technique opens up a new pathway for studying the kinetics of the atomic processes during de-/intercalation of Li-ions.

So far, the few attempts of an in-operando magnetic study of electrode materials under Li de-/intercalation were restricted to ferro- or ferrimagnetic electrode materials with high magnetic moments [158, 160]. Related to that, the aim of this work was to design an electrochemical cell allowing reliable magnetic measurements in a SQUID with optimized background signal reduction. By this means, in-operando magnetic studies on non-ferromagnetic electrode material, i.e., commercially used cathode materials, became feasible. In this thesis this novel technique is applied as a case study to Li_xCoO_2 cathodes, demonstrating not only the reliability of this new characterization method, but also providing new experimental evidence on the nature of the occurring nonmetal-metal transition, the charge compensation and possible deterioration mechanisms.

In addition to the in-operando measurements of the magnetic susceptibility, which are restricted to a temperature range in which the battery can operate, temperature-dependent ex-situ measurements were performed on Li_xCoO_2 cathodes with various predefined Li contents x, to enable a separation of the T-dependent and T-independent contributions to the susceptibility. This ex-situ measurements were performed by G. Klinser in the course of his master thesis [212] under co-supervision of this thesis' author.

The remainder of this chapter is structured as follows: First, the fundamental properties of the investigated cathode material $LiCoO_2$ are summarized in Section 6.2. The electrochemical cell used for the in-operando measurements is presented in Section 6.3.1. Section 6.3.2 deals with the experimental execution of the measurements. The results of the ex-situ and the in-operando measurements of the magnetic susceptibility of Li_xCoO_2 are given in Section 6.4, followed by their discussion in Section 6.5. Finally, the present study is concluded and an outlook for future research is given in Section 6.6.

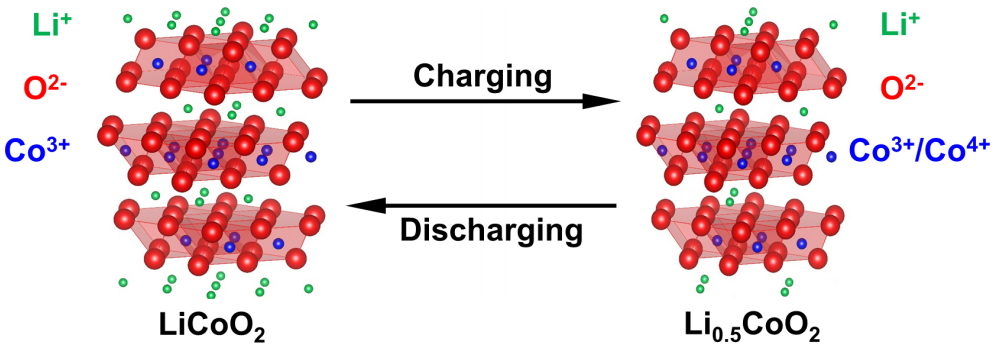

Figure 6.1: Structure (space group R$\bar{3}$m) and scheme of the conventional concept of charge compensation during charging and discharging of Li_xCoO_2 cathodes. During charging up to 50 % of Li^+ can be extracted reversibly. According to the conventional picture of charge compensation, the Co^{3+} is oxidized to Co^{4+} with Li^+ extraction, resulting in equal amounts of Co^{3+} and Co^{4+} in $Li_{0.5}CoO_2$. With discharging (Li^+ re-intercalation) the reverse process occurs. Structures drawn with VESTA [220].

6.2 $LiCoO_2$ cathodes – Fundamental properties

In 1980, Goodenough and co-workers demonstrated the ability of $LiCoO_2$ for reversible electrochemical lithium de-/intercalation [213,214], which makes it a viable cathode material for rechargeable Li-ion batteries. The commercialization of these batteries started in 1991, when SONY developed the first practical rechargeable Li-ion battery by combining the $LiCoO_2$ cathode with a carbon anode [215]. From then on, $LiCoO_2$ was the dominant cathode material used in commercial Li-ion batteries because of its high operating voltage of about 4 V, good cycle life time and ease to synthesis [216]. Although other cathode materials, like the mixed transition metal oxides, such as $LiCo_{1/3}Ni_{1/3}Mn_{1/3}O_2$, have become more prevalent over the past decade due to the scarcity and costs of Co, $LiCoO_2$ remained the most common cathode material, being used to power most of the portable electronic devices, such as cellular phones, laptops and digital cameras [217–219].

$LiCoO_2$ crystallizes in the layered α-$NaFeO_2$ structure (space group R$\bar{3}$m), where Li^+ and Co^{3+} occupy the octahedral 3a and 3b sites of a cubic closed-packed oxygen array, thus forming alternating layers along the (111) planes (see left part of Fig. 6.1). Because of this ordered structure with covalently bonded CoO_2 layers, $LiCoO_2$ exhibits a good Li^+ mobility between the CoO_2 layers and, therefore, Li-ions can be reversibly extracted from and inserted into the lithium planes. However, the Li^+ extraction from Li_xCoO_2 is limited to $x \geq 0.5$, since an irreversible structural phase transition to a monoclinic phase occurs for deeper extractions along with chemical instabilities (see e.g. [216, 221]). As the lithium content of $x = 0.5$ corresponds to a potential of 4.2 V with respect to metallic lithium, this voltage has to be chosen as upper cut-off potential, when charging should be restricted to

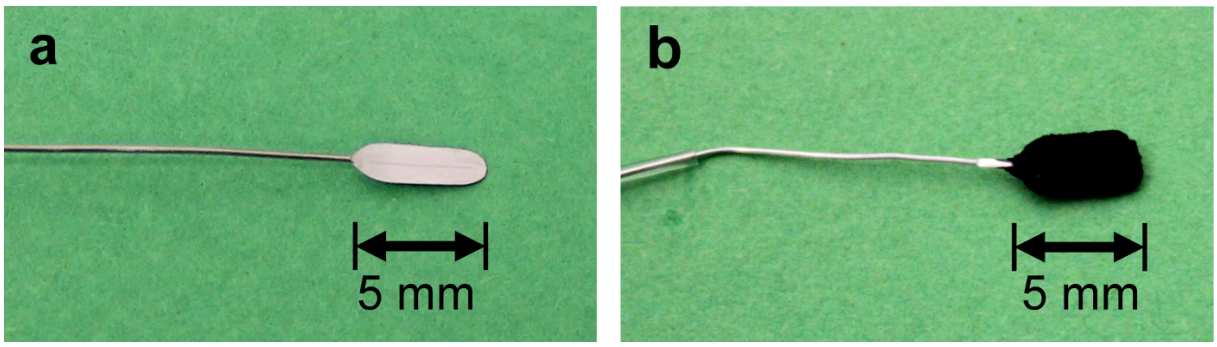

Figure 6.2: Photographs showing different steps of the preparation of the $LiCoO_2$ cathode. (a) Flattened end of the Al wire before the dip-coating process. (b) Completed cathode after the dip-coating process and pressing (see text).

the reversible regime. Due to this restriction, the theoretical capacity of 274 $mAhg^{-1}$, which corresponds to the extraction of one Li-ion per formula unit, cannot be reached in practice. Instead, the practically available maximum capacity amounts to 137 $mAhg^{-1}$.

Upon extracting the Li-ions from Li_xCoO_2 during charging of the battery, the removal of the positively charged ion has to be compensated by a hole transfer to occupied electron states. In the conventional concept of charge compensation, as it can be found in many textbooks (see e.g. [50, 222, 223]), it is assumed that the oxygen valence is fixed at O^{2-} and that only the Co^{3+} takes part in the charge compensation, resulting in a change of the cobalt oxidation state from Co^{3+} to Co^{4+} (see Fig. 6.1). Consequently, one half of the Co-ions will be in the Co^{3+} and the other half in the Co^{4+} state upon charging the battery to the limit of reversible charging, corresponding to $Li_{0.5}CoO_2$. During the discharging process, Li-ions are re-intercalated into the Li_xCoO_2 cathode and the Co^{4+} ions are reduced back to Co^{3+}. Since these changes of the electronic structure of the Co-ions upon charging/discharging are associated with variations of their spin configuration, magnetic susceptibility measurements, in particular in-operando studies, can be used to clarify if this conventional picture of charge compensation pertains.

6.3 Experimental

6.3.1 Electrochemical cell design

The $LiCoO_2$ cathode was prepared by dip-coating a flattened, about 5 mm long end of an Al wire (99.993 %, ø=0.25 mm) in an electrode slurry (see Fig. 6.2a)[v]. The composition of the

[v] The dip-coating of the $LiCoO_2$ cathodes and the preparation of the cathodes for the ex-situ measurements (see below) was performed by C. Baumann (VARTA Micro Innovation GmbH).

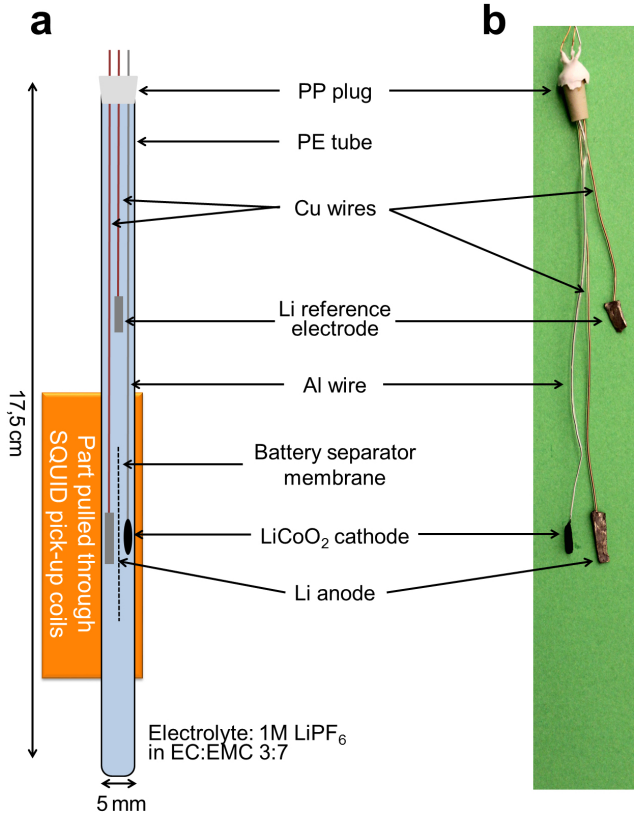

Figure 6.3: (a) Sketch and (b) photograph of electrochemical cell used for in-operando measurements of the magnetic susceptibility of the $LiCoO_2$ cathode during charging/discharging in SQUID magnetometer. The small PE tubes insulating the Al and the Cu wires, not shown in (a) for clarity, can only hardly be discerned in (b). For clarity, the battery separator membrane and the PE tube, which serves as cell compartment, were removed for the photograph shown in (b). In (b), the epoxy used for sealing (see text) can be seen on the top of the PP plug. The orange area in (a) indicates the part of the cell which is pulled through the SQUID pick-up coils during a measurement scan over a length of 6 cm.

slurry was the same as used in commercial Li-ion batteries, containing 88 wt% of $LiCoO_2$-particles as active material, 7 wt% PVDF binder (Kynar 761) and 5 wt% carbon black (Super P) dissolved in NMP (N-Methyl-2-pyrrolidone). The coated wire was dried for 16 h at 333 K in air at first, subsequently for 16 h at 353 K under vacuum (5×10^{-3} mbar). Finally, the cathode material was pressed by applying a hydrostatic pressure of about 80 MPa to ensure a good electrical contact between the cathode material and the Al serving as current collector. A photograph of the $LiCoO_2$ cathode taken after all these preparation steps is shown in Fig. 6.2b.

The electrochemical cell used for the in-operando SQUID measurements of the magnetic susceptibility of the Li_xCoO_2 cathode during charging/discharging was again designed according to the requirements given in Section 3.3. A sketch and a photograph of the cell are shown in Fig. 6.3. The cell consists of a polyethylene (PE) tube with an outer diameter of 5 mm and a length of 17.5 cm. The Al wire was positioned in the cell with the coated

part (i.e., the $LiCoO_2$ cathode) about 7 cm above the end of the PE tube. Metallic Li foils (99.98%) pressed by hand onto Cu wires (99.995%, ø=0.25 mm) served as anode and reference electrode. The anode was placed right next to the cathode to ensure that the charging/discharging process is not impeded by the transport kinetics in the electrolyte. The reference electrode was placed about 5.5 cm above the anode and cathode. Anode and cathode were isolated from each other by a polypropylene battery separator membrane (Celgard 2400) and the wires were encased in small PE tubes to prevent short circuits. As electrolyte 1 M $LiPF_6$+2 wt% vinylene carbonate in EC:EMC (1:2 by weight) was used. After filling the cell tube with the electrolyte, the tube was closed with a polypropylene (PP) plug provided with three feedthroughs for the electrode wires. Finally, the plug was made vacuum tight by gluing with epoxy resin. The entire cell assembling and sealing was performed in a glove box under argon atmosphere[w].

Like for the cells used for the Co deposition (see Sec. 4.2.1) and the studies on the porous nanophase Pt samples (see Sec. 5.2.2), the major advantage of this cell design is the minimized magnetic background signal. This reduction of the background signal is the necessary prerequisite for magnetometry on electrode materials which exhibit paramagnetic, but not ferro- or ferrimagnetic behavior, such as the commercial cathode materials like Li_xCoO_2. Again, this background reduction could be accomplished by means of an elongated homogeneous cell (PE tube, electrolyte) extending over all the three pick-up coils of the gradiometer of the SQUID during the whole measurement scan (see orange area in Fig. 6.3). However, the magnetic signal of the Li_xCoO_2 cathode is superimposed by the signal of the Li anode, since, as already mentioned above, the placement of the anode right next to the cathode is necessary for a satisfactory electrochemical performance of the cell. To enable a subtraction of this signal, measurements were performed on a reference cell without the dip-coated cathode layer, which revealed a background signal of 2.08×10^{-4} emu at a magnetic field of 5000 Oe.

6.3.2 SQUID measurement procedure

In-operando measurements

For the in-operando SQUID measurements during charging/discharging, the electrochemical battery cell was mounted into a standard plastic straw, which was attached to a modified sample rod with electrical feedthroughs for connecting the electrode terminals of the cell

[w] The cell assembling in the glove box was performed by H. Kren (VARTA Micro Innovation GmbH).

with the potentiostat. Charging and discharging was performed with a C-rate[x] of C/10, corresponding to a current of $\pm 194.5\,\mu$A, based on a nominal cathode weight of 16.13 mg and the theoretical capacitance of $137\,\mathrm{mAhg}^{-1}$ for Li_xCoO_2 (see Sec. 6.2). Charging, i.e., Li-ion extraction from the cathode, and discharging (Li-ion loading of the cathode) was limited to an upper and lower cut-off potential of 4.2 V and 3 V. In this way, the charging and discharging process was restricted to the potential range of reversible Li de/-intercalation. In this chapter, each potential is quoted in relation to the metallic lithium reference electrode.

All in-operando SQUID measurements were performed at a temperature of 300 K and at an applied magnetic field of 5000 Oe. The magnetic susceptibility was measured continuously during charging/discharging using a scan length of 6 cm with 64 data points recorded in each scan. The molar magnetic susceptibility χ_{LCO} of the Li_xCoO_2 cathode was obtained after subtracting the above mentioned magnetic background signal of the Li anode (see page 88). Variations of the background signal due to a charging-induced variation of the mass of the Li anode can be neglected, since the latter is in the range of of 2-4 % only, as estimated from the charge capacity of the cathode in relation to the mass of the Li anode. The contribution of the PVDF binder and the carbon black to the magnetic susceptibility of the cathode could also safely be neglected, since G. Klinser showed by ex-situ measurements [212] that this signal is more than a factor 30 smaller than that of the Li_xCoO_2. Furthermore, as will be discussed on page 97, this contribution is considerably less than the uncertainty coming from the background signal of the Li anode quoted on page 88.

Ex-situ measurements

To obtain Li_xCoO_2 cathodes with different Li contents x for the temperature-dependent ex-situ measurements of the magnetic susceptibility, $LiCoO_2$ was coated on aluminium foils, analogously to the dip-coating process used for the preparation of the in-operando cathode (see page 87). The Li extraction was performed in a Maccor Series 4000 battery tester with a C-rate of 0.005 using a three-electrode cell (Swagelok® T-cell), which contained a Li anode and Li reference electrode and the same electrolyte as used for the in-operando measurements. The charging time for a pre-defined Li content x was determined using the theoretical capacitance of Li_xCoO_2. In total, 13 samples with different Li contents x in the range $1 \geq x \geq 0.2$ were prepared in this way. Hence, even samples beyond the

[x] The C-rate is defined as the inverse of the time, in hours, necessary to fully charge or discharge the battery according to the practically available maximum capacity. Thus a C-rate of C/10 for $LiCoO_2$ means that charging up to 4.2 V should last 10 hours.

limit of reversible charging ($x = 0.5$) were prepared for the ex-situ measurements. For selected concentrations x, two samples were prepared to verify the reproducibility of the measurements.

The measurements of the magnetic susceptibility χ_{LCO} on these Li_xCoO_2 samples were performed in field-cooling mode in a temperature range between 300 K and 8 K at an applied magnetic field of 10 kOe. As described in detail by G. Klinser [212], a sample holder with minimized background signal, allowing for measurements in protective Ar atmosphere, was used. The sample handling before the susceptibility measurements was also performed under protective Ar atmosphere. Furthermore, a precise correction of the magnetic contribution of the Al foil and the additives (PVDF binder, carbon black) was performed at the ex-situ measurements[y].

6.4 Results

This section is divided into two parts. First, the results of the temperature-dependent ex-situ measurements, which are necessary for the interpretation of the in-operando measurements, are given in Section 6.4.1. Then, the results of the in-operando measurements are presented in Section 6.4.2.

6.4.1 Ex-situ measurements

Figure 6.4 shows the variation of the molar magnetic susceptibility χ_{LCO} of Li_xCoO_2 with temperature exemplary for three Li contents x. Both the absolute values as well as the temperature dependence vary with the Li content x. To distinguish between the temperature-dependent and independent part, the susceptibility curves were fitted using a modified Curie-Weiss law

$$\begin{aligned} \chi_{LCO} &= \chi_L + \chi_0 \\ &= \frac{C}{(T + T_N)} + \chi_0 \\ &= \frac{N_A \mu_{eff}^2}{3k_B(T + T_N)} + \chi_0 \quad \text{(cgs units)}. \end{aligned} \tag{6.1}$$

Herein, χ_L denotes the temperature-dependent Langevin susceptibility of the localized paramagnetic centers and χ_0 the temperature-independent susceptibility, which is assigned to

[y] As already stated above, this small correction was not applied for the in-operando measurements, since, as will be discussed on page 97, the uncertainty coming from the background signal of the Li anode is considerably higher than this correction.

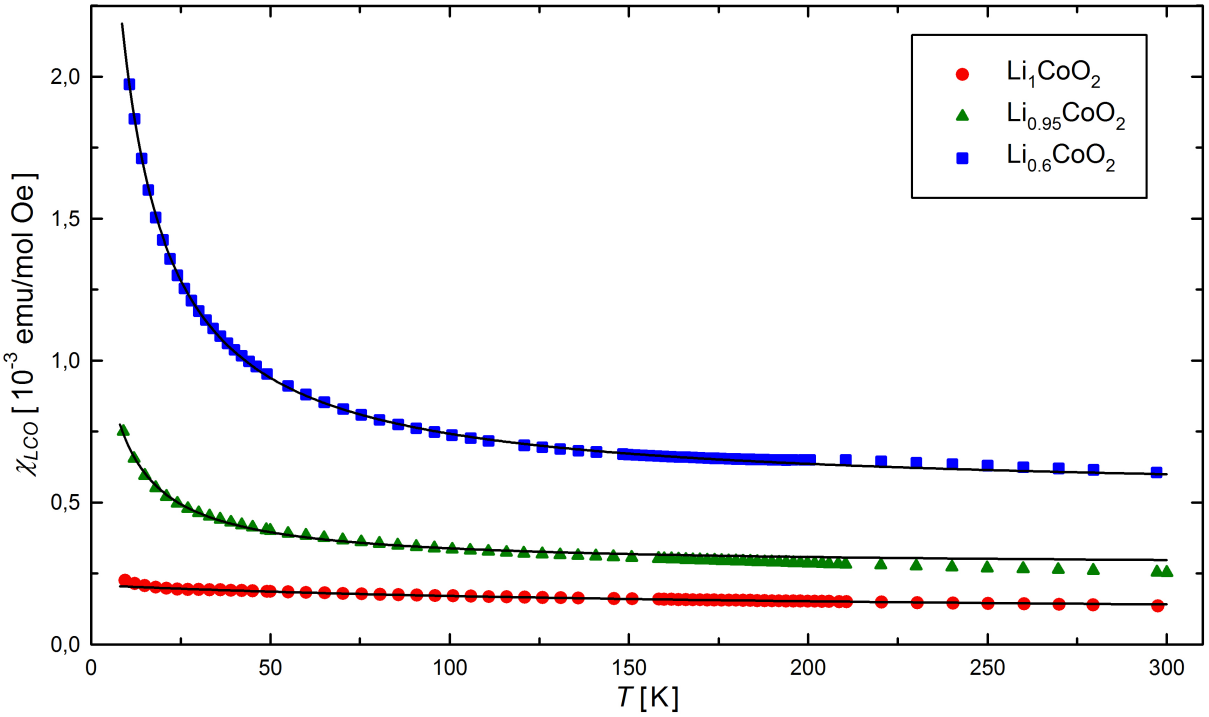

Figure 6.4: Molar susceptibility χ_{LCO} of Li_xCoO_2 (symbols) as a function of temperature T for three different lithium contents x (see legend) measured in field cooling mode at a constant magnetic field of 10 kOe. The black lines are least square fits to the data in the temperature range between 8 K and 130 K using eq. (6.1).

Pauli and Van Vleck paramagnetism (see below). C is the Curie constant, T_N the Néel temperature, N_A the Avogadro constant, μ_{eff} the effective magnetic moment of the paramagnetic centers and k_B the Boltzmann constant. In case of 3d-metal ions, like Co, as magnetic centers, the orbital magnetic moment is quenched and, therefore, the effective magnetic moment is given by

$$\mu_{eff} = \sqrt{S(S+1)}\mu_B, \tag{6.2}$$

with S the spin quantum number. Due to kink-like behavior in the T range between 140 K and 160 K for certain Li-contents x (see [212] for details), fitting was restricted to $T \leq 130$ K. As can bee seen from Fig. 6.4, the magnetic susceptibility data are well described by the modified Curie-Weiss law in this temperature range. The slight deviation of the Li_1CoO_2 curve from the fit at low temperatures comes from antiferromagnetic ordering which occurs below 35 K. Due to this discrepancy, the values of χ_L and χ_0 for Li_1CoO_2 cannot be obtained accurately from the fit and are therefore not considered further.

In Fig. 6.5, the magnetic susceptibility χ_{LCO} measured at 300 K (which corresponds to the most-right data points of the $\chi_{LCO} - T$ curves in Fig. 6.4) is plotted as a function of the Li content x, together with the contributions χ_0 and χ_L of the T-independent and the

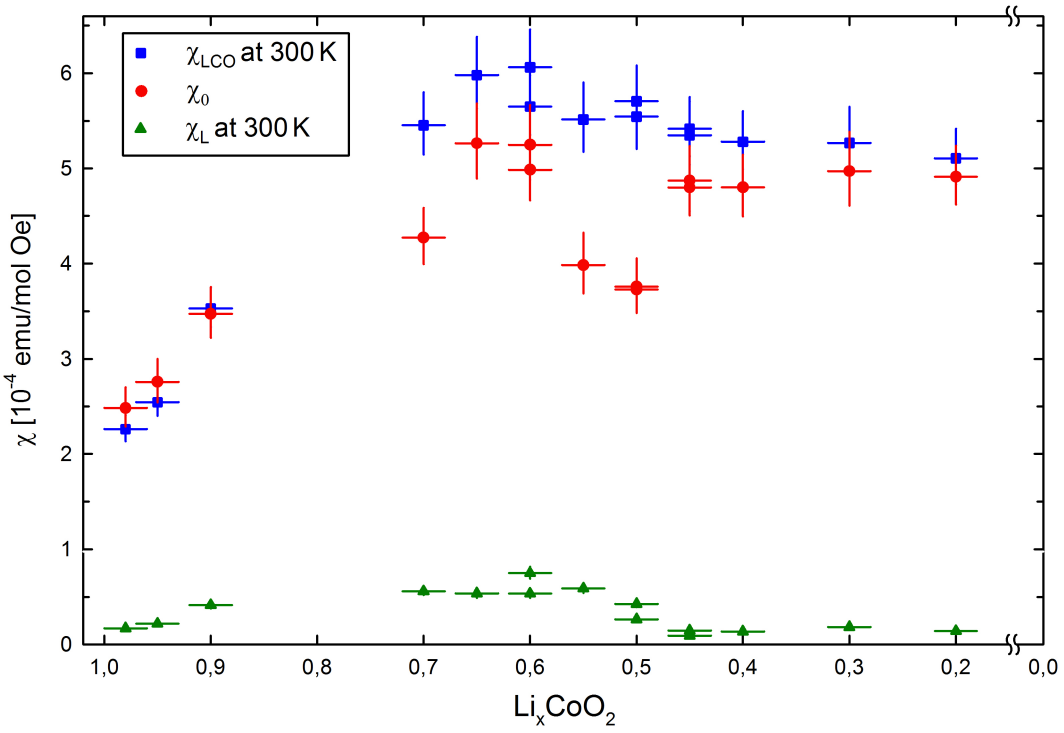

Figure 6.5: Different contributions to the magnetic susceptibility of Li_xCoO_2 cathodes at $T = 300\,K$. χ_{LCO}: total magnetic susceptibility measured at 300 K (corresponds to the most-right data points of $\chi_{LCO} - T$ curves in Fig. 6.4), χ_0: temperature-independent part of the magnetic susceptibility, χ_L: temperature-dependent Langevin part of the magnetic susceptibility at $T = 300\,K$ (see eq. (6.1)). The vertical error bars of χ_L are too small to be visible in the present scaling.

T-dependent part. First, it should be noted that $\chi_{LCO} = \chi_L + \chi_0$ is not strictly valid for the data shown in this figure, since the values of χ_L and χ_0 were obtained by fitting eq. (6.1) to the susceptibility data in a T-range between 8 K and 130 K, whereas χ_{LCO} is the magnetic susceptibility measured for $T = 300\,K$. It becomes obvious from Fig. 6.5 that for $T = 300\,K$ the main contribution to the magnetic susceptibility χ_{LCO} comes from the temperature-independent part χ_0. χ_0 first increases continuously with Li extraction and reaches a constant value for $x \leq 0.65$, except for $Li_{0.55}CoO_2$ and $Li_{0.5}CoO_2$, for which slightly reduced values are found. As stated by Motohashi et al. [207], these exceptions as well as a reduced value of χ_0 for $Li_{0.7}CoO_2$ may arise due to the kink-like behavior of the $\chi_{LCO} - T$ curves for this Li concentrations x (see [212] for details). For χ_L, an increase is observed with Li-ion extraction for $1 \geq x > 0.55$, which is most pronounced for $1 \geq x \geq 0.7$. In the vicinity of the limit of reversible charging ($0.55 \geq x \geq 0.45$), χ_L shows a strong decrease. For the Néel temperature T_N, the fits provided values in the range of 3-14 K.

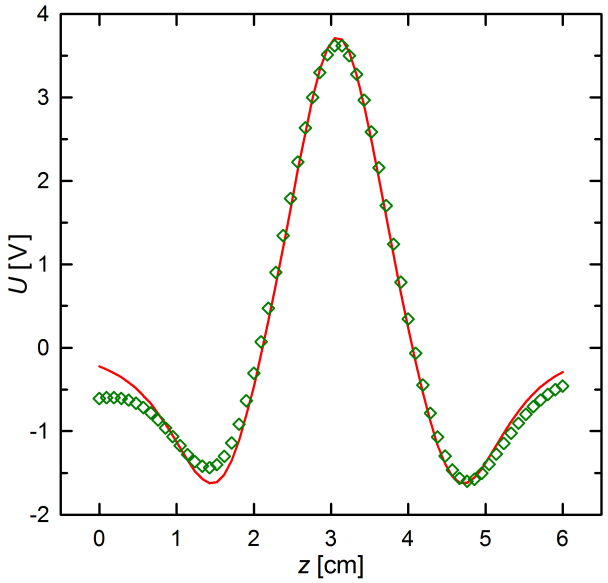

Figure 6.6: Measured SQUID output voltage curve (symbols) and corresponding fit (line) for the first data point of the magnetic susceptibility χ_{LCO} obtained at the in-operando measurements on Li_xCoO_2 shown in Fig. 6.7.

6.4.2 In-operando measurements

First, to verify that reliable values of the magnetic susceptibility are measured at the SQUID measurements with the electrochemical cell, the SQUID output voltage curve and the corresponding fit are shown in Fig. 6.6 exemplary for the first data point of χ_{LCO} of the in-operando measurements in Fig. 6.7. The good coincidence of the data and the fit indicates that the magnetic signal arises solely from the centered parts of the cell, i.e., the Li_xCoO_2 cathode and the Li anode, and that accurate values of χ_{LCO} are obtained at the in-operando measurements. The slight deviations, which occur especially for $z \leq 2\,\text{cm}$, most probably stem from a small vertical displacement of the Li_xCoO_2 cathode and the Li anode. However, since these small discrepancies have no significant influence on the amplitude of the fit, the χ_{LCO} value determined from this fit is not affected considerably.

The variation of the magnetic susceptibility χ_{LCO} of the Li_xCoO_2 cathode upon three consecutive charging/discharging cycles is shown in Fig. 6.7 along with the electrode potential U. A detailed view of the start of the first charging cycle is given in Fig. 6.8. The electrode potential U shows the typical loading/unloading curves characteristic for $LiCoO_2$ cathodes demonstrating the reliable performance of the electrochemical SQUID cell. Prior to charging, the cell was kept in an open circuit mode for 10 min, during which the electrode potential U and χ_{LCO} stayed constant (see $t = 0$ to 10 min in Fig. 6.8). With the onset of the charging, i.e., Li extraction, χ_{LCO} starts to increase linearly immediately. As can be seen

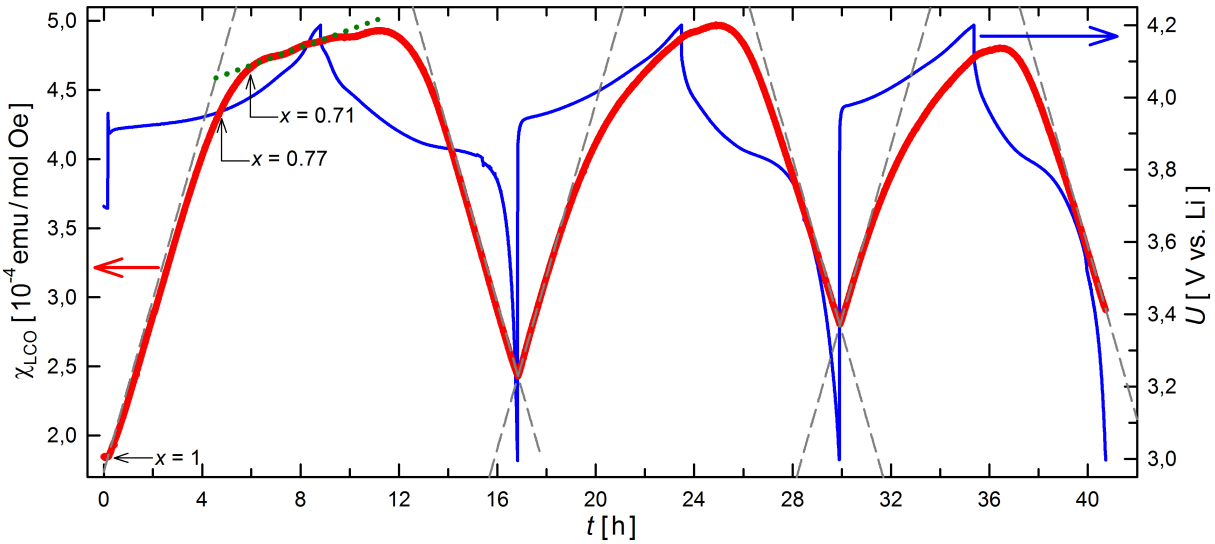

Figure 6.7: Magnetic susceptibility χ_{LCO} of the Li_xCoO_2 cathode (red line) and electrode potential U (blue line) as a function of time t during three consecutive cycles of charging/discharging with a nominal C-rate of C/10. The gray dashed lines indicate the theoretical slope s_{LCO} of the magnetic susceptibility for the reversible transition between Co^{3+} (S=0) and Co^{4+} (S=1/2) which would correspond to a pure Langevin paramagnetism of localized moments. But as discussed in the text, delocalized Pauli paramagnetism prevails. Several Li contents x are indicated in the first charging cycle for the discussion. The green dotted line is a linear fit to χ_{LCO} for $x \leq 0.71$ of the first charging cycle (see discussion). An enlarged view of the measurement onset is given in Fig. 6.8.

from Fig. 6.7, this increase prevails with a constant rate for about 5 hours and afterwards proceeds with a reduced constant rate. This increase at a reduced rate even continues after the first charging cycle is stopped at the upper cut-off potential of 4.2 V after 8.65 hours and discharging, i.e., Li re-intercalation, sets in. The maximum of χ_{LCO}, which is 167 % higher than the initial value of χ_{LCO}, is reached at $t = 11.25$ h after about 2.4 hours of discharging. Subsequently, χ_{LCO} decreases after about one further hour, with the same absolute rate as during charging, until the first discharging cycle is stopped after 8 hours at $t = 16.8$ h by reaching a potential of 3 V. Upon starting the second charging cycle, the variation of χ_{LCO} reverses its sign instantaneously, leading again to the same linear rise as in the first cycle. Thereafter, the behavior of χ_{LCO} in the second and third charging/discharging cycles is qualitatively the same as in the first one.

The charging times (t_{charge}) and discharging times ($t_{discharge}$) of the three consecutive cycles of the in-operando measurement are given in Table 6.1. As can be seen from this table, the charging cycles are shorter than the expected 10 hours, which were defined by choosing a C-rate of C/10. This indicates a reduced capacity presumably because not the entire cathode material contributes to charging/discharging because of structural inhomogeneities and thickness variations of the dip-coated layer. Furthermore, a loss of small fragments

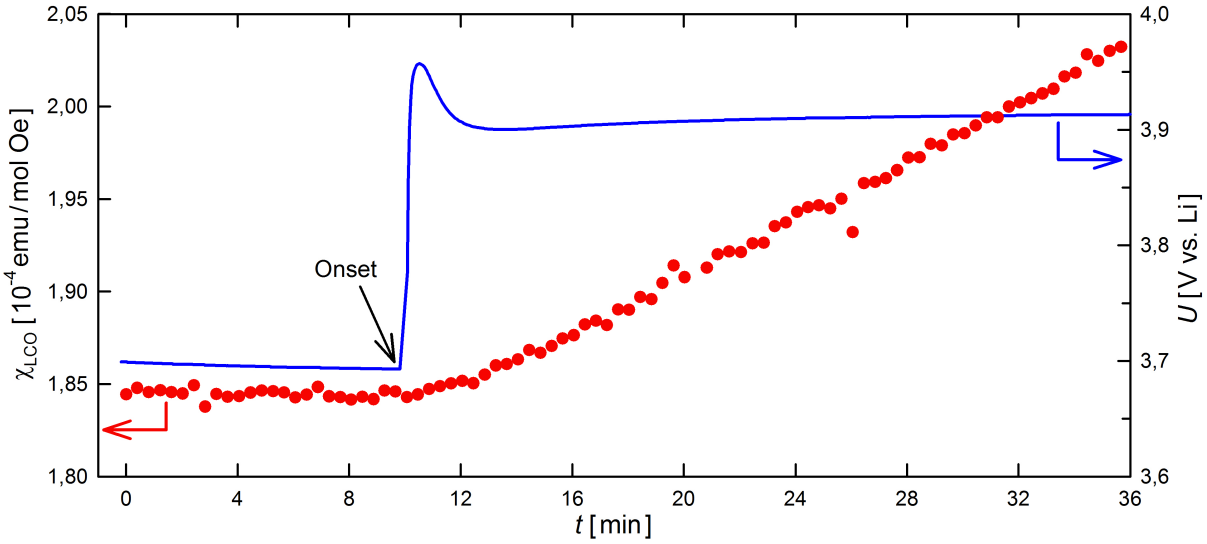

Figure 6.8: Detailed view showing the magnetic susceptibility χ_{LCO} of the Li_xCoO_2 cathode (red dots) and electrode potential U (blue line) as a function of time t at the onset of the first charging cycle. The cell was kept in an open circuit mode until the charging with a current of $+194.5\,\mu A$ was started at $t = 10\,min$. The further progression of χ_{LCO} and U during 3 consecutive cycles of charging/discharging is shown in Fig. 6.7.

of the brittle cathode during assembling the cell cannot be excluded. However, an effect of such a loss on a reduction of the capacity is considered to be small and, therefore, not quantitatively taken into consideration. Moreover, the fact that $t_{charge} > t_{discharge}$ indicates that the fully Li-loaded initial state is not restored. This is also reflected by the higher value of χ_{LCO} after the end of the first discharging step ($t = 16.8\,h$ in Fig. 6.7) in comparison to the initial χ_{LCO} value. A likely reason may be a slight misalignment of cathode and anode, which causes that not the entire Li can be re-intercalated into the Li_xCoO_2 cathode in the discharging cycle. This misalignment could also explain the decrease of the charging times from cycle to cycle, since Li that was not re-intercalated in the preceding discharging cycles is not available in the following cycles. However, as discussed below, the possible formation of Co^{2+} during reduction may also play a role at the deterioration of the battery performance.

Table 6.1: Charging times (t_{charge}) and discharging times ($t_{discharge}$) of the Li_xCoO_2 cathode during the three consecutive cycles of the in-operando measurement shown in Fig. 6.7.

Cycle	t_{charge} [h]	$t_{discharge}$ [h]
1	8.65	8.00
2	6.66	6.41
3	5.45	5.36

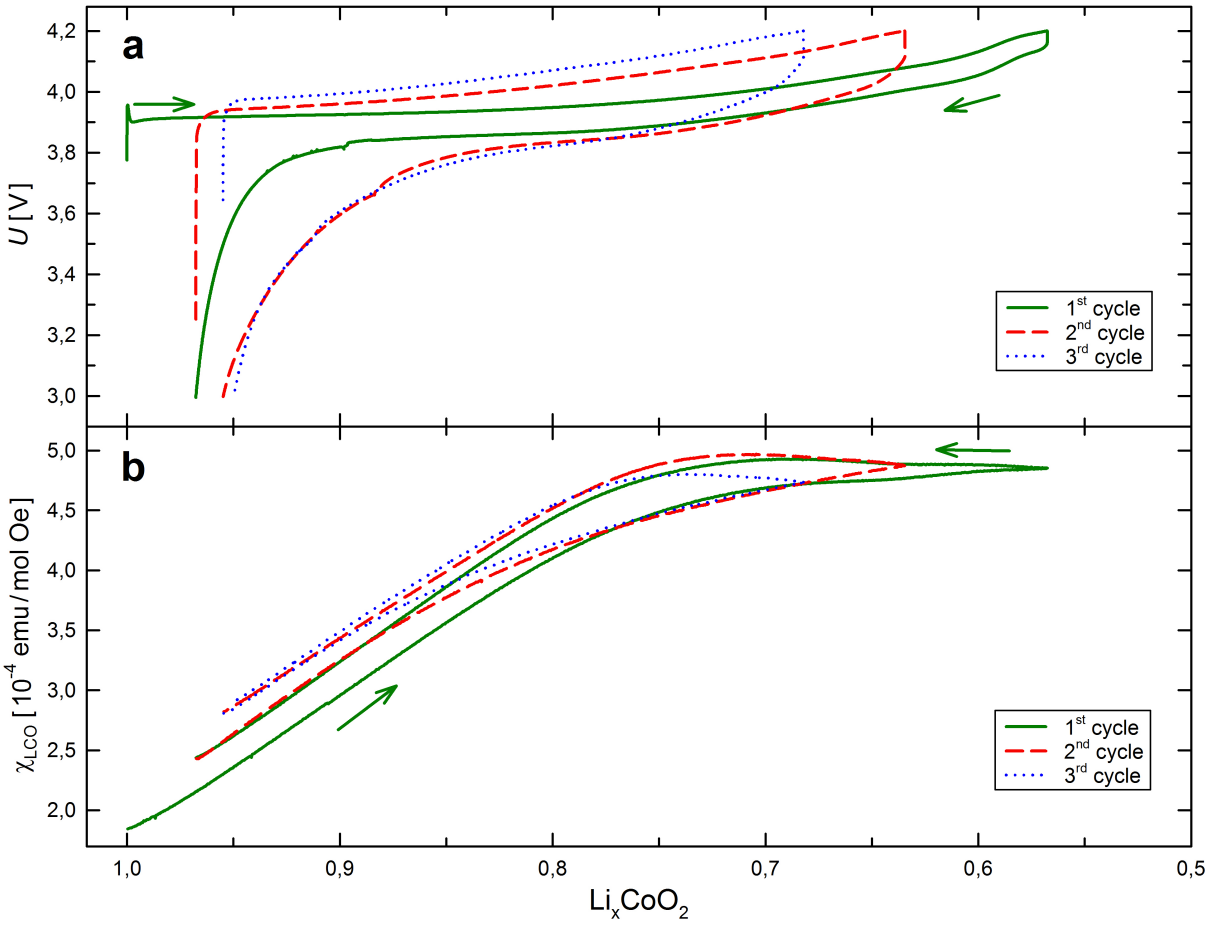

Figure 6.9: (a) Electrode potential U and (b) magnetic susceptibility χ_{LCO} of the Li_xCoO_2 cathode measured with the in-operando electrochemical cell as a function of the Li content x.

6.5 Discussion

For the discussion of the results, the susceptibility χ_{LCO} of the Li_xCoO_2 cathode is plotted in Fig. 6.9 as a function of the Li content x for the three consecutive cycles of in-situ charging/discharging, along with the electrode potential U. The Li content x was calculated based on the nominal cathode mass and on Faraday's law, assuming that the current is entirely caused by Li de-/intercalation. As can be seen from this figure, χ_{LCO} varies linearly with the Li content for $1 > x \geq 0.77$. This linear increase of χ_{LCO} is addressed in the first part of the discussion (see Sec. 6.5.1). The regime $x \leq 0.77$, in which the increase of χ_{LCO} with decreasing Li content x is reduced considerably, is discussed in Section 6.5.2.

Before these discussions, the results of the in-operando measurements of the magnetic susceptibility of the Li_xCoO_2 cathode should be compared with the results of the ex-situ measurements. For this purpose, χ_{LCO} of the first charging cycle of the in-operando measure-

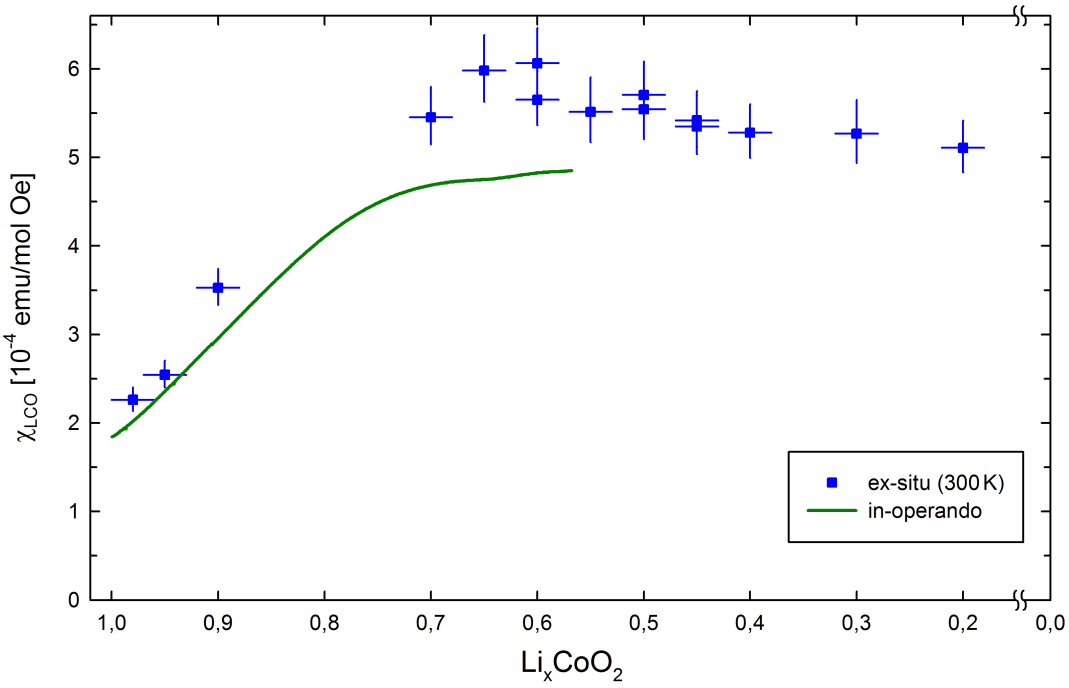

Figure 6.10: Comparison between the in-operando (green line) and the ex-situ (blue symbols) measurements of the magnetic susceptibility χ_{LCO} of Li_xCoO_2 as a function of Li content x. The ex-situ data are the data points which were obtained at the temperature dependent measurement for $T = 300\,\mathrm{K}$.

ments is plotted in Fig. 6.10 as a function of the Li content x together with the χ_{LCO} values of the ex-situ measurements for 300 K. This comparison shows that the same $\chi_{LCO} - x$ progression is obtained by the in-operando and the ex-situ measurements, confirming the reliability of the presented in-operando technique. Furthermore, this figure demonstrates that the major advantage of the in-operando measurement is the continuous monitoring of the charging-induced variation of χ_{LCO}. Whereas the ex-situ measurements suggest that the strong linear increase of χ_{LCO} with Li extraction continues until a Li content of $x = 0.7$, the in-operando measurements show that the slope of the χ_{LCO} variation changes already at $x = 0.77$. The slight deviation in the absolute values of the magnetic susceptibility between the in-operando and ex-situ measurements most probably arises from uncertainties of the background subtraction. As stated in Section 6.3, for the in-operando measurements the magnetic background signal of the Li anode has to be subtracted to obtain the magnetic susceptibility χ_{LCO}. Since this background signal of 2.08×10^{-4} emu at a magnetic field of 5000 Oe determined by measurements on a reference cell (see page 88) is of the same order of magnitude as the magnetic signal of the Li_xCoO_2 cathode, a slightly different amount of metallic Li used as anode in the cells is most probably the cause of this deviation.

6.5.1 Li_xCoO_2 concentration range: $1 > x \geq 0.77$

For the discussion of the strong linear variation of χ_{LCO} for $1 > x \geq 0.77$ (see Fig. 6.9), at first the simple conventional notion of charge compensation is adopted according to which Li extraction is associated with the oxidation of Co from Co^{3+} to Co^{4+}. Here, pure Langevin paramagnetism of localized magnetic moments is assumed, i.e., only the first part χ_L of eq. (6.1) is considered[z]. Regarding that both the Co^{3+} ions (S=0) [205, 207, 224] and the Co^{4+} ions (S=1/2) [203, 207, 224] are in the low-spin state, the oxidation of the Co from Co^{3+} to Co^{4+} corresponds to an increase of the molar magnetic susceptibility of

$$\begin{aligned}\Delta\chi &= \chi_{L,Co^{4+}} - \chi_{L,Co^{3+}} \\ &= \frac{N_A\left[2\sqrt{\frac{1}{2}\left(\frac{1}{2}+1\right)}\right]^2}{3k_BT} - 0 \\ &= 1.25\times10^{-3}\,\mathrm{emu/(mol\ Oe)} \quad (\text{for } T = 300\,\mathrm{K}).\end{aligned} \tag{6.3}$$

By charging the cathode with the current i of 194.5 μA, the total number of moles of Co which are transformed from Co^{3+} to Co^{4+} per second is given by

$$N_{total} = \frac{i}{eN_A} = 2.02\times10^{-9}\,\mathrm{mol/s}. \tag{6.4}$$

Taking into consideration the nominal cathode mass m of 16.13 mg of which 88 wt% are apportioned to $LiCoO_2$, the number of $LiCoO_2$ moles in the cathode N_{LCO} can be calculated by

$$N_{LCO} = \left(\frac{0.88m}{M_{LCO}}\right) = 1.45\times10^{-4}\,\mathrm{mol}, \tag{6.5}$$

where M_{LCO} denotes the molar mass of $LiCoO_2$ of 97.87 g/mol. The molar fraction of Li_xCoO_2, which is transformed from Co^{3+} to Co^{4+} per second, is given by the ratio of eq. (6.4) and (6.5):

$$x_{LCO} = \frac{N_{total}}{N_{LCO}} = 1.39\times10^{-5}\,\mathrm{s^{-1}}. \tag{6.6}$$

The product of x_{LCO} and $\Delta\chi$, i.e., the variation of the molar magnetic susceptibility according to eq. (6.3), yields the expected slope s_{LCO} of the $\chi_{LCO} - t$ variation:

$$s_{LCO} = x_{LCO}\times\Delta\chi = 1.73\times10^{-8}\,\mathrm{emu/(mol\ Oe\ s)} \quad (\text{for } T = 300\,\mathrm{K}). \tag{6.7}$$

This slope is illustrated by the gray dashed lines in Fig. 6.7. It fits remarkably well the experimental data in the regime of the constant high rate, i.e., for $x \geq 0.77$. Despite this

[z] For the following calculations, antiferromagnetic ordering is neglected (T_N =0), since, as stated above, T_N is rather small.

good agreement with a Langevin-type behavior of localized moments, the temperature-dependent ex-situ measurements revealed that the temperature-independent susceptibility χ_0 prevails. As can be seen from Fig. 6.5, χ_0 dominates by far at 300 K and at most one eighth of χ_{LCO} originates from localized moments (i.e., from χ_L with Langevin behavior). The prevalence of χ_0 was further demonstrated in a couple of ex-situ studies [202–204, 206–208, 210, 211]. Hence, the strong linear increase of χ_{LCO} for $x \geq 0.77$ cannot be explained by variations of the Langevin-term χ_L of the susceptibility, but rather by variations of the temperature-independent susceptibility χ_0.

This temperature-independent part of the susceptibility χ_0 is attributed to Van Vleck and Pauli paramagnetism [42, 201, 203, 205, 207, 225]. Since the Van Vleck paramagnetism is hardly affected by electron hole formation upon Li extraction, the observed variation of χ_0 has to be attributed entirely to Pauli paramagnetism. Given that the charging-induced linear variation of χ_{LCO} for $x \geq 0.77$ is due to changes of the Pauli susceptibility $\chi_P = \mu_0 \mu_B^2 D(E_F)$, this indicates that the density of states at the Fermi level $D(E_F)$ varies linearly with Li de-/intercalation for $1 > x \geq 0.77$. As $D(E_F) = 0$ for Li_1CoO_2 [226], a value of $D(E_F) = 6.8\,eV^{-1}$ can be derived for $Li_{0.77}CoO_2$ from the total alteration $\Delta\chi_{LCO}$ of $2.5{\times}10^{-4}$ emu/(mol Oe) in this linear range, assuming that the small contribution of the localized moments (Langevin behavior) on χ_{LCO} is the same as determined for $x \leq 0.71$ (see below). This value of $D(E_F)$ is higher than the value calculated by ab-initio electronic band structure calculations lying in the range of $4.5\,eV^{-1}$ [226], indicating that the χ_P-variation cannot entirely be attributed to a rise of $D(E_F)$. In fact, an Anderson-type nonmetal-metal transition in this regime (see below) contributes to a χ_P-enhancement due to correlation effects [227].

In a next step, this strong linear variation of χ_{LCO} with the Li-ion concentration x is compared with that of the electrical conductivity. Since the $\chi_{LCO} - x$ variation is predominantly caused by a variation of the Pauli paramagnetism, the instant increase of χ_{LCO} with charging suggests that $LiCoO_2$ becomes metallic right after starting the Li extraction. This is also consistent with the calculations of Milewska et al. [226] according to which $D(E_F) > 0$ prevails already for $Li_{0.99}CoO_2$. Compared to that, however, conductivity measurements indicate a nonmetal-metal transition for $x = 0.94$. The nature of this nonmetal-metal transition is still under discussion [226, 228]. The different behavior of the conductivity and the magnetic susceptibility is well reconcilable with the interpretation of the transition being of Anderson-type [226], which affects conductivity and susceptibility in a different

manner. Due to the Anderson transition, electron holes are localized, which suppresses electron mobility for $x > 0.94$. Whereas this localization leads to a jump in conductivity at the nonmetal-metal transition, the Pauli susceptibility shows a continuous behavior (see Mott [227]) in full agreement with the present results. Indications of such an Anderson localization in Li_xCoO_2 were also observed by STM measurements [229]. For $La_{0.3}CoO_2$, where the low conductivity was attributed to this kind of localization, Pauli paramagnetism occurs [230] as well.

6.5.2 Li_xCoO_2 concentration range: $x \leq 0.77$

This subsection addresses the regime of $x \leq 0.77$, in which the increase of χ_{LCO} with decreasing Li-ion content x is reduced considerably (see Fig. 6.9). As shown by the temperature-dependent ex-situ measurements presented in Fig. 6.5 and by several other ex-situ studies [204, 206, 207], the temperature-independent susceptibility χ_0 becomes nearly independent of x in this concentration range. At most, a tendency for a χ_0 reduction with Li extraction can be discerned from the ex-situ measurements (see Fig. 6.5). This leads to the conclusion that the $\chi_{LCO} - x$ variation for $x \leq 0.77$, which shows an increase with Li extraction (see Fig. 6.9), must be governed by the localized magnetic moments owing to the charging-induced change of the oxidation state of the Co-ions (i.e., by the variation of χ_L). However, the simple notion of a transition from Co^{3+} to Co^{4+} does not apply, since as outlined above this would be associated with a much stronger variation of χ_{LCO} (see calculated gray dashed line in Fig. 6.7). The reduced slope of χ_{LCO} indicates that the charge is compensated not only by the Co oxidation but rather by concomitant charge transfer with O. In fact, XANES [231] and XPS measurements [224] have shown that in addition to Co, also O undergoes partial oxidation during Li extraction. Fitting $\chi_{LCO} - x(t)$ linearly for $x \leq 0.71$ (see green dotted line in Fig. 6.7) according to a Langevin-type behavior, yields a slope of $s_{fit} = 1.77 \times 10^{-9}$ emu/(mol Oe s), which corresponds to an effective magnetic moment of $0.55\,\mu_B$ per reacting Co-ion according to equations (6.3)–(6.7). This value is well in line with ex-situ data [203, 206] which supports the notion that the $\chi_{LCO} - x$ variation in this regime is governed by a change of the Co oxidation state. Since the transition Co^{3+} to Co^{4+} corresponds to a magnetic moment change of $1.73\,\mu_B$, an effective concentration of transformed Co of 32 % is derived from the effective magnetic moment of $0.55\,\mu_B$, which is in excellent agreement with ab-initio calculations according to which 35 % of charge is transferred to Co [232]. This demonstrates that the in-operando magnetometry measurements can monitor sensitively the oxidation state of the transition metal ions in the cathode

material during charging/discharging.

Remarkable is the fact that the increase of χ_{LCO} proceeds at the beginning of the discharging process (see $t = 8.8\,\mathrm{h}$ in Fig. 6.7, and regime of reversal on right-hand side in Fig. 6.9). This may indicate that parts of the Co-ions are reduced to an oxidation state having a high-spin configuration. Indeed it was concluded by XPS measurements, that Co^{2+} in the high-spin state is formed during reduction, due to oxygen deficiency at the electrode surface [233]. This formation of Co^{2+} would also be in line with the observed decrease of charging times from cycle to cycle (see Table 6.1). Since no indication for an oxidation of Co^{2+} back to Co^{3+} is found in the second charging cycle, which would be manifested by a decrease of χ_{LCO} in the charging cycle, it can be assumed that the formation of Co^{2+} is irreversible and, therefore, leads to performance losses (i.e., reduced charging capacity) in the next cycle. As can be seen in Fig. 6.7 and Table 6.1, both the rise of χ_{LCO} at the beginning of the discharging cycle, indicating the formation of Co^{2+}, and the performance losses become less pronounced with ongoing cycling, which shows that these two effects are correlated. To clarify this item and to check whether the formation of Co^{2+} is kinetically controlled, further measurements with different charging rates, cut-off and holding potentials are needed. The present measurements, however, already show that the in-operando technique gives access to such kind of phenomena, which may cause a deterioration of the cathode performance.

6.6 Conclusion and outlook

A technique for in-operando measurements of the magnetic susceptibility during electrochemical charging was implemented which enables in-operando studies of application-relevant battery materials even if they are not ferromagnetic. This is possible owing to the strongly reduced background signal of the cell. As a case study, charging and discharging of a commercially used paramagnetic Li_xCoO_2 cathode was monitored during consecutive cycles. The magnetic susceptibility of this cathode material varies by more than 150 % upon charging/discharging and, therefore, serves as highly sensitive fingerprint for the charge state. The continuous monitoring of χ_{LCO} allows a clear distinction between different magnetic behavior for various lithium contents x, yielding new insights into the electronic and chemical processes in the electrode during charging and discharging. In particular, the χ_{LCO} variation with Li content yields evidence for a nonmetal-metal transition of Anderson-type and for a charge compensation where in addition to Co oxidation also a charge transfer with O is involved.

As already stated above, further measurements on Li_xCoO_2 with different charging rates could be used to clarify if occurring phenomena, like the formation of Co^{2+}, are kinetically controlled. The kinetics of the ongoing processes could be further studied by holding of the charging/discharging process at a certain potential, while monitoring whether the χ_{LCO} variation continues or χ_{LCO} stays constant. Moreover, measurements with different upper cut-off potentials seem to be promising. On the one hand, by lowering the upper cut-off potential stepwise from 4.2 V, one can study up to which cut-off potential the χ_{LCO} variation shows an instant change in sign when starting the discharging cycle. These measurements would reveal the critical potential, above which the proposed irreversible formation of Co^{2+} in the discharging cycle occurs. On the other hand, the electronic and chemical processes going on when crossing the limit of reversible charging ($x = 0.5$) could be studied by increasing the upper cut-off potential from 4.2 V onwards. As can be seen from the ex-situ measurements (see Fig. 6.5), χ_L shows a strong decrease in the vicinity of the limit of reversible charging, indicating that an electronic charge transfer from O-ions to Co-ions occurs in the wake of loss of oxygen. Due to the possibility of the in-operando measurements to monitor χ_{LCO} continuously, such measurements could reveal if this decrease of χ_L occurs in a discrete step or continuously over a certain Li concentration range. This would shed new light on the electronic and chemical processes occurring at the limit of reversible charging.

Beside these additional measurements on Li_xCoO_2, the application of the presented in-operando technique to other cathode materials promises interesting results. For instance, studies on $LiFePO_4$ cathodes would be of high relevance, since the application of this material in e.g. batteries for electric vehicles is limited by the fact that the flat potential profile during charging/discharging hampers the determination of the state of charge [217]. Therefore, several research groups proposed to use the magnetic susceptibility of the $LiFePO_4$ cathode as an alternative quantity for the state of charge determination [234–236]. However, so far it has not been investigated whether the magnetic susceptibility of $LiFePO_4$ varies continuously in a systematic and reversible way over various cycles of charging/discharging. This would be the imperative prerequisite for such a detection method. The present in-operando technique represents the ideal tool to clarify if this is the case.

The layered mixed transition metal oxides, especially the so-called NMC materials, which contain nickel, manganese and cobalt ions ($Li_xCo_yNi_zMn_{1-y-z}O_2$) and which are beginning to be deployed in electric vehicles [219] are a further class of cathode materials, where novel insights into the chemical processes can be expected from in-operando studies of the mag-

netic susceptibility. In general, it is assumed that the transition metal ions in these materials are oxidized in sequence of $Ni^{2+} \rightarrow Ni^{3+}$, $Ni^{3+} \rightarrow Ni^{4+}$, $Co^{3+} \rightarrow Co^{4+}$ during charging, and that the Mn^{4+} stays unchanged [237]. Since the various transition metal ions exhibit different spin states, distinct variations of the Langevin susceptibility χ_L of these paramagnetic centers are expected for these different transitions. Since ex-situ measurements showed that NMC cathodes exhibit only this Langevin paramagnetism and no T-independent paramagnetism χ_0 [238–240], in-operando SQUID measurements would be an ideal technique to directly monitor these changes of the oxidation states of the transition metal ions continuously over several cycles of charging and discharging. Indeed, in preliminary measurements on $Li_xCo_{1/3}Ni_{1/3}Mn_{1/3}O_2$ cathodes, we could show that with Li de-/intercalation, different reversible ($Ni^{2+} \rightarrow Ni^{3+}$, $Ni^{3+} \rightarrow Ni^{4+}$) and irreversible ($Co^{3+} \rightarrow Co^{4+}$) oxidation processes can be unambiguously detected and analyzed.

CHAPTER 7

Summary and conclusion

In summary, a novel electrochemical cell design for in-situ studies in a state-of-the-art SQUID magnetometer was developed. The main improvements of this design are the reduced magnetic background signal and the implementation of a third electrode. Owing to the reduced background signal of the cell, measurements on paramagnetic samples and ultrathin magnetic films became feasible. Regarding thin films, the implemented technique of in-situ electrodeposition enables, furthermore, a total elimination of the magnetic background signal of the substrate and, therefore, allows a precise determination of the absolute magnetic moment arising exclusively from the electrodeposited film. Owing to the implementation of the third electrode, reliable in-situ cyclic voltammetry measurements and, therefore, a continuous monitoring of the magnetic properties during electrochemical characterization measurements became possible. In this way, a precise correlation between the electrochemical processes occurring on the investigated electrode and the detected variations of the magnetic properties could be accomplished. This was demonstrated based on three different topics.

At first, in-situ electrodeposition of thin Co films on a Au(111) substrate was addressed (Chapter 4). The emergence and decreasing of magnetism with Co deposition/dissolution could be observed by monitoring the magnetic moment m_{film} of the film continuously during its growth and subsequent dissolution. Since our method of in-situ electrodeposition enables to determine both the film thickness and the absolute magnetic moment of the ultrathin film, the thickness-dependence of the magnetic moment of the deposited Co films for film thicknesses between one and some tens of atomic layers could be studied. For the

first few atomic layers, an enhancement of the magnetic moment per Co atom compared to the bulk could be observed, which increases steadily with lowering the film thickness, and reaches up to 40 % for a film thickness of one atomic layer. Such an enhancement of the magnetic moment for ultrathin Co films is consistent with data in literature. Therefore, it was demonstrated that the presented approach of in-situ electrodeposition in a SQUID magnetometer is a promising new method for the determination of the absolute magnetic moment of ultrathin magnetic films.

Furthermore, the novel cell design was applied for studies of the electrochemical tuning of the magnetic properties of porous nanophase systems (Chapter 5). In this case, the ability to monitor the magnetic moment continuously during cyclic voltammetry measurements was utilized to distinguish which electrochemical process at the electrode-electrolyte interface causes the variation of the magnetic moment m. For porous nanophase Pt, the reversible variation of the magnetic moment during electrooxidation of up to 1 % turned out to be mainly caused by the electric field, which is generated by the electrochemical double layer at the Pt-electrolyte interface. Electric field-dependent spin-orbit coupling was identified as one possible origin of this m-variation. In contrast to the magnetic moment, the electrical resistance of the Pt sample is mainly influenced by the reversible oxygen adsorption/desorption processes at the Pt surface. The in-situ cyclic voltammetry measurements on a γ-Fe_2O_3/Pt nanocomposite showed that the charging-induced variation of the magnetic moment of the γ-Fe_2O_3 nanocrystallites of up to 4.9 % strongly depends on the potential regime of charging and, thereby demonstrates the ability of the novel measurement set-up to allocate the m-variation to a distinct electrochemical regime. In the positive potential regime, the charging-induced m-variation is suppressed due to the formation of a hydroxyl adsorption layer. The pronounced sensitivity of the magnetic moment to charging in the negative potential regime is most probably associated with a pseudocapacitive reversible redox reaction between γ-Fe_2O_3 and Fe_3O_4. However, it cannot be excluded that the magnetic moment is also influenced by charging-induced variations of the magnetic anisotropy or by a combined effect of charging-induced strain and magnetoelastic coupling.

Finally, the first in-operando measurements of the magnetic susceptibility of commercially used Li-ion battery cathode materials could be performed by means of the novel cell design (Chapter 6). As a case study, the magnetic susceptibility χ_{LCO} of Li_xCoO_2 cathodes was monitored during consecutive cycles of charging and discharging. It was demonstrated that the distinct variation of χ_{LCO} with Li content x can be used to give insights into the

chemical and electronic processes occurring in the cathode during charging and discharging. In particular, the linear variation of χ_{LCO} for lithium contents $1 > x \geq 0.77$ indicates a linear rise of the density of states at the Fermi-level $D(E_F)$ with Li extraction. For $x < 0.77$, the variation of χ_{LCO} was assigned to alterations of the Co oxidation state, revealing that in addition to cobalt also oxygen undergoes partial oxidation during charging. An observed further increase of χ_{LCO} at the beginning of the discharging process may indicate the formation of Co^{2+} during reduction.

In conclusion, it was demonstrated that the novel electrochemical cell design enables reliable electrochemical characterization measurements in-situ in a SQUID magnetometer and, that it is therefore highly suitable for studies of the correlations between electrochemical processes and magnetic properties in different kinds of fields, such as electrodeposition, electrochemical tuning of magnetic properties and as a diagnostic tool to characterize electronic and chemical processes occurring in Li-ion battery cathodes during charging and discharging. Therefore, this combination of SQUID magnetometry and in-situ electrochemical experiments promises to be a key to better understand the interdisciplinary field between magnetism and electrochemistry.

Bibliography

[1] J. M. D. Coey. *Magnetoelectrochemistry.* Europhys. News **34** (2003) 246.
DOI: 10.1051/epn:2003615

[2] A. Alemany, J.-P. Chopart. *An Outline of Magnetoelectrochemistry*, in *Magnetohydrodynamics* (edited by S. Molokov, R. Moreau, K. Moffatt), pp. 391–407. Springer, 2007.
DOI: 10.1007/978-1-4020-4833-3_24

[3] W. Schwarzacher, K. Attenborough, A. Michel, G. Nabiyouni, J. Meier. *Electrodeposited nanostructures.* J. Magn. Magn. Mater. **165** (1997) 23.
DOI: 10.1016/S0304-8853(96)00465-9

[4] W. Schindler, J. Kirschner. *Ultrathin magnetic films: Electrochemistry versus molecular-beam epitaxy.* Phys. Rev. B **55** (1997) R1989.
DOI: 10.1103/PhysRevB.55.R1989

[5] P. Allongue, F. Maroun, H. F. Jurca, N. Tournerie, G. Savidand, R. Cortès. *Magnetism of electrodeposited ultrathin layers: Challenges and opportunities.* Surf. Sci. **603** (2009) 1831.
DOI: 10.1016/j.susc.2008.11.040

[6] I. W. Wolf. *Composition and Thickness Effects on Magnetic Properties of Electrodeposited Nickel-Iron Thin Films.* J. Electrochem. Soc. **108** (1961) 959.
DOI: 10.1149/1.2427928

[7] C. Cheung, F. Djuanda, U. Erb, G. Palumbo. *Electrodeposition of nanocrystalline Ni-Fe alloys.* Nanostruct. Mater. **5** (1995) 513.
DOI: 10.1016/0965-9773(95)00264-F

[8] F. Rhen, G. Hinds, C. O'Reilly, J. Coey. *Electrodeposited FePt films.* IEEE Trans. Magn. **39** (2003) 2699.
DOI: 10.1109/TMAG.2003.815566

[9] K. Leistner, J. Thomas, H. Schlörb, M. Weisheit, L. Schultz, S. Fähler. *Highly coercive electrodeposited FePt films by postannealing in hydrogen.* Appl. Phys. Lett. **85** (2004) 3498.
DOI: 10.1063/1.1807958

[10] M. Dariel, L. H. Bennett, D. S. Lashmore, P. Lubitz, M. Rubinstein, W. L. Lechter, M. Z. Harford. *Properties of electrodeposited Co-Cu multilayer structures.* J. Appl. Phys. **61** (1987) 4067.
DOI: 10.1063/1.338529

[11] L. Péter, A. Cziráki, L. Pogány, Z. Kupay, I. Bakonyi, M. Uhlemann, M. Herrich, B. Arnold, T. Bauer, K. Wetzig. *Microstructure and Giant Magnetoresistance of Electrodeposited Co-Cu/Cu Multilayers.* J. Electrochem. Soc. **148** (2001) C168.
DOI: 10.1149/1.1346606

[12] K. Leistner, S. Fähler, H. Schlörb, L. Schultz. *Preparation and characterization of electrodeposited Fe/Pt multilayers.* Electrochem. Commun. **8** (2006) 916.
DOI: 10.1016/j.elecom.2006.03.032

[13] H. Schlörb, V. Haehnel, M. S. Khatri, A. Srivastav, A. Kumar, L. Schultz, S. Fähler. *Magnetic nanowires by electrodeposition within templates.* Phys. Status Solidi B **247** (2010) 2364.
DOI: 10.1002/pssb.201046189

[14] C. T. Sousa, D. C. Leitao, M. P. Proenca, J. Ventura, A. M. Pereira, J. P. Araujo. *Nanoporous alumina as templates for multifunctional applications.* Appl. Phys. Rev. **1** (2014) 031102.
DOI: 10.1063/1.4893546

[15] C. Lemier, S. Ghosh, R. N. Viswanath, G.-T. Fei, J. Weissmüller. *Charge induced Variation of the Magnetization in Nanoporous Ni-Pd.* MRS Proceedings **876** (2005) R2.6.
DOI: 10.1557/PROC-876-R2.6

[16] S. Ghosh, C. Lemier, J. Weissmüller. *Charge-dependent magnetization in nanoporous Pd-Co alloys.* IEEE Trans. Magn. **42** (2006) 3617.
DOI: 10.1109/TMAG.2006.880922

[17] H. Drings, R. N. Viswanath, D. Kramer, C. Lemier, J. Weissmüller, R. Würschum. *Tuneable magnetic susceptibility of nanocrystalline palladium.* Appl. Phys. Lett. **88** (2006) 253103.
DOI: 10.1063/1.2216897

[18] T. Traussnig, S. Topolovec, K. Nadeem, D. V. Szabó, H. Krenn, R. Würschum. *Magnetization of Fe-oxide based nanocomposite tuned by surface charging.* Phys. Status Solidi RRL **5** (2011) 150.
DOI: 10.1002/pssr.201004483

[19] M. Weisheit, S. Fähler, A. Marty, Y. Souche, C. Poinsignon, D. Givord. *Electric Field-Induced Modification of Magnetism in Thin-Film Ferromagnets.* Science **315** (2007) 349.
DOI: 10.1126/science.1136629

[20] N. Hiraoka, Y. Oba, T. Watanabe, H. Maki, Y. Einaga, T. Sato. *Redox-Induced Modification of Magnetism in Ni Thin Film.* e-J. Surf. Sci. Nanotechnol. **7** (2009) 787.
DOI: 10.1380/ejssnt.2009.787

[21] K. Leistner, N. Lange, J. Hänisch, S. Oswald, F. Scheiba, S. Fähler, H. Schlörb, L. Schultz. *Electrode processes and in situ magnetic measurements of FePt films in a $LiPF_6$ based electrolyte.* Electrochim. Acta **81** (2012) 330.
DOI: 10.1016/j.electacta.2012.07.055

[22] N. Tournerie, A. P. Engelhardt, F. Maroun, P. Allongue. *Influence of the surface chemistry on the electric-field control of the magnetization of ultrathin films.* Phys. Rev. B **86** (2012) 104434.
DOI: 10.1103/PhysRevB.86.104434

[23] K. Leistner, N. Lange, S. Oswald, L. Schultz. *Reversible Change of Magnetism in FePt Films by Electrochemical Charging in a $LiClO_4$ Based Electrolyte.* ECS Trans. **50** (2013) 49.
DOI: 10.1149/05010.0049ecst

[24] T. Traussnig. *Charge-induced property tuning of nanoscaled metals and metal oxides.* PhD thesis, Institute of Materials Physics, Graz University of Technology, 2011.

[25] W. Schindler, J. Kirschner. *New electrochemical cell for in situ tunneling microscopy, cyclovoltammetry, and optical measurements.* Rev. Sci. Instrum. **67** (1996) 3578.
DOI: 10.1063/1.1147176

[26] W. Schindler, O. Schneider, J. Kirschner. *Electrodeposition of ultrathin magnetic films of Fe and Co.* J. Appl. Phys. **81** (1997) 3915.
DOI: 10.1063/1.364701

[27] K. M. Poduska, S. Morin. *Electrochemical cell for in situ magneto-optic Kerr effect measurements.* Rev. Sci. Instrum. **74** (2003) 4723.
DOI: 10.1063/1.1619583

[28] W. Schindler. *Electrodeposited Magnetic Monolayers: In-Situ Studies of Magnetism and Structure*, in *Solid-Liquid Interfaces*, Vol. 85 of *Topics in Applied Physics* (edited by K. Wandelt, S. Thurgate), pp. 243–259. Springer, 2003.
DOI: 10.1007/3-540-44817-9_8

[29] A. Gündel, T. Devolder, C. Chappert, J. Schmidt, R. Cortes, P. Allongue. *Electrodeposition of Fe/Au(111) ultrathin layers with perpendicular magnetic anisotropy.* Phys. B **354** (2004) 282.
DOI: 10.1016/j.physb.2004.09.068

[30] P. Allongue, F. Maroun. *Metal electrodeposition on single crystal metal surfaces mechanisms, structure and applications.* Curr. Opin. Solid State Mater. Sci. **10** (2006) 173.
DOI: 10.1016/j.cossms.2007.04.001

[31] T. Mangen, H. Bai, J. Tsay. *Structures and magnetic properties for electrodeposited Co ultrathin films on copper.* J. Magn. Magn. Mater. **322** (2010) 1863.
DOI: 10.1016/j.jmmm.2009.12.042

[32] C.-L. Lin, A.-W. Wu, Y.-C. Wang, Y.-C. Tseng, J.-S. Tsay. *Spin reorientation transitions and structures of electrodeposited Ni/Cu(100) ultrathin films with and without Pb additives.* Phys. Chem. Chem. Phys. **15** (2013) 2360.
DOI: 10.1039/C2CP42833D

[33] N. Tournerie, A. Engelhardt, F. Maroun, P. Allongue. *Probing the electrochemical interface with in situ magnetic characterizations: A case study of Co/Au(111) layers.* Surf. Sci. **631** (2015) 88.
DOI: 10.1016/j.susc.2014.06.023

[34] L. Cagnon, A. Gündel, T. Devolder, A. Morrone, C. Chappert, J. Schmidt, P. Allongue. *Anion effect in Co/Au(111) electrodeposition: structure and magnetic behavior.* Appl. Surf. Sci. **164** (2000) 22.
DOI: 10.1016/S0169-4332(00)00330-5

[35] A. Gündel, L. Cagnon, C. Gomes, A. Morrone, J. Schmidt, P. Allongue. *In-situ magnetic measurements of electrodeposited ultrathin Co, Ni and Fe/Au(111) layers.* Phys. Chem. Chem. Phys. **3** (2001) 3330.
DOI: 10.1039/B100547M

[36] A. Gündel, E. Chassaing, J. E. Schmidt. *In-situ magnetization measurements of Cu/Co multilayers during the process of electrodeposition.* J. Appl. Phys. **90** (2001) 5257.
DOI: 10.1063/1.1413233

[37] A. Gündel, A. Morrone, J. Schmidt, L. Cagnon, P. Allongue. *Magnetic properties of electrodeposited Fe/Au(111) layers: in situ AGFM measurements.* J. Magn. Magn. Mater. **226** (2001) 1616.
DOI: 10.1016/S0304-8853(00)01039-8

[38] J. Geshev, A. Gündel, I. Zaharieva, J. E. Schmidt. *Edge atoms effects on the perpendicular anisotropy of ultrathin magnetic layers.* Appl. Phys. Lett. **101** (2012) 132407.
DOI: 10.1063/1.4754621

[39] D. Spoddig, R. Meckenstock, J. Bucher, J. Pelzl. *Studies of ferromagnetic resonance line width during electrochemical deposition of Co films on Au(111).* J. Magn. Magn. Mater. **286** (2005) 286.
DOI: 10.1016/j.jmmm.2004.09.082

[40] H. Gleiter, J. Weissmüller, O. Wollersheim, R. Würschum. *Nanocrystalline materials: a way to solids with tunable electronic structures and properties?* Acta Mater. **49** (2001) 737.
DOI: 10.1016/S1359-6454(00)00221-4

[41] M. Zhernenkov, M. R. Fitzsimmons, J. Chlistunoff, J. Majewski, I. Tudosa, E. E. Fullerton. *Electric-field modification of magnetism in a thin CoPd film.* Phys. Rev. B **82** (2010) 024420.
DOI: 10.1103/PhysRevB.82.024420

[42] N. A. Chernova, G. M. Nolis, F. O. Omenya, H. Zhou, Z. Li, M. S. Whittingham. *What can we learn about battery materials from their magnetic properties?* J. Mater. Chem. **21** (2011) 9865.
DOI: 10.1039/C1JM00024A

[43] S. Topolovec, P. Jerabek, D. V. Szabó, H. Krenn, R. Würschum. *SQUID magnetometry combined with in situ cyclic voltammetry: A case study of tunable magnetism of γ-Fe_2O_3 nanoparticles.* J. Magn. Magn. Mater. **329** (2013) 43.
DOI: 10.1016/j.jmmm.2012.09.071

[44] E.-M. Steyskal, S. Topolovec, S. Landgraf, H. Krenn, R. Würschum. *In situ monitoring magnetism and resistance of nanophase platinum upon electrochemical oxidation.* Beilstein J. Nanotech. **4** (2013) 394.
DOI: 10.3762/bjnano.4.46

[45] S. Topolovec, H. Krenn, R. Würschum. *Electrochemical cell for in situ electrodeposition of magnetic thin films in a superconducting quantum interference device magnetometer.* Rev. Sci. Instrum. **86** (2015) 063903.
DOI: 10.1063/1.4922462

[46] S. Topolovec, H. Krenn, R. Würschum. *Enhanced magnetic moment of ultrathin Co films measured by in situ electrodeposition in a SQUID.* J. Magn. Magn. Mater. **397** (2016) 96.
DOI: 10.1016/j.jmmm.2015.08.088

[47] S. Topolovec, H. Kren, G. Klinser, S. Koller, H. Krenn, R. Würschum. *In-operando SQUID magnetometry on Li_xCoO_2 during charging/discharging.* Submitted for pubilcation.

[48] Y. D. Gamburg, G. Zangari. *Theory and Practice of Metal Electrodeposition.* Springer, 2011.
DOI: 10.1007/978-1-4419-9669-5

[49] J. S. Blakemore. *Solid State Physics.* Cambridge University Press, 1985.
DOI: 10.1017/CBO9781139167871

[50] C. H. Hamann, W. Vielstich. *Elektrochemie.* Wiley-VCH, 4. edition, 2005.

[51] P. Kornyshev, E. Spohr, M. Vorotynstev. *Electrochemical Interfaces: At the Border Line*, in *Encyclopedia of Electrochemistry*, Vol. 1: Thermodynamics and Electrified Interfaces (edited by A. Bard, M. Stratmann, E. Gileadi, M. Urbakh), pp. 33–132. Wiley-VCH, 2003.
DOI: 10.1002/9783527610426.bard010201

[52] E. Gileadi. *Electrode Kinetics for Chemists, Chemical Engineers and Materials Scientists.* Wiley-VCH, 1993.

[53] W. Schmickler. *Grundlagen der Elektrochemie.* Vieweg, 1996.

[54] N. Kanani. *Electroplating - Basic Principles, Processes and Practice.* Elsevier, 2004.

[55] P. Unwin. *Introduction to Electroanalytical Techniques and Instrumentation*, in *Encyclopedia of Electrochemistry*, Vol. 3: Instrumentation and Electroanalytical Chemistry (edited by A. Bard, M. Stratmann, P. Unwin), pp. 3–23. Wiley-VCH, 2003.
DOI: 10.1002/9783527610426.bard030101

[56] S. Chen. *Practical Electrochemical Cells*, in *Handbook of Electrochemistry* (edited by C. G. Zoski), pp. 33–56. Elsevier, 2007.
DOI: 10.1016/B978-044451958-0.50003-3

[57] R. G. Compton, C. E. Banks. *Understanding voltammetry.* Imperial College Press, 2. edition, 2011.
DOI: 10.1142/9781848165878_fmatter

[58] G. Denuault, M. Sosna, K.-J. Williams. *Classical Experiments*, in *Handbook of Electrochemistry* (edited by C. G. Zoski), pp. 431–469. Elsevier, 2007.
DOI: 10.1016/B978-044451958-0.50024-0

[59] H. Angerstein-Kozlowska, B. Conway, W. Sharp. *The real condition of electrochemically oxidized platinum surfaces: Part I. Resolution of component processes.* J. Electroanal. Chem. **43** (1973) 9.
DOI: 10.1016/S0022-0728(73)80307-9

[60] B. Conway. *Electrochemical oxide film formation at noble metals as a surface-chemical process.* Prog. Surf. Sci. **49** (1995) 331.
DOI: 10.1016/0079-6816(95)00040-6

[61] G. Jerkiewicz, G. Vatankhah, J. Lessard, M. P. Soriaga, Y.-S. Park. *Surface-oxide growth at platinum electrodes in aqueous H_2SO_4: Reexamination of its mechanism through combined cyclic-voltammetry, electrochemical quartz-crystal nanobalance, and Auger electron spectroscopy measurements.* Electrochim. Acta **49** (2004) 1451.
DOI: 10.1016/j.electacta.2003.11.008

[62] R. C. Black, F. C. Wellstood. *Measurements of Magnetism and Magnetic Properties of Matter*, in *The SQUID Handbook Vol II: Applications of SQUIDs and SQUID Systems* (edited by J. Clarke, A. I. Braginski). Wiley-VCH, 2006.
DOI: 10.1002/9783527609956

[63] Quantum Design, Inc. *MPMS Application Note 1014-213.* San Diego, 2002.

[64] Quantum Design, Inc. *MPMS Application Note 1014-201.* San Diego, 2000.

[65] C. A. F. Vaz, J. A. C. Bland, G. Lauhoff. *Magnetism in ultrathin film structures.* Rep. Prog. Phys. **71** (2008) 056501.
DOI: 10.1088/0034-4885/71/5/056501

[66] Y. Shiratsuchi, M. Yamamoto, S. Bader. *Magnetism and surface structure of atomically controlled ultrathin metal films.* Progr. Surf. Sci. **82** (2007) 121.
DOI: 10.1016/j.progsurf.2006.08.001

[67] A. Ney, T. Kammermeier, V. Ney, K. Ollefs, S. Ye. *Limitations of measuring small magnetic signals of samples deposited on a diamagnetic substrate.* J. Magn. Magn. Mater. **320** (2008) 3341.
DOI: 10.1016/j.jmmm.2008.07.008

[68] M. Sawicki, W. Stefanowicz, A. Ney. *Sensitive SQUID magnetometry for studying nanomagnetism.* Semicond. Sci. Technol. **26** (2011) 064006.
DOI: 10.1088/0268-1242/26/6/064006

[69] B. Heinrich, J. F. Cochran. *Magnetic Ultrathin Films*, in *Handbook of Magnetism and Advanced Magnetic Materials*, Vol. 4 (edited by H. Kronmüller, S. Parkin), pp. 2285–2305. John Wiley & Sons, 2007.
DOI: 10.1002/9780470022184.hmm420

[70] E. Manios, D. Stamopoulos, N. Moutis, M. Pissas, D. Niarchos. *Magnetic measurements in thin film specimens: Rejecting the contribution of the substrate.* J. Magn. Magn. Mater. **320** (2008) 3264.
DOI: 10.1016/j.jmmm.2008.06.020

[71] Quantum Design, Inc. *MPMS MultiVu Application User's Manual.* San Diego, 2004.

[72] C. Q. Cui, S. P. Jiang, A. C. C. Tseung. *Electrodeposition of Cobalt from Aqueous Chloride Solutions.* J. Electrochem. Soc. **137** (1990) 3418.
DOI: 10.1149/1.2086232

[73] M. Kleinert, H.-F. Waibel, G. Engelmann, H. Martin, D. Kolb. *Co deposition on Au(111) and Au(100) electrodes: an in situ STM study.* Electrochim. Acta **46** (2001) 3129.
DOI: 10.1016/S0013-4686(01)00604-1

[74] M. B. Stearns. *Magnetic Properties of Metals*, in *Landolt-Börnstein - Group III Condensed Matter*, Vol. 19a (edited by H. P. J. Wijn), p. 37. Springer, 1986.
DOI: 10.1007/10311893_7

[75] J. Bubendorff, C. Mény, E. Beaurepaire, P. Panissod, J. Bucher. *Electrodeposited cobalt films: hcp versus fcc nanostructuring and magnetic properties.* Eur. Phys. J. B **17** (2000) 635.
DOI: 10.1007/s100510070102

[76] A. Ney, P. Poulopoulos, M. Farle, K. Baberschke. *Absolute determination of Co magnetic moments: Ultrahigh-vacuum high-T_c SQUID magnetometry.* Phys. Rev. B **62** (2000) 11336.
DOI: 10.1103/PhysRevB.62.11336

[77] G. H. O. Daalderop, P. J. Kelly, M. F. H. Schuurmans. *Magnetic anisotropy of a free-standing Co monolayer and of multilayers which contain Co monolayers.* Phys. Rev. B **50** (1994) 9989.
DOI: 10.1103/PhysRevB.50.9989

[78] O. Hjortstam, J. Trygg, J. M. Wills, B. Johansson, O. Eriksson. *Calculated spin and orbital moments in the surfaces of the 3d metals Fe, Co, and Ni and their overlayers on Cu(001).* Phys. Rev. B **53** (1996) 9204.
DOI: 10.1103/PhysRevB.53.9204

[79] J. L. Rodríguez-López, J. Dorantes-Dávila, G. M. Pastor. *Orbital magnetism at the surfaces of 3d transition metals.* Phys. Rev. B **57** (1998) 1040.
DOI: 10.1103/PhysRevB.57.1040

[80] A. B. Shick, A. J. Freeman, A. I. Liechtenstein. *Orbital magnetic moment enhancement at surfaces and interfaces within the framework of the local density approximation+U method.* J. Appl. Phys. **83** (1998) 7022.
DOI: 10.1063/1.367723

[81] O. Šipr, S. Bornemann, H. Ebert, J. Minár. *Magnetocrystalline anisotropy energy for adatoms and monolayers on non-magnetic substrates: where does it come from?* J. Phys.: Condens. Matter **26** (2014) 196002.
DOI: 10.1088/0953-8984/26/19/196002

[82] M. Tischer, O. Hjortstam, D. Arvanitis, J. Hunter Dunn, F. May, K. Baberschke, J. Trygg, J. M. Wills, B. Johansson, O. Eriksson. *Enhancement of Orbital Magnetism at Surfaces: Co on Cu(100).* Phys. Rev. Lett. **75** (1995) 1602.
DOI: 10.1103/PhysRevLett.75.1602

[83] P. Srivastava, F. Wilhelm, A. Ney, M. Farle, H. Wende, N. Haack, G. Ceballos, K. Baberschke. *Magnetic moments and Curie temperatures of Ni and Co thin films and coupled trilayers.* Phys. Rev. B **58** (1998) 5701.
DOI: 10.1103/PhysRevB.58.5701

[84] J. A. C. Bland, A. D. Johnson, C. Norris, H. J. Lauter. *Absolute value of the magnetic moment per atom in Ag/Fe/Ag(001) and Ag/Co/Ag(001) epitaxial sandwich structures.* J. Appl. Phys. **67** (1990) 5397.
DOI: 10.1063/1.344565

[85] V. Pasyuk, H. Lauter, M. Johnson, F. den Broeder, E. Janssen, J. Bland, A. Petrenko. *Magnetic properties of a Pd/Co/Pd ultrathin film studied by polarized neutron specular reflection.* Appl. Surf. Sci. **65-66** (1993) 118.
DOI: 10.1016/0169-4332(93)90645-R

[86] A. Ney, P. Poulopoulos, K. Baberschke. *Surface and interface magnetic moments of Co/Cu(001).* Europhys. Lett. **54** (2001) 820.
DOI: 10.1209/epl/i2001-00327-4

[87] J. L. Bubendorff, E. Beaurepaire, C. Mény, J. P. Bucher. *Overpotential driven perpendicular magnetization of electrodeposited ultrathin cobalt films.* J. Appl. Phys. **83** (1998) 7043.
DOI: 10.1063/1.367820

[88] S. Padovani, F. Scheurer, J. P. Bucher. *Burrowing self-organized cobalt clusters into a gold substrate.* Europhys. Lett. **45** (1999) 327.
DOI: 10.1209/epl/i1999-00167-2

[89] F. Wilhelm, M. Angelakeris, N. Jaouen, P. Poulopoulos, E. T. Papaioannou, C. Mueller, P. Fumagalli, A. Rogalev, N. K. Flevaris. *Magnetic moment of Au at Au/Co interfaces: A direct experimental determination.* Phys. Rev. B **69** (2004) 220404.
DOI: 10.1103/PhysRevB.69.220404

[90] U. Bovensiepen, P. Poulopoulos, W. Platow, M. Farle, K. Baberschke. *Sudden jump of the Curie temperature at the coalescence of Co islands on Cu(001).* J. Magn. Magn. Mater. **192** (1999) L386.
DOI: 10.1016/S0304-8853(98)01091-9

[91] S. Padovani, I. Chado, F. Scheurer, J. P. Bucher. *Transition from zero-dimensional superparamagnetism to two-dimensional ferromagnetism of Co clusters on Au(111).* Phys. Rev. B **59** (1999) 11887.
DOI: 10.1103/PhysRevB.59.11887

[92] H. Takeshita, Y. Suzuki, H. Akinaga, W. Mizutani, K. Ando, T. Katayama, A. Itoh, K. Tanaka. *Magnetization process of a nanometer-scale cobalt dots array formed on a reconstructed Au(111) surface.* J. Magn. Magn. Mater. **165** (1997) 38.
DOI: 10.1016/S0304-8853(96)00468-4

[93] E. Dudzik, H. A. Dürr, S. S. Dhesi, G. van der Laan, D. Knabben, J. B. Goedkoop. *Magnetic properties of self-assembled Co clusters on Au(111) below the ferromagnetic phase transition.* J. Phys.: Condens. Matter **11** (1999) 8445.
DOI: 10.1088/0953-8984/11/43/307

[94] P. Poulopoulos, P. J. Jensen, A. Ney, J. Lindner, K. Baberschke. *Metastable magnetic properties of Co/Cu(001) films below the T_C jump.* Phys. Rev. B **65** (2002) 064431.
DOI: 10.1103/PhysRevB.65.064431

[95] M. Rastei, S. Colis, R. Meckenstock, O. Ersen, J. Bucher. *Pulsed electrodeposition and magnetism of two-dimensional assembly of controlled-size Co particles on Si substrates.* Surf. Sci. **600** (2006) 2178.
DOI: 10.1016/j.susc.2006.03.007

[96] F. Pagnanelli, P. Altimari, M. Bellagamba, G. Granata, E. Moscardini, P. G. Schiavi, L. Toro. *Pulsed electrodeposition of cobalt nanoparticles on copper: influence of the operating parameters on size distribution and morphology.* Electrochim. Acta **155** (2015) 228.
DOI: 10.1016/j.electacta.2014.12.112

[97] M. N. Baibich, J. M. Broto, A. Fert, F. N. Van Dau, F. Petroff, P. Etienne, G. Creuzet, A. Friederich, J. Chazelas. *Giant Magnetoresistance of (001)Fe/(001)Cr Magnetic Superlattices.* Phys. Rev. Lett. **61** (1988) 2472.
DOI: 10.1103/PhysRevLett.61.2472

[98] G. Binasch, P. Grünberg, F. Saurenbach, W. Zinn. *Enhanced magnetoresistance in layered magnetic structures with antiferromagnetic interlayer exchange.* Phys. Rev. B **39** (1989) 4828.
DOI: 10.1103/PhysRevB.39.4828

[99] M. Julliere. *Tunneling between ferromagnetic films.* Phys. Lett. A **54** (1975) 225.
DOI: 10.1016/0375-9601(75)90174-7

[100] T. Miyazaki, N. Tezuka. *Giant magnetic tunneling effect in Fe/Al_2O_3/Fe junction.* J. Magn. Magn. Mater. **139** (1995) L231.
DOI: 10.1016/0304-8853(95)90001-2

[101] J. S. Moodera, L. R. Kinder, T. M. Wong, R. Meservey. *Large Magnetoresistance at Room Temperature in Ferromagnetic Thin Film Tunnel Junctions.* Phys. Rev. Lett. **74** (1995) 3273.
DOI: 10.1103/PhysRevLett.74.3273

[102] S. Yuasa, T. Nagahama, A. Fukushima, Y. Suzuki, K. Ando. *Giant room-temperature magnetoresistance in single-crystal Fe/MgO/Fe magnetic tunnel junctions.* Nat. Mater. **3** (2004) 868.
DOI: 10.1038/nmat1257

[103] S. Parkin, C. Kaiser, A. Panchula, P. Rice, B. Hughes, M. Samant, S. Yang. *Giant tunnelling magnetoresistance at room temperature with MgO (100) tunnel barriers.* Nat. Mater. **3** (2004) 862.
DOI: 10.1038/nmat1256

[104] N. Honda, K. Yamakawa. *Write heads: Fundamentals*, in *Developments in data storage: materials perspective* (edited by S. Piramanayagam, T. C. Chong). John Wiley & Sons, 2011.
DOI: 10.1002/9781118096833.ch5

[105] J. Slonczewski. *Current-driven excitation of magnetic multilayers.* J. Magn. Magn. Mater. **159** (1996) L1.
DOI: 10.1016/0304-8853(96)00062-5

[106] L. Berger. *Emission of spin waves by a magnetic multilayer traversed by a current.* Phys. Rev. B **54** (1996) 9353.
DOI: 10.1103/PhysRevB.54.9353

[107] J. A. Katine, F. J. Albert, R. A. Buhrman, E. B. Myers, D. C. Ralph. *Current-Driven Magnetization Reversal and Spin-Wave Excitations in Co/Cu/Co Pillars.* Phys. Rev. Lett. **84** (2000) 3149.
DOI: 10.1103/PhysRevLett.84.3149

[108] Y. Huai, F. Albert, P. Nguyen, M. Pakala, T. Valet. *Observation of spin-transfer switching in deep submicron-sized and low-resistance magnetic tunnel junctions.* Appl. Phys. Lett. **84** (2004) 3118.
DOI: 10.1063/1.1707228

[109] M. Hosomi, H. Yamagishi, T. Yamamoto, K. Bessho, Y. Higo, K. Yamane, H. Yamada, M. Shoji, H. Hachino, C. Fukumoto, H. Nagao, H. Kano. *A novel nonvolatile memory with spin torque transfer magnetization switching: spin-ram*, in *Tech. Dig. - Int. Electron Devices Meet.*, pp. 459–462, 2005.
DOI: 10.1109/IEDM.2005.1609379

[110] C. Binek, B. Doudin. *Magnetoelectronics with magnetoelectrics.* J. Phys.: Condens. Matter **17** (2005) L39.
DOI: 10.1088/0953-8984/17/2/L06

[111] F. Matsukura, Y. Tokura, H. Ohno. *Control of magnetism by electric fields.* Nat. Nanotechnol. **10** (2015) 209.
DOI: 10.1038/NNANO.2015.22

[112] D. Chiba, T. Ono. *Control of magnetism in Co by an electric field.* J. Phys. D: Appl. Phys. **46** (2013) 213001.
DOI: 10.1088/0022-3727/46/21/213001

[113] O. O. Brovko, P. Ruiz-Díaz, T. R. Dasa, V. S. Stepanyuk. *Controlling magnetism on metal surfaces with non-magnetic means: electric fields and surface charging.* J. Phys.: Condens. Matter **26** (2014) 093001.
DOI: 10.1088/0953-8984/26/9/093001

[114] W. Eerenstein, N. D. Mathur, J. F. Scott. *Multiferroic and magnetoelectric materials.* Nature **442** (2006) 759.
DOI: 10.1038/nature05023

[115] Y.-H. Chu, L. W. Martin, M. B. Holcomb, M. Gajek, S.-J. Han, Q. He, N. Balke, C.-H. Yang, D. Lee, W. Hu, Q. Zhan, P.-L. Yang, A. Fraile-Rodriguez, A. Scholl, S. X. Wang, R. Ramesh. *Electric-field control of local ferromagnetism using a magnetoelectric multiferroic.* Nat. Mater. **7** (2008) 478.
DOI: 10.1038/nmat2184

[116] E. Y. Tsymbal. *Electric toggling of magnets.* Nat. Mater. **11** (2012) 12.
DOI: 10.1038/nmat3205

[117] H. Ohno, D. Chiba, F. Matsukura, T. Omiya, E. Abe, T. Dietl, Y. Ohno, K. Ohtani. *Electric-field control of ferromagnetism.* Nature **408** (2000) 944.
DOI: 10.1038/35050040

[118] D. Chiba, M. Yamanouchi, F. Matsukura, H. Ohno. *Electrical manipulation of magnetization reversal in a ferromagnetic semiconductor.* Science **301** (2003) 943.
DOI: 10.1126/science.1086608

[119] T. Maruyama, Y. Shiota, T. Nozaki, K. Ohta, N. Toda, M. Mizuguchi, A. A. Tulapurkar, T. Shinjo, M. Shiraishi, S. Mizukami, Y. Ando, Y. Suzuki. *Large voltage-induced magnetic anisotropy change in a few atomic layers of iron.* Nat. Nanotechnol. **4** (2009) 158.
DOI: 10.1038/NNANO.2008.406

[120] D. Chiba, S. Fukami, K. Shimamura, N. Ishiwata, K. Kobayashi, T. Ono. *Electrical control of the ferromagnetic phase transition in cobalt at room temperature.* Nat. Mater. **10** (2011) 853.
DOI: 10.1038/NMAT3130

[121] Y. Shiota, T. Nozaki, F. Bonell, S. Murakami, T. Shinjo, Y. Suzuki. *Induction of coherent magnetization switching in a few atomic layers of FeCo using voltage pulses.* Nat. Mater. **11** (2015) 13.
DOI: 10.1038/NMAT3172

[122] J. Weissmüller, R. N. Viswanath, D. Kramer, P. Zimmer, R. Würschum, H. Gleiter. *Charge-Induced Reversible Strain in a Metal.* Science **300** (2003) 312.
DOI: 10.1126/science.1081024

[123] R. N. Viswanath, D. Kramer, J. Weissmüller. *Adsorbate effects on the surface stress-charge response of platinum electrodes.* Electrochim. Acta **53** (2008) 2757.
DOI: 10.1016/j.electacta.2007.10.049

[124] H.-J. Jin, J. Weissmüller. *A Material with Electrically Tunable Strength and Flow Stress.* Science **332** (2011) 1179.
DOI: 10.1126/science.1202190

[125] E. Detsi, Z. G. Chen, W. P. Vellinga, P. R. Onck, J. T. M. De Hosson. *Reversible strain by physisorption in nanoporous gold.* Appl. Phys. Lett. **99** (2011) 083104.
DOI: 10.1063/1.3625926

[126] J. Biener, S. Dasgupta, L. Shao, D. Wang, M. A. Worsley, A. Wittstock, J. R. I. Lee, M. M. Biener, C. A. Orme, S. O. Kucheyev, B. C. Wood, T. M. Willey, A. V. Hamza, J. Weissmüller, H. Hahn, T. F. Baumann. *Macroscopic 3D Nanographene with Dynamically Tunable Bulk Properties.* Adv. Mater. **24** (2012) 5083.
DOI: 10.1002/adma.201202289

[127] N. Mameka, J. Markmann, H.-J. Jin, J. Weissmüller. *Electrical stiffness modulation – confirming the impact of surface excess elasticity on the mechanics of nanomaterials.* Acta Mater. **76** (2014) 272.
DOI: 10.1016/j.actamat.2014.04.067

[128] Y. Xue, J. Markmann, H. Duan, J. Weissmüller, P. Huber. *Switchable imbibition in nanoporous gold.* Nat. Commun. **5** (2014) 4237.
DOI: 10.1038/ncomms5237

[129] M. Sagmeister, U. Brossmann, S. Landgraf, R. Würschum. *Electrically Tunable Resistance of a Metal.* Phys. Rev. Lett. **96** (2006) 156601.
DOI: 10.1103/PhysRevLett.96.156601

[130] S. Dasgupta, S. Gottschalk, R. Kruk, H. Hahn. *A nanoparticulate indium tin oxide field-effect transistor with solid electrolyte gating.* Nanotechnology **19** (2008) 435203.
DOI: 10.1088/0957-4484/19/43/435203

[131] P. Wahl, T. Traussnig, S. Landgraf, H.-J. Jin, J. Weissmüller, R. Würschum. *Adsorption-driven tuning of the electrical resistance of nanoporous gold.* J. Appl. Phys. **108** (2010) 073706.
DOI: 10.1063/1.3490789

[132] A. K. Mishra, C. Bansal, M. Ghafari, R. Kruk, H. Hahn. *Tuning properties of nanoporous Au-Fe alloys by electrochemically induced surface charge variations.* Phys. Rev. B **81** (2010) 155452.
DOI: 10.1103/PhysRevB.81.155452

[133] E.-M. Steyskal, M. Besenhard, S. Landgraf, Y. Zhong, J. Weissmüller, P. Pölt, M. Albu, R. Würschum. *Sign-inversion of charging-induced variation of electrical resistance of nanoporous platinum.* J. Appl. Phys. **112** (2012) 073703.
DOI: 10.1063/1.4755808

[134] S. Dasgupta, D. Wang, C. Kübel, H. Hahn, T. F. Baumann, J. Biener. *Dynamic Control Over Electronic Transport in 3D Bulk Nanographene via Interfacial Charging.* Adv. Funct. Mater. **24** (2014) 3494.
DOI: 10.1002/adfm.201303534

[135] L.-H. Shao, M. Ruther, S. Linden, M. Wegener, J. Weissmüller. *On the mechanism of electrochemical modulation of plasmonic resonances.* Appl. Phys. Lett. **101** (2012) 121109.
DOI: 10.1063/1.4753805

[136] M. Endo, D. Chiba, H. Shimotani, F. Matsukura, Y. Iwasa, H. Ohno. *Electric double layer transistor with a (Ga,Mn)As channel.* Appl. Phys. Lett. **96** (2010) 022515.
DOI: 10.1063/1.3277146

[137] H. T. Yi, B. Gao, W. Xie, S.-W. Cheong, V. Podzorov. *Tuning the metal-insulator crossover and magnetism in $SrRuO_3$ by ionic gating.* Sci. Rep. **4** (2014) 6604.
DOI: 10.1038/srep06604

[138] C. Bi, Y. Liu, T. Newhouse-Illige, M. Xu, M. Rosales, J. W. Freeland, O. Mryasov, S. Zhang, S. G. E. te Velthuis, W. G. Wang. *Reversible Control of Co Magnetism by Voltage-Induced Oxidation.* Phys. Rev. Lett. **113** (2014) 267202.
DOI: 10.1103/PhysRevLett.113.267202

[139] U. Bauer, L. Yao, A. J. Tan, P. Agrawal, S. Emori, H. L. Tuller, S. van Dijken, G. S. D. Beach. *Magneto-ionic control of interfacial magnetism.* Nat. Mater. **14** (2015) 174.
DOI: 10.1038/NMAT4134

[140] V. Sivakumar, S. Kumar, C. Ross, Y. Shao-Horn. *Magnetic and Structural Investigation of Electrochemically Lithiated Magnetite Nanoparticles.* IEEE Trans. Magn. **43** (2007) 3121.
DOI: 10.1109/TMAG.2007.894005

[141] V. Sivakumar, N. Yabuuchi, C. A. Ross, Y. Shao-Horn. *Partially reversible changes in magnetic properties of CrO_2 nanoparticles through electrochemical cycling.* J. Appl. Phys. **103** (2008) 07D708.
DOI: 10.1063/1.2836799

[142] B. Cui, C. Song, G. Wang, Y. Yan, J. Peng, J. Miao, H. Mao, F. Li, C. Chen, F. Zeng, F. Pan. *Reversible Ferromagnetic Phase Transition in Electrode-Gated Manganites.* Adv. Funct. Mater. **24** (2014) 7233.
DOI: 10.1002/adfm.201402007

[143] B. Cui, C. Song, G. A. Gehring, F. Li, G. Wang, C. Chen, J. Peng, H. Mao, F. Zeng, F. Pan. *Electrical Manipulation of Orbital Occupancy and Magnetic Anisotropy in Manganites.* Adv. Funct. Mater. **25** (2015) 864.
DOI: 10.1002/adfm.201403370

[144] Y. Kasahara, T. Nishijima, T. Sato, Y. Takeuchi, J. Ye, H. Yuan, H. Shimotani, Y. Iwasa. *Electric-Field-Induced Superconductivity Detected by Magnetization Measurements of an Electric-Double-Layer Capacitor.* J. Phys. Soc. Jpn. **80** (2011) 023708.
DOI: 10.1143/JPSJ.80.023708

[145] Y. Kasahara, T. Nishijima, T. Sato, Y. Takeuchi, J. T. Ye, H. T. Yuan, H. Shimotani, Y. Iwasa. *Electrostatically and electrochemically induced superconducting state realized in electrochemical cells.* J. Phys.: Conf. Ser. **400** (2012) 022049.
DOI: 10.1088/1742-6596/400/2/022049

[146] S. Ghosh. *Charge-response of magnetization in nanoporous Pd-Ni alloys.* J. Magn. Magn. Mater. **323** (2011) 552.
DOI: 10.1016/j.jmmm.2010.10.008

[147] Y. Yamada, K. Ueno, T. Fukumura, H. T. Yuan, H. Shimotani, Y. Iwasa, L. Gu, S. Tsukimoto, Y. Ikuhara, M. Kawasaki. *Electrically Induced Ferromagnetism at Room Temperature in Cobalt-Doped Titanium Dioxide.* Science **332** (2011) 1065.
DOI: 10.1126/science.1202152

[148] K. Shimamura, D. Chiba, S. Ono, S. Fukami, N. Ishiwata, M. Kawaguchi, K. Kobayashi, T. Ono. *Electrical control of Curie temperature in cobalt using an ionic liquid film.* Appl. Phys. Lett. **100** (2012) 122402.
DOI: http://dx.doi.org/10.1063/1.3695160

[149] M. Kawaguchi, K. Shimamura, S. Ono, S. Fukami, F. Matsukura, H. Ohno, D. Chiba, T. Ono. *Electric Field Effect on Magnetization of an Fe Ultrathin Film.* Appl. Phys. Express **5** (2012) 063007.
DOI: 10.1143/APEX.5.063007

[150] A. K. Mishra, A. J. Darbandi, P. M. Leufke, R. Kruk, H. Hahn. *Room temperature reversible tuning of magnetism of electrolyte-gated $La_{0.75}Sr_{0.25}MnO_3$ nanoparticles.* J. Appl. Phys. **113** (2013) 033913.
DOI: 10.1063/1.4778918

[151] L. Reichel, S. Oswald, S. Fähler, L. Schultz, K. Leistner. *Electrochemically driven variation of magnetic properties in ultrathin CoPt films.* J. Appl. Phys. **113** (2013) 143904.
DOI: 10.1063/1.4799413

[152] T. Yamada, K. Morita, H. Wang, K. Kume, H. Yoshikawa, K. Awaga. *In-situ Seamless Magnetic Measurements for Solid-State Electrochemical Processes in Prussian Blue Analogues.* Angew. Chem. Int. Ed. **52** (2013) 6238.
DOI: 10.1002/anie.201301084

[153] K. Leistner, J. Wunderwald, N. Lange, S. Oswald, M. Richter, H. Zhang, L. Schultz, S. Fähler. *Electric-field control of magnetism by reversible surface reduction and oxidation reactions.* Phys. Rev. B **87** (2013) 224411.
DOI: 10.1103/PhysRevB.87.224411

[154] S. Ghosh. *Switching magnetic order in nanoporous Pd-Ni by electrochemical charging.* J. Mater. Res. **28** (2013) 3010.
DOI: 10.1557/jmr.2013.291

[155] S. Shimizu, K. S. Takahashi, T. Hatano, M. Kawasaki, Y. Tokura, Y. Iwasa. *Electrically Tunable Anomalous Hall Effect in Pt Thin Films.* Phys. Rev. Lett. **111** (2013) 216803.
DOI: 10.1103/PhysRevLett.111.216803

[156] L. Herrera Diez, A. Bernand-Mantel, L. Vila, P. Warin, A. Marty, S. Ono, D. Givord, L. Ranno. *Electric-field assisted depinning and nucleation of magnetic domain walls in FePt/Al_2O_3/liquid gate structures.* Appl. Phys. Lett. **104** (2014) 082413.
DOI: 10.1063/1.4867067

[157] S. Dasgupta, B. Das, M. Knapp, R. A. Brand, H. Ehrenberg, R. Kruk, H. Hahn. *Intercalation-Driven Reversible Control of Magnetism in Bulk Ferromagnets.* Adv. Mater. **26** (2014) 4639.
DOI: 10.1002/adma.201305932

[158] G. Gershinsky, E. Bar, L. Monconduit, D. Zitoun. *Operando electron magnetic measurements of Li-ion batteries.* Energy Environ. Sci. **7** (2014) 2012.
DOI: 10.1039/C4EE00490F

[159] R. Akiyama, H. Oikawa, K. Yamawaki, S. Kuroda. *Electric-field modulation of ferromagnetism in hexagonal chromium telluride thin film.* Phys. Status Solidi C **11** (2014) 1320.
DOI: 10.1002/pssc.201300751

[160] T. Yamada, K. Morita, K. Kume, H. Yoshikawa, K. Awaga. *The solid-state electrochemical reduction process of magnetite in Li batteries: in situ magnetic measurements toward electrochemical magnets.* J. Mater. Chem. C **2** (2014) 5183.
DOI: 10.1039/C4TC00299G

[161] C. Reitz, P. M. Leufke, R. Schneider, H. Hahn, T. Brezesinski. *Large Magnetoresistance and Electrostatic Control of Magnetism in Ordered Mesoporous $La_{1-x}Ca_xMnO_3$ Thin Films.* Chem. Mater. **26** (2014) 5745.
DOI: 10.1021/cm5028282

[162] S. Shimizu, K. S. Takahashi, M. Kubota, M. Kawasaki, Y. Tokura, Y. Iwasa. *Gate tuning of anomalous Hall effect in ferromagnetic metal $SrRuO_3$.* Appl. Phys. Lett. **105** (2014) 163509.
DOI: 10.1063/1.4899145

[163] N. Di, J. Kubal, Z. Zeng, J. Greeley, F. Maroun, P. Allongue. *Influence of controlled surface oxidation on the magnetic anisotropy of Co ultrathin films.* Appl. Phys. Lett. **106** (2015) 122405.
DOI: 10.1063/1.4916554

[164] Y. Wang, X. Zhou, C. Song, Y. Yan, S. Zhou, G. Wang, C. Chen, F. Zeng, F. Pan. *Electrical Control of the Exchange Spring in Antiferromagnetic Metals.* Adv. Mater. **27** (2015) 3196.
DOI: 10.1002/adma.201405811

[165] D. Vollath, D. V. Szabó, R. D. Taylor, J. O. Willis, K. E. Sickafus. *Synthesis and properties of nanocrystalline superparamagnetic γ-Fe_2O_3.* Nanostruct. Mater. **6** (1995) 941.
DOI: 10.1016/0965-9773(95)00215-4

[166] D. Vollath, D. Szabó. *Synthesis of nanopowders by the microwave plasma process - basic considerations and perspectives for up scaling*, in *Innovative processing of films and nanocrystalline powders* (edited by K.-L. Choy), pp. 220–251. Imperial College Press, 2002.
DOI: 10.1142/9781860949623_0008

[167] D. Vollath, D. V. Szabó. *The Microwave plasma process - a versatile process to synthesise nanoparticulate materials.* J. Nanopart. Res. **8** (2006) 417.
DOI: 10.1007/s11051-005-9014-0

[168] K. Nadeem, H. Krenn, T. Traussnig, R. Würschum, D. V. Szabó, I. Letofsky-Papst. *Effect of dipolar and exchange interactions on magnetic blocking of maghemite nanoparticles.* J. Magn. Magn. Mater. **323** (2011) 1998.
DOI: 10.1016/j.jmmm.2011.02.041

[169] K. Nadeem, H. Krenn, T. Traussnig, R. Würschum, D. V. Szabó, I. Letofsky-Papst. *Spin-glass freezing of maghemite nanoparticles prepared by microwave plasma synthesis.* J. Appl. Phys. **111** (2012) 113911.
DOI: 10.1063/1.4724348

[170] L. Spiess, G. Teichert, R. Schwarzer, H. Behnken, C. Genzel. *Moderne Röntgenbeugung.* Vieweg+Teubner, 2009.

[171] S. Topolovec. *Magnetische Eigenschaften nanokristalliner Metalloxide unter elektrochemischer Beladung.* Master thesis, Institute of Materials Physics, Graz University of Technology, 2010.

[172] JCPDS - International Centre of Diffraction Data. *Pt - PDF-file: 87-0640*, 2001.

[173] S. Trasatti, O. Petrii. *Real surface area measurements in electrochemistry.* J. Electroanal. Chem. **327** (1992) 353.
DOI: 10.1016/0022-0728(92)80162-W

[174] R. Tucceri. *A review about the surface resistance technique in electrochemistry.* Surf. Sci. Rep. **56** (2004) 85.
DOI: 10.1016/j.surfrep.2004.09.001

[175] T. Gray, C. McCain. *The Chemisorption of Oxygen and Hydrogen on Platinum*, in *Proceedings of the second international congress of surface activity*, Vol. 2 Solid/gas interface (edited by J. Schulman), p. 260. Butterworths, 1957.

[176] Q. Pang, Y. Zhang, J.-M. Zhang, K.-W. Xu. *Structural and electronic properties of atomic oxygen adsorption on Pt(111): A density-functional theory study.* Appl. Surf. Sci. **257** (2011) 3047.
DOI: 10.1016/j.apsusc.2010.10.114

[177] G. Bihlmayer, Y. Koroteev, P. Echenique, E. Chulkov, S. Blügel. *The Rashba-effect at metallic surfaces.* Surf. Sci. **600** (2006) 3888.
DOI: 10.1016/j.susc.2006.01.098

[178] A. Kawasuso, Y. Fukaya, M. Maekawa, H. Zhang, T. Seki, T. Yoshino, E. Saitoh, K. Takanashi. *Current-induced spin polarization on a Pt surface: A new approach using spin-polarized positron annihilation spectroscopy.* J. Magn. Magn. Mater. **342** (2013) 139.
DOI: 10.1016/j.jmmm.2013.04.006

[179] H. J. Zhang, S. Yamamoto, Y. Fukaya, M. Maekawa, H. Li, A. Kawasuso, T. Seki, E. Saitoh, K. Takanashi. *Current-induced spin polarization on metal surfaces probed by spin-polarized positron beam.* Sci. Rep. **4** (2014) 4844.
DOI: 10.1038/srep04844

[180] J. Wiebe, F. Meier, K. Hashimoto, G. Bihlmayer, S. Blügel, P. Ferriani, S. Heinze, R. Wiesendanger. *Unoccupied surface state on Pt(111) revealed by scanning tunneling spectroscopy.* Phys. Rev. B **72** (2005) 193406.
DOI: 10.1103/PhysRevB.72.193406

[181] L. Xu, S. Zhang. *Electric field control of interface magnetic anisotropy.* J. Appl. Phys. **111** (2012) 07C50.
DOI: 10.1063/1.3670002

[182] S.-J. Gong, C.-G. Duan, Y. Zhu, Z.-Q. Zhu, J.-H. Chu. *Controlling Rashba spin splitting in Au(111) surface states through electric field.* Phys. Rev. B **87** (2013) 035403.
DOI: 10.1103/PhysRevB.87.035403

[183] S. Subkow, M. Fähnle. *Potential explanation of charge response of magnetization in nanoporous systems.* Phys. Rev. B **84** (2011) 220409.
DOI: 10.1103/PhysRevB.84.220409

[184] M. Fähnle, S. Subkow. *Ab-initio calculations and atomistic calculations on the magnetoelectric effects in metallic nanostructures.* Phys. Status Solidi C **11** (2014) 186.
DOI: 10.1002/pssc.201350286

[185] B. Conway. *Transition from 'supercapacitor' to 'battery' behavior in electrochemical energy storage.* J. Electrochem. Soc. **138** (1991) 1539.
DOI: 10.1149/1.2085829

[186] P. Castro, E. Vago, E. Calvo. *Surface electrochemical transformations on spinel iron oxide electrodes in aqueous solutions.* J. Chem. Soc., Faraday Trans. **92** (1996) 3371.
DOI: 10.1039/FT9969203371

[187] V. A. Brabers. *Ferrimagnetic Insulators*, in *Handbook of Magnetism and Advanced Magnetic Materials*, Vol. 4 (edited by H. Kronmüller, S. Parkin), pp. 2079–2097. John Wiley & Sons, 2007.
DOI: 10.1002/9780470022184.hmm414

[188] C.-G. Duan, J. P. Velev, R. F. Sabirianov, Z. Zhu, J. Chu, S. S. Jaswal, E. Y. Tsymbal. *Surface Magnetoelectric Effect in Ferromagnetic Metal Films.* Phys. Rev. Lett. **101** (2008) 137201.
DOI: 10.1103/PhysRevLett.101.137201

[189] O. Iglesias, A. Labarta. *Finite-size and surface effects in maghemite nanoparticles: Monte Carlo simulations.* Phys. Rev. B **63** (2001) 184416.
DOI: 10.1103/PhysRevB.63.184416

[190] H. Khurshid, P. Lampen-Kelley, Ò. Iglesias, J. Alonso, M.-H. Phan, C.-J. Sun, M.-L. Saboungi, H. Srikanth. *Spin-glass-like freezing of inner and outer surface layers in hollow γ-Fe_2O_3 nanoparticles.* ArXiv e-prints (2015) arXiv:1503.00602v2.

[191] J. Mazo-Zuluaga, J. Restrepo, J. Mejia-Lopez. *Effect of surface anisotropy on the magnetic properties of magnetite nanoparticles: A Heisenberg-Monte Carlo study.* J. Appl. Phys. **103** (2008) 113906.
DOI: 10.1063/1.2937240

[192] M. Hakamada, M. Takahashi, T. Furukawa, M. Mabuchi. *Coercivity of nanoporous Ni produced by dealloying.* Appl. Phys. Lett. **94** (2009) 153105.
DOI: 10.1063/1.3119663

[193] Z. Dan, F. Qin, Y. Sugawara, I. Muto, N. Hara. *Bimodal nanoporous nickel prepared by dealloying $Ni_{38}Mn_{62}$ alloys.* Intermetallics **31** (2012) 157.
DOI: 10.1016/j.intermet.2012.06.018

[194] D. V. Pugh, A. Dursun, S. G. Corcoran. *Formation of nanoporous platinum by selective dissolution of Cu from $Cu_{0.75}Pt_{0.25}$.* J. Mater. Res. **18** (2003) 216.
DOI: 10.1557/JMR.2003.0030

[195] W. Li, H. Ma, L. Huang, Y. Ding. *Well-defined nanoporous palladium for electrochemical reductive dechlorination.* Phys. Chem. Chem. Phys. **13** (2011) 5565.
DOI: 10.1039/C0CP02178D

[196] Y. Sun, J. D. Burton, E. Y. Tsymbal. *Electrically driven magnetism on a Pd thin film.* Phys. Rev. B **81** (2010) 064413.
DOI: 10.1103/PhysRevB.81.064413

[197] S. Amalraj, D. Aurbach. *The use of in situ techniques in R & D of Li and Mg rechargeable batteries.* J. Solid State Electr. **15** (2011) 877.
DOI: 10.1007/s10008-011-1324-9

[198] S. Ramdon, B. Bhushan, S. C. Nagpure. *In situ electrochemical studies of lithium-ion battery cathodes using atomic force microscopy.* J. Power Sources **249** (2014) 373.
DOI: 10.1016/j.jpowsour.2013.10.099

[199] P. Harks, F. Mulder, P. Notten. *In situ methods for Li-ion battery research: A review of recent developments.* J. Power Sources **288** (2015) 92.
DOI: 10.1016/j.jpowsour.2015.04.084

[200] N. Imanishi, M. Fujiyoshi, Y. Takeda, O. Yamamoto, M. Tabuchi. *Preparation and ^{7}Li-NMR study of chemically delithiated $Li_{1-x}CoO_2$ ($0 < x < 0.5$).* Solid State Ion. **118** (1999) 121.
DOI: 10.1016/S0167-2738(98)00441-X

[201] S. Levasseur, M. Ménétrier, Y. Shao-Horn, L. Gautier, A. Audemer, G. Demazeau, A. Largeteau, C. Delmas. *Oxygen Vacancies and Intermediate Spin Trivalent Cobalt Ions in Lithium-Overstoichiometric $LiCoO_2$.* Chem. Mater. **15** (2003) 348.
DOI: 10.1021/cm021279g

[202] J. Sugiyama, H. Nozaki, J. H. Brewer, E. J. Ansaldo, G. D. Morris, C. Delmas. *Frustrated magnetism in the two-dimensional triangular lattice of Li_xCoO_2.* Phys. Rev. B **72** (2005) 144424.
DOI: 10.1103/PhysRevB.72.144424

[203] D. Kellerman, V. Galakhov, A. Semenova, Y. Blinovskov, O. Leonidova. *Semiconductor-metal transition in defect lithium cobaltite.* Phys. Solid State **48** (2006) 548.
DOI: 10.1134/S106378340603022X

[204] K. Mukai, Y. Ikedo, H. Nozaki, J. Sugiyama, K. Nishiyama, D. Andreica, A. Amato, P. L. Russo, E. J. Ansaldo, J. H. Brewer, K. H. Chow, K. Ariyoshi, T. Ohzuku. *Magnetic Phase Diagram of Layered Cobalt Dioxide Li_xCoO_2.* Phys. Rev. Lett. **99** (2007) 087601.
DOI: 10.1103/PhysRevLett.99.087601

[205] M. Ménétrier, D. Carlier, M. Blangero, C. Delmas. *On "Really" Stoichiometric $LiCoO_2$.* Electrochem. Solid-State Lett. **11** (2008) A179.
DOI: 10.1149/1.2968953

[206] J. T. Hertz, Q. Huang, T. McQueen, T. Klimczuk, J. W. G. Bos, L. Viciu, R. J. Cava. *Magnetism and structure of Li_xCoO_2 and comparison to Na_xCoO_2.* Phys. Rev. B **77** (2008) 075119.
DOI: 10.1103/PhysRevB.77.075119

[207] T. Motohashi, T. Ono, Y. Sugimoto, Y. Masubuchi, S. Kikkawa, R. Kanno, M. Karppinen, H. Yamauchi. *Electronic phase diagram of the layered cobalt oxide system Li_xCoO_2 ($0.0 \leq x \leq 1.0$).* Phys. Rev. B **80** (2009) 165114.
DOI: 10.1103/PhysRevB.80.165114

[208] K. Miyoshi, C. Iwai, H. Kondo, M. Miura, S. Nishigori, J. Takeuchi. *Magnetic and electronic properties of Li_xCoO_2 single crystals.* Phys. Rev. B **82** (2010) 075113.
DOI: 10.1103/PhysRevB.82.075113

[209] D. Mohanty, H. Gabrisch. *Comparison of magnetic properties in Li_xCoO_2 and its decomposition products $LiCo_2O_4$ and Co_3O_4.* Solid State Ion. **194** (2011) 41.
DOI: 10.1016/j.ssi.2011.05.005

[210] T. Y. Ou-Yang, F.-T. Huang, G. J. Shu, W. L. Lee, M.-W. Chu, H. L. Liu, F. C. Chou. *Electronic phase diagram of Li_xCoO_2 revisited with potentiostatically deintercalated single crystals.* Phys. Rev. B **85** (2012) 035120.
DOI: 10.1103/PhysRevB.85.035120

[211] K. Mukai, Y. Aoki, D. Andreica, A. Amato, I. Watanabe, S. R. Giblin, J. Sugiyama. *Thermally activated spin fluctuations in stoichiometric $LiCoO_2$ clarified by electron paramagnetic resonance and muon-spin rotation and relaxation measurements.* Phys. Rev. B **89** (2014) 094406.
DOI: 10.1103/PhysRevB.89.094406

[212] G. Klinser. *Charakterisierung des Beladungszustandes von Lithium-Kobaltoxid Batteriekathoden durch Magnetometrie.* Master thesis, Institute of Materials Physics, Graz University of Technology, 2014.

[213] K. Mizushima, P. Jones, P. Wiseman, J. Goodenough. *Li_xCoO_2 ($0 < x \leq 1$): A new cathode material for batteries of high energy density.* Mater. Res. Bull. **15** (1980) 783.
DOI: 10.1016/0025-5408(80)90012-4

[214] K. Mizushima, P. Jones, P. Wiseman, J. Goodenough. *Li_xCoO_2 ($0 < x \leq 1$): A new cathode material for batteries of high energy density.* Solid State Ion. **3-4** (1981) 171.
DOI: 10.1016/0167-2738(81)90077-1

[215] K. Ozawa. *Lithium-ion rechargeable batteries with $LiCoO_2$ and carbon electrodes: the $LiCoO_2$/C system.* Solid State Ion. **69** (1994) 212.
DOI: 10.1016/0167-2738(94)90411-1

[216] A. Manthiram, T. Muraliganth. *Lithium Intercalation Cathode Materials for Lithium-Ion Batteries*, in *Handbook of Battery Materials* (edited by C. Daniel, J. O. Besenhard), pp. 341–375. Wiley-VCH, 2011.
DOI: 10.1002/9783527637188.ch12

[217] V. Etacheri, R. Marom, R. Elazari, G. Salitra, D. Aurbach. *Challenges in the development of advanced Li-ion batteries: a review.* Energy Environ. Sci. **4** (2011) 3243.
DOI: 10.1039/C1EE01598B

[218] A. Yoshino. *Development of the Lithium-Ion Battery and Recent Technological Trends*, in *Lithium-Ion Batteries* (edited by G. Pistoia), pp. 1 – 20. Elsevier, 2014.
DOI: 10.1016/B978-0-444-59513-3.00001-7

[219] M. S. Whittingham. *Ultimate Limits to Intercalation Reactions for Lithium Batteries.* Chem. Rev. **114** (2014) 11414.
DOI: 10.1021/cr5003003. PMID: 25354149

[220] K. Momma, F. Izumi. *VESTA: a three-dimensional visualization system for electronic and structural analysis.* J. Appl. Crystallogr. **41** (2008) 653.
DOI: 10.1107/S0021889808012016

[221] Y. Lyu, J. Huang, H. Li. *Layered and Spinel Structural Cathodes*, in *Rechargeable Batteries* (edited by Z. Zhang, S. S. Zhang), pp. 67–92. Springer, 2015.
DOI: 10.1007/978-3-319-15458-9_3

[222] C. Graf. *Kathodenmaterialien für Lithium-Ionen-Batterien*, in *Handbuch Lithium-Ionen-Batterien* (edited by R. Korthauer), pp. 31–44. Springer, 2013.
DOI: 10.1007/978-3-642-30653-2_4

[223] V. Bagotsky, A. Skundin, Y. Volfkovich. *Electrochemical Power Sources: Batteries, Fuel Cells, and Supercapacitors.* Wiley, 2015.
DOI: 10.1002/9781118942857

[224] L. Dahéron, R. Dedryvère, H. Martinez, M. Ménétrier, C. Denage, C. Delmas, D. Gonbeau. *Electron Transfer Mechanisms upon Lithium Deintercalation from $LiCoO_2$ to CoO_2 Investigated by XPS.* Chem. Mater. **20** (2008) 583.
DOI: 10.1021/cm702546s

[225] T. Motohashi, Y. Katsumata, T. Ono, R. Kanno, M. Karppinen, H. Yamauchi. *Synthesis and properties of CoO_2 the $x = 0$ end member of the Li_xCO_2 and Na_xCoO_2 systems.* Chem. Mater. **19** (2007) 5063.
DOI: 10.1021/cm0702464

[226] A. Milewska, K. Świerczek, J. Tobola, F. Boudoire, Y. Hu, D. Bora, B. Mun, A. Braun, J. Molenda. *The nature of the nonmetal-metal transition in Li_xCoO_2 oxide.* Solid State Ion. **263** (2014) 110.
DOI: 10.1016/j.ssi.2014.05.011

[227] N. F. Mott. *Knight shift at an Anderson transition.* Philos. Mag. **29** (1974) 59.
DOI: 10.1080/14786437408213553

[228] M. Ménétrier, I. Saadoune, S. Levasseur, C. Delmas. *The insulator-metal transition upon lithium deintercalation from $LiCoO_2$: electronic properties and ^7Li NMR study.* J. Mater. Chem. **9** (1999) 1135.
DOI: 10.1039/A900016J

[229] K. Iwaya, T. Ogawa, T. Minato, K. Miyoshi, J. Takeuchi, A. Kuwabara, H. Moriwake, Y. Kim, T. Hitosugi. *Impact of Lithium-Ion Ordering on Surface Electronic States of* Li_xCoO_2. Phys. Rev. Lett. **111** (2013) 126104.
DOI: 10.1103/PhysRevLett.111.126104

[230] K. Knížek, J. Hejtmánek, M. Maryško, E. Šantavá, Z. Jirák, J. Buršík, K. Kirakci, P. Beran. *Structure and properties of a novel cobaltate $La_{0.30}CoO_2$.* J. Solid State Chem. **184** (2011) 2231.
DOI: 10.1016/j.jssc.2011.06.021

[231] W.-S. Yoon, K.-B. Kim, M.-G. Kim, M.-K. Lee, H.-J. Shin, J.-M. Lee, J.-S. Lee, C.-H. Yo. *Oxygen Contribution on Li-Ion Intercalation–Deintercalation in $LiCoO_2$ Investigated by O K-Edge and Co L-Edge X-ray Absorption Spectroscopy.* J. Phys. Chem. B **106** (2002) 2526.
DOI: 10.1021/jp013735e

[232] M. K. Aydinol, A. F. Kohan, G. Ceder, K. Cho, J. Joannopoulos. *Ab initio study of lithium intercalation in metal oxides and metal dichalcogenides.* Phys. Rev. B **56** (1997) 1354.
DOI: 10.1103/PhysRevB.56.1354

[233] G. Cherkashinin, K. Nikolowski, H. Ehrenberg, S. Jacke, L. Dimesso, W. Jaegermann. *The stability of the SEI layer, surface composition and the oxidation state of transition metals at the electrolyte-cathode interface impacted by the electrochemical cycling: X-ray photoelectron spectroscopy investigation.* Phys. Chem. Chem. Phys. **14** (2012) 12321.
DOI: 10.1039/C2CP41134B

[234] W. Waag, C. Fleischer, D. U. Sauer. *Critical review of the methods for monitoring of lithium-ion batteries in electric and hybrid vehicles.* J. Power Sources **258** (2014) 321.
DOI: 10.1016/j.jpowsour.2014.02.064

[235] T. Gallien, H. Krenn, R. Fischer, S. Lauterbach, B. Schweighofer, H. Wegleiter. *Magnetism Versus $LiFePO_4$ Battery's State of Charge: A Feasibility Study for Magnetic-Based Charge Monitoring.* IEEE Trans. Instrum. Meas. **PP** (2015) 1.
DOI: 10.1109/TIM.2015.2437634

[236] T. Kadyk, M. Eikerling. *Magnetic susceptibility as a direct measure of oxidation state in $LiFePO_4$ batteries and cyclic water gas shift reactors.* Phys. Chem. Chem. Phys. **17** (2015) 19834.
DOI: 10.1039/C5CP02977E

[237] B. Xu, D. Qian, Z. Wang, Y. S. Meng. *Recent progress in cathode materials research for advanced lithium ion batteries.* Mater. Sci. Eng. R-Rep. **73** (2012) 51.
DOI: 10.1016/j.mser.2012.05.003

[238] D. Mohanty, H. Gabrisch. *Microstructural investigation of $Li_xNi_{1/3}Mn_{1/3}Co_{1/3}O_2$ ($x \leq 1$) and its aged products via magnetic and diffraction study.* J. Power Sources **220** (2012) 405.
DOI: 10.1016/j.jpowsour.2012.08.005

[239] A. Mauger, F. Gendron, C. Julien. *Magnetic properties of $Li_xNi_yMn_yCo_{1-2y}O_2$ ($0.2 \leq 1-2y \leq 0.5, 0 \leq x \leq 1$).* J Alloy. Compd. **520** (2012) 42.
DOI: 10.1016/j.jallcom.2011.12.055

[240] M. Labrini, I. Saadoune, F. Scheiba, A. Almaggoussi, J. Elhaskouri, P. Amoros, H. Ehrenberg, J. Brötz. *Magnetic and structural approach for understanding the electrochemical behavior of $LiNi_{0.33}Co_{0.33}Mn_{0.33}O_2$ positive electrode material.* Electrochim. Acta **111** (2013) 567.
DOI: 10.1016/j.electacta.2013.08.051

Acknowledgments

I would like to sincerely thank the following people who supported me in my research and who contributed to the completion of this thesis:

Univ.-Prof. Dr. Roland Würschum, Institute of Materials Physics, TU Graz
For giving me the opportunity to work on this thesis in his department, the valuable supervision, advice and guidance throughout my doctoral studies as well as for the freedom given to me undertaking this research. Particularly, for many productive discussions and his support during the writing process of the published articles and this thesis.

Univ.-Prof. Dr. Heinz Krenn, Institute of Physics, KFU Graz
For providing me the possibility to perform the SQUID magnetometry measurements in his laboratory, for his tremendous support during these measurements and for many fruitful discussions about magnetism and his valuable ideas for experimental work.

Univ.-Prof. Dr. Ludwig Schultz, Leibniz-Institute of Solid State and Materials Research Dresden and TU Dresden
For accepting to review this thesis as external reviewer.

Dipl.-Ing. Eva-Maria Steyskal, Institute of Materials Physics, TU Graz
For the fruitful collaboration in the field of electrochemical tuning of material properties and many valuable discussions, especially concerning electrochemistry.

Dipl.-Ing. Gregor Klinser, Institute of Materials Physics, TU Graz
For the productive collaboration on the magnetic studies of the $LiCoO_2$ cathodes and especially for his valuable contributions to their interpretation.

Dr. Harald Kren, Dr. Stefan Koller and Christian Baumann, VARTA Micro Innovation GmbH, Graz

For their collaboration on the Li-ion battery studies and the many suggestions concerning the design of the electrochemical cell used for the in-operando studies on $LiCoO_2$. In particular, Harald Kren for handling the difficult task of cell assembling in the glove box and Christian Baumann for the preparation of the $LiCoO_2$ cathodes.

Dr. Thomas Traußnig, formerly Institute of Materials Physics, TU Graz

For the first work on electrochemical in-situ studies in a SQUID magnetometer which served as a base for this thesis and for sharing his knowledge and experience with me during my master thesis.

Dr. Peter Parz, formerly Institute of Materials Physics, TU Graz

For many helpful discussions about electrochemistry and materials science as well as for his many suggestions for solving experimental problems.

Ao.Univ.-Prof. Dr. Stephan Landgraf, Institute of Physical and Theoretical Chemistry, TU Graz

For valuable discussions about electrochemistry.

Dr. Dorothée Vinga Szabó, Institute for Applied Materials – Materials Processing Technology, Karlsruhe Institute of Technology

For the synthesis and provision of the γ-Fe_2O_3 nanoparticles.

Dr. Ilse Letofsky-Papst, Sanja Simic and Manuel Paller, Institute of Electron Microscopy and Nanoanalysis, TU Graz

For their help. Ilse Letofsky-Papst and Sanja Simic for performing the SEM and EDX measurements on the γ-Fe_2O_3/Pt nanocomposite and Manuel Paller for cutting the substrate stripes for the in-situ electrodeposition experiments out of the Au(111)/Si wafer.

All present and former colleagues at the Institute of Materials Physics

For all their help during the last years and particularly for providing a pleasant working atmosphere.

My family and friends

For all their support and for all the good times spent together. In particular, I want to thank my parents, Veronika and Peter and my sisters, Claudia and Iris, for their continuous encouragement and love.

EIDESSTATTLICHE ERKLÄRUNG

AFFIDAVIT

Ich erkläre an Eides statt, dass ich die vorliegende Arbeit selbstständig verfasst, andere als die angegebenen Quellen/Hilfsmittel nicht benutzt, und die den benutzten Quellen wörtlich und inhaltlich entnommenen Stellen als solche kenntlich gemacht habe. Das in TUGRAZonline hochgeladene Textdokument ist mit der vorliegenden Masterarbeit/Diplomarbeit/Dissertation identisch.

I declare that I have authored this thesis independently, that I have not used other than the declared sources/resources, and that I have explicitly indicated all material which has been quoted either literally or by content from the sources used. The text document uploaded to TUGRAZonline is identical to the present master's thesis/diploma thesis/doctoral dissertation.

_____ _____

Datum / Date Unterschrift / Signature